Eötvös Loránd University
Institute of Geography and Earth Sciences
Department of Meteorology

Application of Scorer-parameter in Mountain Wave Forecasting at the Hungarian Meteorological Service

Master thesis

Author:

Imen Ghanmi

Meteorology MSc,

Forecaster specialization

Supervisor:

Péter Salavec

Unit of Aviation Meteorology, Hungarian Meteorological Service

Departmental Consultant:

Zoltán Barcza

Department of Meteorology, Eötvös Loránd University

Budapest, 2020

Contents

1. Introduction

1.1. Aviation and atmospheric turbulence

It is well known that aviation is strongly related to atmospheric processes. Numerous weather events jeopardize flight safety like mountain waves (as they represent serious hazard sources such as strong up- and down-drafts), downslope windstorms (*Holmboe and Klieforth*, 1957; *Jiang and Doyle*, 2008), clear air turbulence (CAT) associated with tropospheric wave breaking (*Peltier and Clark*, 1979; *Belušić et al.*, 2007), low-level turbulence and 'rotors' associated with wave-induced boundary layer separation (*Doyle and Durran*, 2002; *Strauss et al.*, 2015) as well as hazards to surface transport such as very strong or gusty winds (*Grisogono and Belušić*, 2009).

Turbulence is defined as high-frequency oscillations in the wind. The order of their period ranges from approximately 1 minute to 0.1 seconds. Since turbulence has been associated with many aviation accidents, various researches have been conducted to understand the physical process behind it. *Lilly* (1968) proposed that cloud-top cooling was strongly related to turbulence in the stratus-topped boundary layer, a notion that has subsequently been corrected introducing convection as the main source for turbulence (*Deardorff*, 1980; *Moeng*, 1986; *Hanson*, 1987; *Curry et al.*, 1988). In general, thermal convection without any cloud formation is also a source of turbulence in the atmospheric boundary layer, as the vertical velocity in thermals are usually in the same order as the horizontal wind. This is called thermal turbulence (*Malkus and Chandrasekhar*, 1954; *Elder*, 1967; *Kaimal and Finnigan*, 1994; *Sun et al.*, 2006).

Due to Earth-atmosphere interaction and internal viscosity of the air, in the atmospheric boundary layer (ABL), winds tend to deviate on isobars, towards lower pressure regions. This deviation creates vertical wind shear which can lead to mechanical turbulence causing vertical mixing between the air layers. Above the ABL in the free troposphere, turbulence due to viscosity is less present and, in mid-latitudes, the geostrophic wind prevails following the isobars (*Oke*, 2002).

Wind shear is considered a major source of turbulence in the troposphere (*Vinnichenko and Dutton*, 1969; *Browning et al.*, 1970; *Wyngaard et al.*, 1971; *Kim and Mahrt*, 1992). Basic fluid dynamics states that shear cannot exceed a maximum in any fluid, such as the atmosphere, without transforming the laminar flow turbulent. Due to the high frequency of turbulent oscillations, the wind components can change markedly in space, producing strong

local wind shear on a spatial scale comparable to an aircraft's size (*Cushman-Roisin*, 2011). This is responsible for the most weather-related in-flight injuries according to the investigations (*Sato*, 2004).

Despite that most of the flight duration for manned aircraft is above the ABL (*Watkins et al.*, 2010), there is only a moderate focus on this aspect of flight as most of the weather-related accidents occur during takeoff or landing. However, CAT and other turbulence sources can be encountered in this layer presenting a serious hazard for the crew and the passengers.

Depending on the type, some airplanes are more susceptible to the effects of turbulence than others. Light aircraft are more significantly affected even by light turbulence than heavier aircraft. Relatively few reports of turbulence are received from fast military jets which are designed to have a higher tolerance.

This work focuses on the study of Mountain Waves (MTW), which occurs when winds flow over topography. *Eliassen and Palm* (1960) highlighted their responsibility for transporting a significant amount of momentum and energy to the middle and upper atmosphere. Thus, MTW can be both an advantage and a disadvantage to aviation.

Experienced glider pilots look for the updraft side of MTW to gain altitude. With ascent rates of approximately 10 to 50 m s^{-1} and to soar a glider to an altitude of 20 to 30 km without an engine, MTW can be very useful in gaining height quickly. Within such updrafts, the turbulence is usually weak, so the glider pilot can use it to assure a smooth flight (*Teets Jr. and Carter*, 2003).

Over the history of aviation, numerous aircraft accidents have occurred over mountain areas, for which there was no satisfactory interpretation or explanation and it has been known that the airflow over mountainous or hilly terrain is more disturbed than over flat terrain. Recently, turbulence related incidents accounted for over half of all the commercial carrier accident and the National Transportation Safety Board reported that incidents between the years 1990 and 2000 and caused around 65% of all weather-related commercial aircraft incidents from more recent investigations (*Sharman et al.*, 2000; *Sharman et al.*, 2006).

Several mechanisms and environmental conditions can cause vertically propagating MTW to disturb aircraft operations:

- Increase of the wave amplitude as waves propagate upwards in decreasing air density (*Eliassen and Palm*, 1960).
- Wind speed decreasing with height, which may lead to a layer of zero wind speed (*Booker and Bretherton*, 1967).

- Creation of environmental critical levels by wind direction changes (*Broad*, 1995).
- An abrupt increase in atmospheric stability, for example a sharp inversion or the transition from the troposphere to the stratosphere (*VanZandt and Fritts*, 1989).

Since the discovery of MTW in 1933 (*Hirth*, 1935; *Küttner*, 1938), several theoretical and numerical studies were made to describe them (*Scorer*, 1949; *Long*, 1953; *Küttner*, 1959; *Scorer and Klieforth*, 1959; *Smith*, 1979; *Tokgozlu et al.*, 2006). However, our knowledge about their related turbulence is limited and they are examined predominantly by numerical models designed for simulating mountain waves and related turbulence (*Pao*, 1969; *Orlanski and Ross*, 1973; *Murrow et al.*, 1982; *Tan and Eckermann*, 2000; *Epifanio and Quian*, 2008; *Smith and Skyllingstad*, 2009). A comprehensive review of the current state in this topic was given recently by *Teixeira* (2014). Numerical models operationally used in general weather forecasting have difficulties accurately forecasting turbulence because of their coarser resolution, thus, forecasters usually use synoptic-scale analysis techniques and numerical model products based mainly on model wind and wind shear (*Ellrod and Knapp*, 1992).

1.2. Aircraft accidents outside Hungary

On 5th March 1966, the flight 911 of the British Overseas Airways Corporation (BOAC) was traveling around the world and made a stop in Tokyo. Continuing the journey, the same day, the plane crashed shortly after take-off as a result of an encounter with severe turbulence near Mount Fuji in Japan, killing all 113 passengers and 11 crew members. Vertical accelerations were so strong that parts of the plane experienced dangerous structural damage (Fig. 1). According to satellite observations, 30 minutes before the accident, lenticularis clouds were visible about 240 km south of the peak, indicating CAT (*Job*, 1995).

Investigators discovered the true danger of the poorly understood mountain wave phenomenon, and the accident served as a wake-up call to the aviation industry about this threat (*Dempsey*, 2019). Mount Fuji has a height of 3776 m above mean sea level and width of a few kilometers. As it is the tallest mountain in Japan, it is directly exposed to the stream of wind blowing over the islands from west to east. The investigation report explained that powerful existed in the lee side of Mount Fuji and that the breakdown of the waves resulted in small-scale turbulence, in which the intensity might have become severe or extreme in a short period (*Stone*, 1968).

In a more detailed explanation by *Dempsey* (2019), it is described that a mountain wave can overturn or rotors can cause high vertical wind speeds, and strong spatial variations in

it, generating vertical wind gusts over 100 km h^{-1}. An airplane can easily handle a 100 km h^{-1} horizontal wind because the resulting aerodynamic forces do not differ much from the normal usually experienced in flight. In contrast, a vertical wind of the same speed is extremely rare, and a plane designed to withstand such horizontal wind loads may not be able to withstand those same loads from a different direction. A 100 km h^{-1} vertical gust can cause severe structural damage to an airplane.

Fig. 1. The Boeing 707 aircraft G-APFE crashed on 5th March 1966 at an elevation of 1320 m on Mount Fuji, Japan (Dempsey, 2019; Original source is unclear).

Another incident on 16th December 2015 was when a Cessna 182Q aircraft crashed, killing two passengers and injuring the pilot. The crash took place near the Kareedouw – Tsitsikamma Mountains, South Africa. Analysis of meteorological information revealed later that MTW was involved, and the associated turbulence was most likely the cause of the crash (*Van der Mescht and Geldenhuys*, 2017).

On 30th December 2015, an Air Canada flight encountered severe mountain wave turbulence over Alaska. Pilots reported that turbulence lasted about 40 minutes and the flight made an emergency landing. In the aftermath of the incident 21 passengers were hospitalized (*Gast and Moshtaghian*, 2015).

1.3. Aircraft accidents in Hungary

Since 2006, approximately three airplane accidents per year can be connected to mountain turbulence according to the requested accident investigations at the Transportation Safety Bureau of Hungary. In most of the cases, however, some ultralight aircraft (usually paraglider or hang-glider) is involved and the investigation of meteorological circumstances are often not detailed enough to prove the connection.

For example, on 14th May 2006 near Hármashatár-hegy (Budapest), a paraglider pilot encountered a strong headwind above the hilltop. However, more investigations from the authority need to be done, to confirm if the presence of turbulence is related to this incident (*Janovics and Farkas*, 2006).

1.4. Motivation of the study and objectives

MTW is often accompanied with other turbulence phenomena, for example rotor motions, hydraulic jumps, areas of increased and decreased wind speeds as well as fluctuations in the lift. The effect of these can be damaging if the pilot is unaware of the flow in mountainous terrain (*Sharman and Lane*, 2016).

Currently, airlines use turbulence forecasts, pilot reports and real-time weather observations (radar, satellite, etc.) to plan safe sky routes. If mountain wave activity is forecasted or reported, Delta Air Lines, for example, adopts a mountain wave avoidance system for which pilots can either avoid selected altitudes or avoid the steep terrain area (*Sharman and Lane*, 2016).

To make mountain flying safer, a wide range of research has been conducted in recent years to gain a better understanding of airflow over mountains which is useful for the insurance of the national mountain flight operations. As a result, much useful information has been gathered which, if properly used, would be instrumental in reducing the number of aircraft accidents over mountains.

This thesis work is a contribution to the better analysis and understanding of the MTWs atmospheric process and development of aviation forecasting. The Unit of Aviation Meteorology at the Hungarian Meteorological Service (HMS) provides forecast products for general aviation (thermal soaring, balloon, mountain wave gliding, etc). The information published for mountain wave gliding, for example, is a wind profile (time-height section) for 4 airfields (Dunakeszi, Kőszeg, Pécs-Pogány and Gyöngyös-Pipishegy) up to 12 km height, a surface wind gust and a precipitation map. However, the theory of MTW is not governed

only by the wind profile so this raises the need for extending the forecast products by introducing more useful parameters (*Salavec*, 2018).

The purpose of the present work is to serve as a basis for the documentation of the new MTW forecast products planned to be published on the http://aviation.met.hu website.

The steps of this research are as follows:

- Designing the products. Presentation and explanation of the preliminary plans, generated by the HAWK-3 visualization system, will be done in this thesis.
- Analysis of a case study using the operational numerical weather prediction (NWP) model AROME (*Seity et al.*, 2010; *Szintai et al.*, 2015), for a case when MTW formation was observed in Hungary.
- Examination of several weather situations both with and without MTW formation. Interpretation of features visible on the products in cases when MTW formation or trapping is expected will be part of the planned documentation attached to the products.
- Development of a possible automatic detection method of probable trapping of MTW in the model simulation will be proposed.

The thesis is organized as follows: Section 2 contains a review of the literature: a qualitative summary of the mountain wave and related phenomena are discussed, followed by the physical aspects of the linear theory. Methodology of the research published in this thesis is detailed in Section 3. In Section 4, a case study will be presented with samples of the planned products, a sensitivity test, and a proposal of a wave trapping detection method. Conclusions and further plans are outlined in Section 5.

2. Literature Review

2.1. Gravity waves, mountain waves and lee waves

One of the most interesting atmospheric phenomena related to the airflow over mountains is the generation of atmospheric gravity waves. These waves have two types: surface waves existing on the interface between media with different densities, and internal waves within one medium (*Fritts and Alexander*, 2003). Gravity waves can be generated in the troposphere by frontal systems, thunderstorms, or airflow over mountains (*Balachandran*, 1980; *Ralph et al.*, 1999; *Lin and Zhang*, 2008; *Fritts and Nastrom*, 1992).

Atmospheric gravity waves play a key role in the middle atmosphere dynamics as they enhance the transfer of momentum from the troposphere to the stratosphere and mesosphere (*McLandress*, 1998). These waves are constantly present in the atmosphere (*Francis*, 1975; *Nappo*, 2012), but their existence is only occasionally revealed visually by cloud patterns.

Gravity waves induced by orographic barriers, generally belong to the category of internal waves, as they propagate in the interior of the fluid and not at the discontinuity surface between two media with different density. Internal gravity waves are transverse waves for which the parcel oscillations are perpendicular to the direction of propagation. MTW is a type of internal gravity waves, excited by the topography and they play a part in the atmospheric dynamics at different scales (*Nappo*, 2012; *Holton and Hakim*, 2013).

Wurtele et al. (1996) categorized lee waves as hydrostatic and non-hydrostatic lee waves. Hydrostatic waves are found only above the mountain while non-hydrostatic waves can sometimes propagate far downstream of the mountain. The wavelength of the non-hydrostatic waves is usually shorter than that of the hydrostatic waves. Resonant waves are defined as a superposition series of non-hydrostatic gravity waves with both upwards downwards propagation in vertical (*Tutiš*, 1992; *Lane et al.*, 2001).

Topography and the generation of the MTW can modify several elements of weather processes, like precipitation, wind, cyclogenesis, downslope windstorms, etc. (*Guarino*, 2017). Sometimes an inversion is above the mountains, so the air can flow over the summit if it has enough kinetic energy. In other cases, when inversion is below the mountain top, the air must often flow around the mountain (*Scorer*, 1951; *Reiter and Rasmussen*, 1967; *Uhlenbrock et al.*, 2007).

When the air flows over a mountain ridge, internal gravity waves can be excited. In the case of high mountains and specific environmental conditions, in terms of the vertical profile

of wind speed and air density, the typical order of the wavelength of these waves range from 100 m to 10 km. MTW of high amplitudes (specifically trapped lee waves) are associated with the formation of lenticular and lower-level rotor clouds (*Scorer and Klieforth*, 1959). They transport energy and may drive changes in winds, temperature, and chemical composition of the atmosphere through redistribution of atmospheric constituents in wave breaking regions and forcing the mean air circulations (*Guarino*, 2017).

As MTW propagates upward, they can overturn and break (in a similar manner to water waves running up a beach). Downslope windstorms can often be associated with mountain wave events. Theory suggests, however, that they are not necessarily related (*Klemp and Lilly*, 1975; *Lilly*, 1978; *Dierking*, 1998). In these situations, surface wind speeds on the lee side sometimes exceed the speed of 150 km h^{-1} (*Minár et al.*, 2008; *Guarino*, 2017).

People living in the vicinity of mountains are familiar with their impact on the local weather and the associated implications for their lives (*Beall*, 2007; *Kaltenborn et al.*, 2010; *McDowell et al.*, 2013). For example, hikers depend on the mountain weather for their tours, tourism entrepreneurs rely on snowfall in the winter season (*Abegg*, 1996), and energy suppliers benefit from enhanced wind speeds at the flanks of the high mountains for wind power production (*Ahmed*, 2014). The impact of mountain turbulence on aviation operations is one of the motivations for their scientific and physical study.

2.2. Mountain waves and associated phenomena

Depending on the humidity in the air, MTW can be divided into three categories (*Houze*, 2014):

- Dry waves: when no cloud pattern is associated with them.
- Moist reversible waves: when the atmosphere contains enough moisture and the stratification is stable, the air in the cloud begins to sink, and lenticular clouds (altocumulus lenticularis) may form at the wave crests.
- Moist irreversible waves: if there is enough moisture and the stratification is conditionally unstable, deep convection (cumulus cloud formation) may start at the top of the mountain. This usually destroys wavelike streams downstream in reality, but it appears in the mathematical description of the waves as a degenerate solution.

As the moisture and stability has a vertical profile, the different layers of air can produce different types of waves (*Barcilon and Fitzjarrald*, 1985). For example, below a moist reversible layer (i.e. a lenticular cloud) the wave is dry. Multilayered lenticular clouds often appear in this situation. Another example may be a pileus cloud which is a moist reversible wave over a moist irreversible wave.

MTW can also be categorized based on their energy transport into two major types: vertically propagating waves that transport energy to high altitude vertically and trapped lee waves that can extend only to some altitudes.

2.2.1. Vertically propagating waves

Vertically propagating waves occur usually when static stability increases above the mountain top and when the wind speed does not increase significantly with height. They typically extend vertically up to the higher troposphere but evidence for their presence in the stratosphere and mesosphere is also well known (*Schöberl*, 1985; *Bacmeister*, 1993; *Fritts et al.*, 2018).

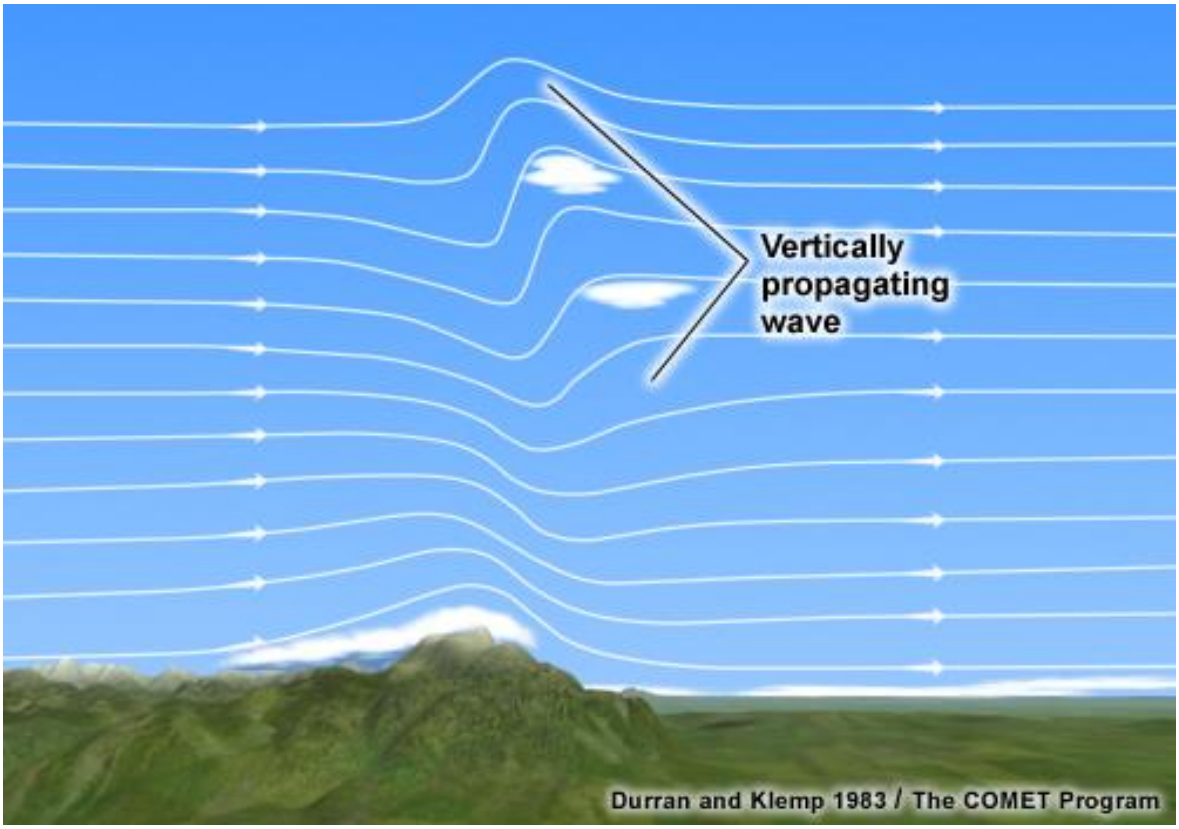

Fig. 2. Illustration of the vertically propagating waves (after Durran and Klemp, 1983).

Their horizontal wavelengths can exceed the order of 10 km. These waves become frequently more amplified and tilt upwind with height (*Sharman et al.*, 2017), however, they

are present only in the vicinity of the mountain (Fig. 2.). This is because the vertical and the horizontal components of these waves' group velocity are in the same order, provoking the carrying out of the energy as it dissipates rapidly downstream, which leads to a smaller overall horizontal extension of the wave pattern (*Lilly and Kennedy*, 1973). This is in contrast with the trapped lee waves.

It was proved in the research of *Bramberger et al.* (2020), that these tilted amplified waves can create strong horizontal wind and temperature gradients leading to flight stall warnings.

2.2.2. Trapped lee waves

Unlike the vertically propagating waves, trapped waves propagate horizontally and can extend over several hundreds of kilometers downstream of a mountain (*Smith*, 1979).

Usually, they have horizontal wavelengths in the order of 100 m to 10 km and they are trapped in a layer with high static stability and medium wind speeds, generally in the lowest 5 km of the troposphere (*Durran*, 1986). They occur when wind speed above the mountain increases sharply with height and/or when stability decreases in a layer above the mountain top. As the wave energy is trapped within the stable layer, these waves can propagate far downwind of the mountain crest (Fig. 3.).

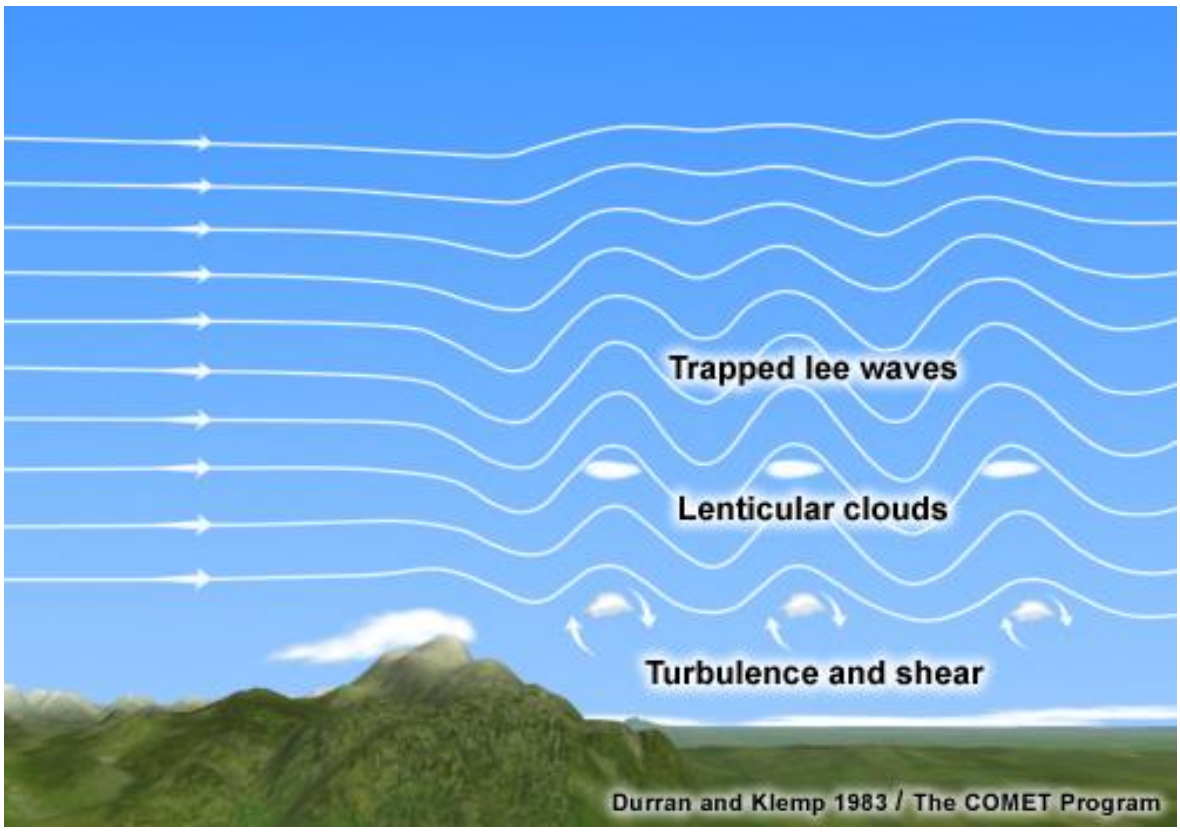

Fig. 3. Illustration of clouds related to trapped lee waves (after Durran and Klemp, 1983).

More detailed studies (*Chunchuzov*, 1994; *Nance and Durran*, 1997; *Ralph et al.*, 1997a, *Hills and Durran*, 2012) report that MTW can have a "non-stationary" behavior. This is mainly because resonant wave modes are sensitive to changes in the average wind and temperature profiles (*Durran*, 2003).

Fig. 4 shows trapped lee wave clouds over southern France, Sardinia, and Tunisia (light pink), while high level cloudiness is present due to vertically propagating lee waves over the Alps (orange). The former consist of water drops and the latter are composed of ice crystals. Since sublimation of the ice crystals in the wave trough is slower than their formation, they remain visible as a homogeneous shield.

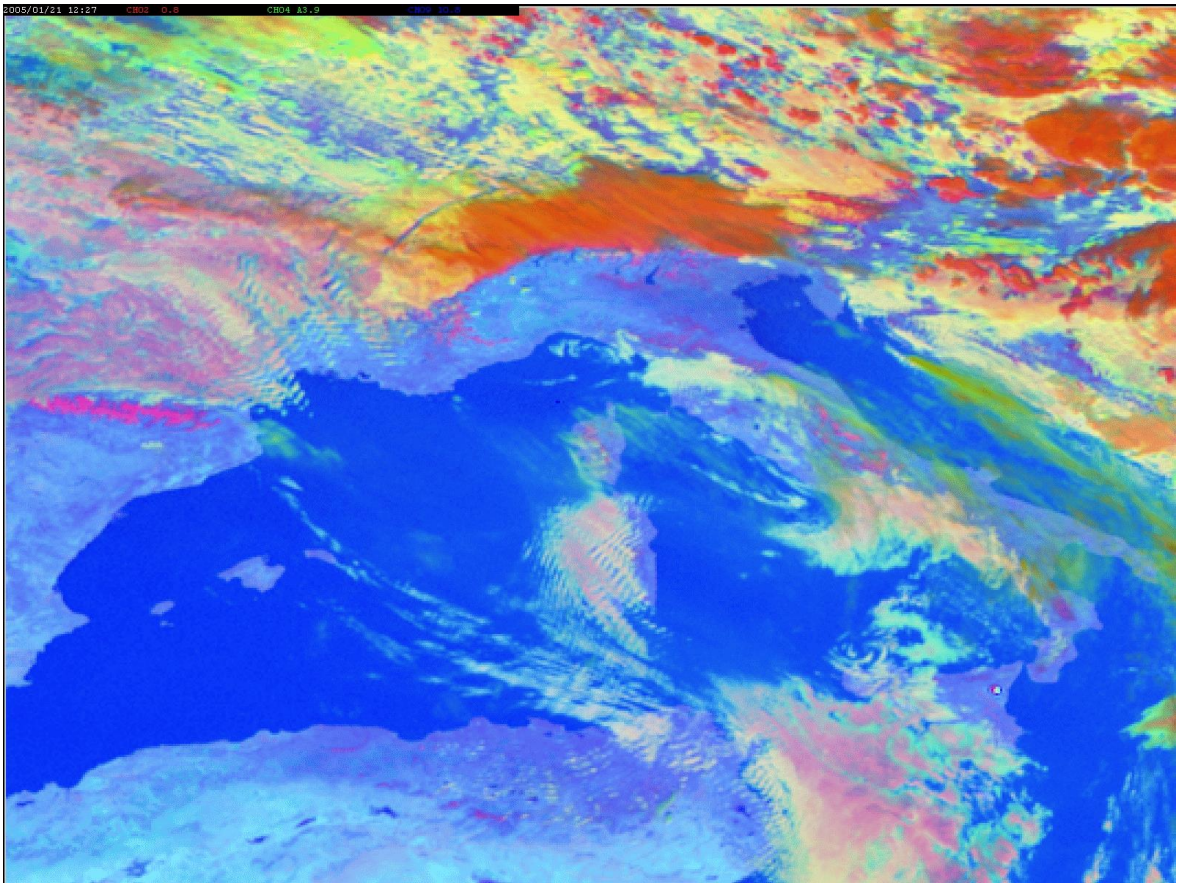

Fig. 4. MSG Daytime Microphysical RGB composite image at 12:00 UTC, 21st January 2005. Light pink colors indicate mid-level cloudiness consisting of water drops. Wave-like pattern is visible in these clouds over southern France, Sardinia and Tunisia. The orange field over the Alps is a high-level cloud shield caused by vertically propagating waves.

2.3. Other Phenomena Associated with MTW.

2.3.1. Cap clouds

Cap clouds often appear above mountain ridges as air is forced to rise on the windward side (Fig. 5.). If the flow is sufficiently humid, the moisture will condense to a cloud bank

that follows mountain contours. As the flow descends in the lee of the mountain ridge, the clouds disappear. Cap clouds can indicate likely wave activities downstream, and their absence doesn't mean that waves are absent because waves may form in drier conditions without cloud formation (*Carney*, 1995; *Downing*, 2013).

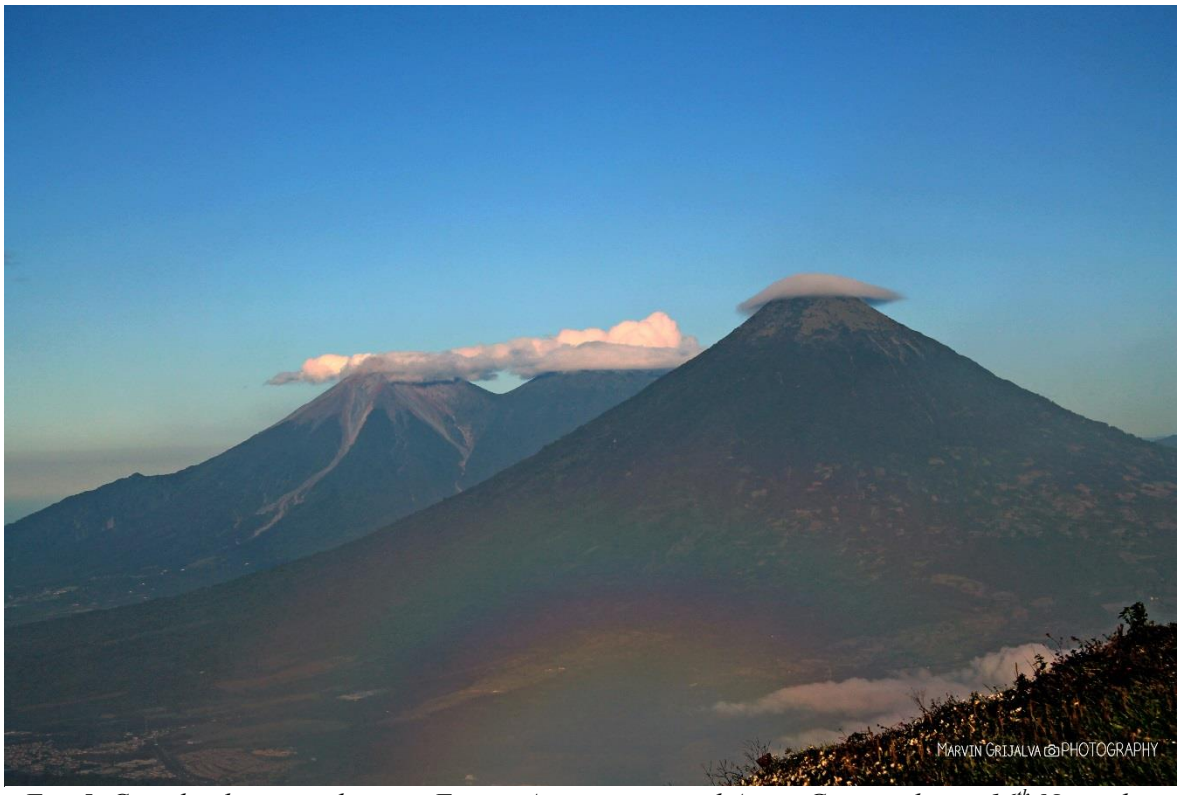

Fig. 5. Cap clouds over volcanoes Fuego, Acatenango, and Agua, Guatemala, on 16th November 2014. A glory on the mist is visible in the foreground. Photo by Marvin Grijalva (Griljava and Foster, 2015).

2.3.2. Downslope windstorms

Strong downslope windstorms may accompany mountain wave systems (*Klemp and Lilly*, 1975), usually associated with strong cross barrier flow and an inversion near barrier top. In extreme cases, wind can exceed 50 m s^{-1} and can lead to severe turbulence and strong wind shear at low altitudes causing significant danger to the pilots (*Smith and Skyllingstad*, 2011). Examples of downslope windstorms are the bora along the northeastern shore of the Adriatic Sea and the Taku wind along the Gastineau Channel in southeast Alaska (*Smith*, 1979), and several other names are known in different cultural regions.

2.3.3. Rotors

The formation of rotors, (appearing often in the form of a horizontal roll vortex), is tightly linked to the pressure force that MTW exerts on the low-level flow in the lee side of a mountain (*Queney*, 1955; *Scorer*, 1955; *Vosper et al.*, 2006). These accelerate the flow under the downwelling wave branches but decelerate it under the upwelling zones. Under the ascending side of a lee-wave, the flow is divergent causing a mass "deficit". Thus, a reverse flow sets up under the wave crest, leading to a flow separation under the descending side of the wave (Fig. 6.). In this case, a closed circulation downwind of the mountain ridge forms, rotating around a horizontal axis parallel to the ridgeline. This stream is called a type 1 rotor. Type 2 rotor can form over a trough of the mountain wave, especially when the wave amplitude decreases rapidly with height, for a similar reason (*Grubišić et al.*, 2015; *Hertenstein and Küttner*, 2016). Numerous aviation accidents have been related to encounters of commercial and general aviation aircraft with rotors (*Udina et al.*, 2020).

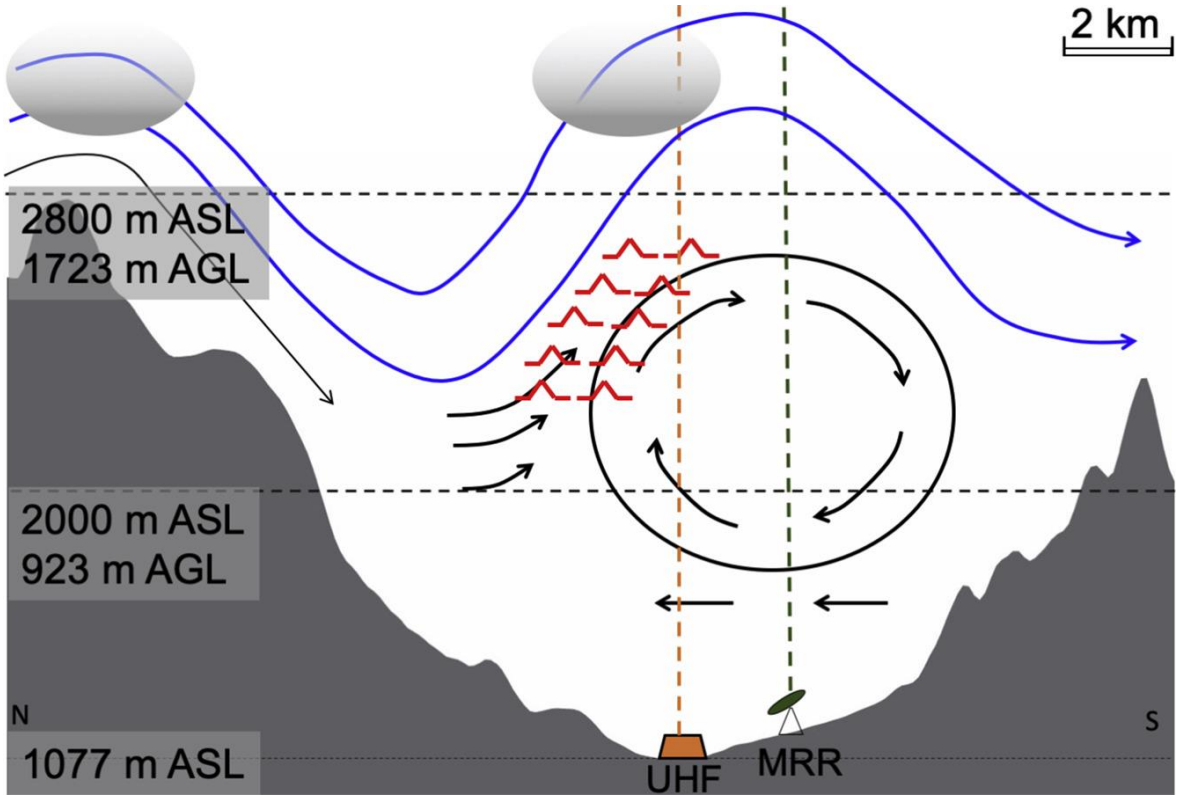

Fig. 6. Illustration of (type 1) rotor formation under a mountain wave crest. Due to surface friction and the divergence under the upwind side of the wave, a reverse streaming appears at low levels, causing a closed circulation under the wave crest (Udina et al., 2020).

Some visual signs of these rotors are the clouds associated with them (*Carney*, 1995), called rotor clouds. It's possible that atmospheric rotors were discovered earlier than mountain waves by Croatian geophysicist Andrija Mohorovičić in the 1920s (*Herak and Herak*,

2007; *Grubišić and Orlić*, 2007). Rotor clouds can develop to cumulus clouds if the moisture is sufficient. They are found near the top of the rotor circulation and often under higher lenticular clouds. Immediately above this cloud, the turbulence decreases significantly. Since the rotor can become convectively unstable in some situations, the downdraft of the rotors can be severely turbulent. This phenomenon may be called "rotor breaking", is similar to the wave breaking phenomena in the higher troposphere (*Smith*, 2003; *Kozhevnikov et al.*, 2020).

Vertically propagating and trapped lee waves can coexist. As the formation of rotors can be different associated with the individual wave modes, these rotors can interact and affect the wave-induced streaming in a complex way. This can lead to the appearance of unusual patterns in, for example, the rotor clouds or the associated turbulence (*Grubišić et al.*, 2008).

2.3.4. Breaking waves

The vertical wind shear has an important effect on the MTW. Increasing wind speed with height can cause the mountain wave crests to tilt towards the downwind side. Reaching a critical value, wave slopes get steeper until the wave crest overturns the lower part. In this case, an air parcel of higher density becomes placed above air of lower density. This leads to convective instability and causes a sudden increase in downdraft velocity. As a consequence, the flow becomes severely turbulent (*Smith*, 1979; *Ralph et al.*, 1997b; *McHugh and Sharman*, 2013).

2.4. The linear theory of mountain waves

As passing wind over mountains is forced to rise, kinetic energy is transformed into potential energy. Fluid parcels tend to return to their original height if the stratification is stable. In this case, gravity and buoyancy together serve as a restoring force, and the parcels begin to oscillate, thus, atmospheric internal waves develop (*Holton*, 2013), Atmospheric conditions during the winter season are more favorable to the development of mountain waves because of the stable stratification in the lower troposphere.

Orlanski (1975) categorized atmospheric phenomena by their characteristic size and lifetime (Fig. 7.). According to this, short gravity waves (including for example Kelvin-Helmholtz waves) belong to Micro-α (200 m to 2 km) scale. Mountain winds and inertial waves usually belong to Meso-β (20 km to 200 km), CAT and internal gravity waves are considered to Meso-γ (2 km to 20 km). Mountain waves in general, however, can have either shorter or longer horizontal wavelength, so they are an example of phenomena of which the spatial

scale spans through several scales, namely from Micro-α to Meso-β (Micro-α is often named Meso-δ). Moreover, characteristic size and time of mountain waves can be interpreted in two contexts: a) their wavelength and time period of oscillations and b) in the case of trapped waves, the area affected by the waves and the time for which the waves are present. This is determined usually by the synoptic situation (mainly the frontal systems), usually at the Meso-α scale.

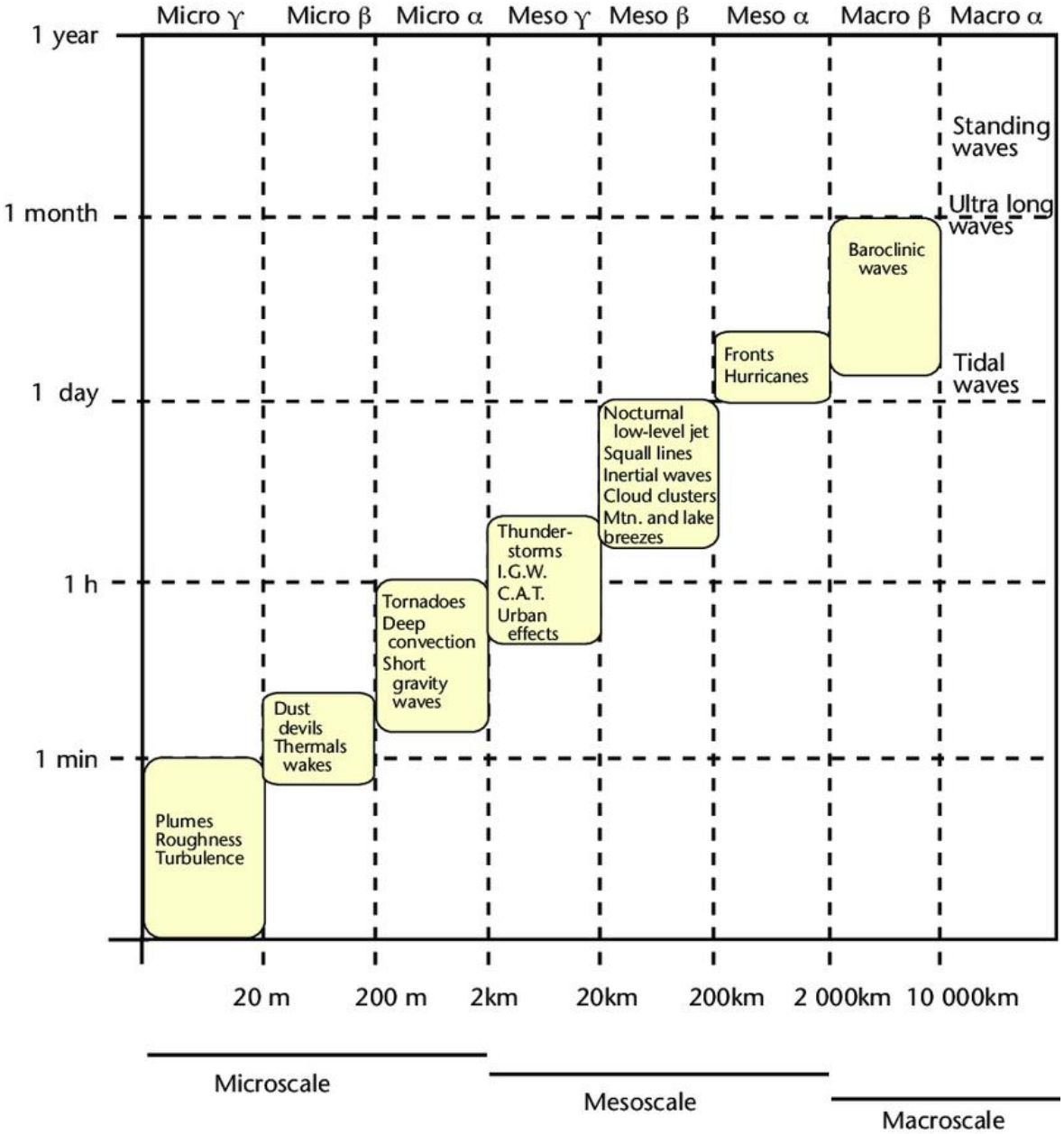

Fig. 7. Categorization of atmospheric phenomena by Orlanski (1975). Internal gravity waves belong usually to Meso-γ scale.

In the next subsections, the major concepts of the linear theory introduced by *Scorer* (1949), and the analytical description of the MTW and its derivation via the vertical velocity

perturbation will be discussed. Four special cases will be solved analytically giving explanations for some concepts arising in this linear theory (Table 1).

Table 1. Special cases and concepts introduced by linear theory. Periodic mountains are represented with a sinusoid function, while isolated mountain with a Fourier-transformable function (here an Agnessi-function). In the one-layer atmosphere, the Scorer-parameter (as well as the horizontal wind and the BV-frequency) is assumed to be constant, while in the two-layer atmosphere, two layers of differing parameters (but constant with height in each layer) are considered.

	One-layer atmosphere	Two-layer atmosphere
Periodic mountains (sinusoid)	Monochromatic solution Vertically periodic/evanescent Wave tilting	Vertically propagating waves
Isolated mountain (Agnessi-function)	Wave reflection Monochromatic resonance	Discrete trapping Horizontally periodic solution Upper layer solution

2.4.1. Governing equations

$$\frac{\partial \rho u_i}{\partial t} + u_j \partial_j (\rho u_i) = -\rho g_i - 2\varepsilon_{ijk}\Omega_j u_k - \partial_i p - \eta \partial_j \partial_j u_i - \frac{\eta}{3}\partial_i \partial_j u_j \tag{1a}$$

$$\frac{\partial \theta}{\partial t} + u_j \partial_j \theta = \nu \partial_j \partial_j \theta - \frac{\partial_j Q_j^* + L_F E}{\rho c_{pd}} \tag{1b}$$

$$\frac{\partial \rho}{\partial t} + \partial_j (\rho u_j) = 0 \tag{1c}$$

Equations (1) describe the atmospheric hydro-thermodynamic equation system, the Navier-Stokes equations of motion (1a), the thermodynamic equation expressed with potential temperature (1b) and the continuity equation (1c). For vector quantities, we use the Einstein summation convention.

Here, ρ is density, $u_j = (u, v, w)$ the wind components, $g_i = (0,0,g)$ is gravity, $\Omega_j = (0, \Omega \sin\varphi\,, \Omega \cos\varphi)$ is Earth's rotation at latitude φ, p is pressure, η is dynamic viscosity, θ is potential temperature, ν is thermal conductivity, Q_j^* is radiation, $L_F E$ is latent heat and c_{pd} is specific heat at constant pressure.

Several simplifications can be made to the equation system based on the characteristic behavior of the mountain waves.

1. Incompressibility: $\frac{d\rho}{dt} = 0 \Rightarrow \partial_j u_j = 0$
2. Rotation of Earth is neglected
3. Inviscid fluid
4. Radiation and latent heat is neglected
5. Stationary flow: $\frac{\partial}{\partial t} = 0$
6. Reynolds-decomposition: variables can be written as the sum of their average (denoted with an overbar) and a perturbation (denoted with a prime): $A = \overline{A} = A'$.

Average quantities represent synoptic scale situation (which leads to further simplifications), while perturbations describe the waves. At this point, the equation system is as follows:

$$(\overline{\rho} + \rho')\left(\overline{u}_j + u_j'\right)\partial_j(\overline{u}_i + u_i') + (\overline{\rho} + \rho')g_i + \partial_i(\overline{p} + p') = 0 \tag{2a}$$

$$\left(\overline{u}_j + u_j'\right)\partial_j\left(\overline{\theta} + \theta'\right) = 0 \tag{2b}$$

$$\partial_j u_j' = 0 \tag{2c}$$

7. Linearization (to obtain wave solution): We assume that primed quantities are small enough to neglect terms with their product, i.e. $A' \ll \overline{A} \Rightarrow A'B' \approx 0$. With this, turbulence is neglected.
8. The average state of the atmosphere is in hydrostatic equilibrium: $\partial_i \overline{p} + \overline{\rho} g_i = 0$
9. Boussinesq approximation: $\rho' \ll \overline{\rho}$. Note that $\rho' g_i$ will remain in the equation because $\overline{\rho} g_i$ already vanished due to the hydrostatic approximation.
10. Two-dimensional description in (x, z) plane: $v = \frac{\partial}{\partial y} = 0$
11. Average state of the atmosphere is horizontally homogeneous: $\frac{\partial \overline{A}}{\partial x} = 0$
12. Average vertical velocity can be neglected: $\overline{w} = 0$
13. Density can be exchanged with potential temperature. After dividing the equations of motion with $\overline{\rho}$, terms with $\frac{\rho'}{\overline{\rho}}$ appear. Reynolds-decomposing the ideal gas law $p = \rho R T$ and applying Poisson's equation leads to $\frac{\rho'}{\overline{\rho}} = -\frac{\theta'}{\overline{\theta}}$.
14. Other variables can be introduced:
    a. Buoyancy: $b = g\frac{\theta'}{\overline{\theta}}$
    b. Brunt-Väisälä frequency: $N^2 = \frac{g}{\overline{\theta}}\frac{\partial \overline{\theta}}{\partial z}$
    c. Reduced pressure: $P' = \frac{p'}{\overline{\rho}}$

The equation system reduces to the following:

$$\overline{u}\frac{\partial u'}{\partial x} + w'\frac{\partial \overline{u}}{\partial z} + \frac{\partial P'}{\partial x} = 0 \tag{3a}$$

$$\overline{u}\frac{\partial w'}{\partial x} + \frac{\partial P'}{\partial z} = b \tag{3b}$$

$$\overline{u}\frac{\partial b}{\partial x} + w'N^2 = 0 \tag{3c}$$

$$\frac{\partial u'}{\partial x} + \frac{\partial w'}{\partial z} = 0 \tag{3d}$$

The equations are the horizontal (3a) and vertical (3b) equation of motion, the thermodynamic equation expressed with buoyancy (3c) and the continuity equation (3d).

2.4.2. Wave equation

Equation system (3) describes has wave solutions which includes mountain waves. Independent variables are the horizontal (u') and vertical (w') wind perturbations, the buoyancy (b) and the reduced pressure (P'). Assuming wave form solution for all variables would lead to a general dispersion relation of this equation system. However, we are interested in the vertical velocity in the stationary mountain waves, thus, we will eliminate the other variables.

Equation (3a) can be derived with respect to z and equation (3b) with respect to x, and subtracting them will eliminate P'. The buoyancy gradient from equation (3c) can be substituted and then terms of u' can be exchanged with terms of w' using (3d). The only variable remaining will be w', leading to a linear partial second-order homogeneous differential equation, with a functional coefficient $\ell^2(z)$, the Scorer-parameter.

$$\left[\frac{\partial^2}{\partial x^2} + \frac{\partial^2}{\partial z^2} - \left(\frac{N^2}{\overline{u}^2} - \frac{1}{\overline{u}}\frac{\partial^2 \overline{u}}{\partial z^2}\right)\right] w' = 0 \tag{4a}$$

$$\ell^2(z) = \frac{N^2}{\overline{u}^2} - \frac{1}{\overline{u}}\frac{\partial^2 \overline{u}}{\partial z^2} \tag{4b}$$

The Scorer-parameter is related to the Brunt-Väisälä frequency (the static stability) and the average horizontal wind profile. Its first term is the stability term and it often dominates, but the second term (shear curvature) of the velocity profile can be of similar magnitude, especially when the wind shear changes sharply with height, often near the surface and in the vicinity of a jet streak.

2.4.3. Dispersion relation

We assume that the vertical velocity perturbation has a wave solution with W amplitude and (k_x, k_z) horizontal and vertical wavenumbers.

$$w'(x,z) = We^{i(k_x x + k_z z)} \tag{5}$$

Substituting this into equation (4a) gives the dispersion relation:

$$\ell^2 = k_x^2 + k_z^2 \tag{6}$$

This is a Pythagore-equation, so the square-root of the Scorer-parameter can be interpreted as the length of the total wavenumber vector of the inner gravity wave.

To establish a correct upper boundary condition, we will need the group velocity which cannot be derived from a stationary dispersion relation. Thus, calculations are needed to be repeated without assuming stationarity of the flow. When Reynolds decomposition is carried out, time derivatives of the averages can be neglected. After applying Boussinesq approximation, the time derivative of the velocity perturbations and buoyancy appears in the equations:

$$\frac{\partial u'}{\partial t} + \overline{u}\frac{\partial u'}{\partial x} + w'\frac{\partial \overline{u}}{\partial z} + \frac{\partial P'}{\partial x} = 0 \tag{7a}$$

$$\frac{\partial w'}{\partial t} + \overline{u}\frac{\partial w'}{\partial x} + \frac{\partial P'}{\partial z} = b \tag{7b}$$

$$\frac{\partial b}{\partial t} + \overline{u}\frac{\partial b}{\partial x} + w'N^2 = 0 \tag{7c}$$

$$\frac{\partial u'}{\partial x} + \frac{\partial w'}{\partial z} = 0 \tag{7d}$$

We will, again, eliminate variables and leave only w', however, the steps are now more complicated. The differential operator is far more complex and, to be precise, applying stationarity to this equation leads to the second horizontal derivative of the original stationary Scorer-equation (4a). Two forms of this equation can be derived.

$$\left[\left(\frac{1}{\overline{u}}\frac{\partial}{\partial t} + \frac{\partial}{\partial x}\right)^2\left(\frac{\partial^2}{\partial x^2} + \frac{\partial^2}{\partial z^2}\right) + \ell^2\left(\frac{1}{\overline{u}}\frac{\partial}{\partial t} + \frac{\partial}{\partial x}\right)\frac{\partial}{\partial x} - \frac{N^2}{\overline{u}^3}\frac{\partial^2}{\partial t \partial x}\right]w' = 0 \tag{8a}$$

$$\left[\left(\frac{1}{\overline{u}}\frac{\partial}{\partial t} + \frac{\partial}{\partial x}\right)^2\left(\frac{\partial^2}{\partial x^2} + \frac{\partial^2}{\partial z^2}\right) + \frac{N^2}{\overline{u}^2}\frac{\partial^2}{\partial x^2} - \frac{1}{\overline{u}}\frac{\partial^2 \overline{u}}{\partial z^2}\left(\frac{1}{\overline{u}}\frac{\partial}{\partial t} + \frac{\partial}{\partial x}\right)\frac{\partial}{\partial x}\right]w' = 0 \tag{8b}$$

Equation (8a) contains the Scorer-parameter directly. Equation (8b), in turn, is convenient as the wind shear curvature is often small enough to make the last term in (8b) negligible. Substituting a wave solution with ω frequency will lead to the following dispersion relation:

$$\omega = \overline{u}k_x \pm \frac{Nk_x}{\sqrt{k_x^2 + k_z^2}} \tag{9}$$

2.4.4. Group and phase velocities

Group velocity in wave mechanics is the velocity of a wave group or "packet", that carries the energy of the wave as it propagates. Its components can be defined by deriving the frequency with respect to the appropriate wavenumber components:

$$c_{g_x} = \overline{u} \pm \frac{Nk_z^2}{(k_x^2+k_z^2)^{\frac{3}{2}}} \tag{10a}$$

$$c_{g_z} = \mp \frac{Nk_xk_z}{(k_x^2+k_z^2)^{\frac{3}{2}}} \tag{10b}$$

Phase velocity is the velocity at which the phase lines propagate. Dividing the frequency with the wavenumber components will give the components of the phase velocity.

$$c_{f_x} = \overline{u} \pm \frac{N}{\sqrt{k_x^2+k_z^2}} \tag{11a}$$

$$c_{f_z} = \overline{u}\frac{k_x}{k_z} \pm \frac{Nk_x}{k_z\sqrt{k_x^2+k_z^2}} \tag{11b}$$

For the inner gravity waves, the phase and group velocities are perpendicular to each other, meaning that their inner product is zero. This is true for the lower signs.

2.4.5. Wavelength

The wavelength $L_i = \frac{2\pi}{k_i}$ is the distance between two points with the same phase. Usually, short length waves occur in very stable atmospheric conditions with low wind speeds while high wind speeds and a less stable atmosphere generate longer wavelengths. This is, however, not necessary and in general, internal gravity waves with practically every wavelength are present in the atmosphere and their propagation is determined by the profile of the Scorer-parameter. Their amplitudes, as a function of wavelength, constitute the spectrum of these waves. For example, the shape of an orographic barrier determines the spectrum of the initiated internal gravity waves.

2.4.6. Boundary conditions

There are two boundary conditions, one at the ground and one at the top of the atmosphere. The ground surface boundary condition is that the overall wind velocity vector at the ground has to be tangential of the terrain, i.e. the stream should follow the terrain (this is called a free-slip condition). If the height of the ground is described with the function $h(x)$, this will lead to the following equation.

$$w'\big(x, h(x)\big) = \overline{u}\big(h(x)\big)\frac{dh(x)}{dx} \tag{12}$$

When the mountains are small compared to the depth of the atmosphere, $h(x) \approx 0$ is true.

The upper boundary condition is either that the wave amplitude must vanish at infinite height or, if this is not the case (which is for positive N^2), that energy should not arrive into the atmosphere from Space, i.e. the vertical group velocity component has to be positive. Choosing k_x positive, and with the lower sign, this states that k_z should also be positive, which results in waves tilted "backwards", against the average wind with height.

2.5. General solutions in special cases

2.5.1. One-layer atmosphere, periodic terrain

In this case, the atmosphere is characterized by a constant horizontal velocity $\overline{u}$ and BV-frequency N^2, and thus constant Scorer-parameter ℓ^2, with respect to height. The terrain is described by a series of sinusoid hills with H height, L hill distance and $K = \frac{2\pi}{L}$ "hill number":

$$h(x) = H \sin Kx \tag{13}$$

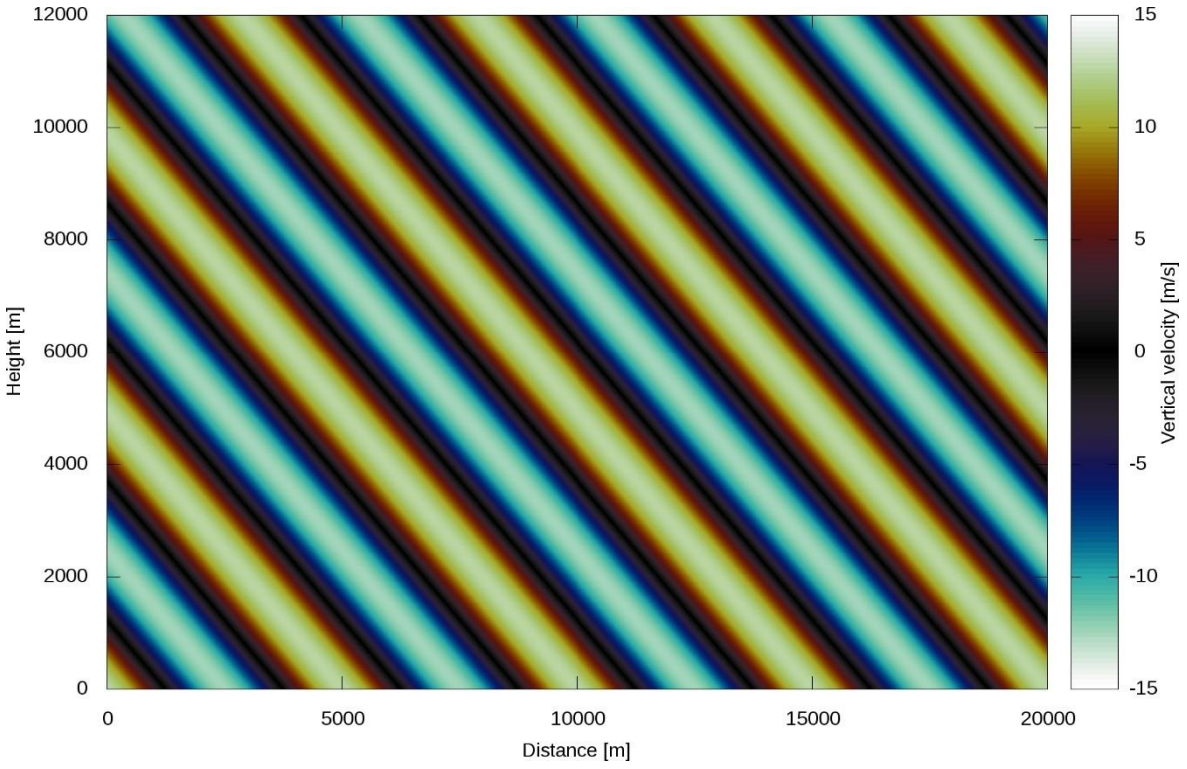

Fig. 8. Vertically periodic monochromatic waves. $L = 5\ km$, $H = 1\ km$, $\overline{u} = 10\ m\ s^{-1}$, $T(z = 0) = 300\ K$, $p(z = 0) = 1000\ hPa$, $\gamma = 0$, $K = 1.2567\ km^{-1}$, $N = 0.017866\ s^{-1}$, $\ell = 1.7866\ km^{-1}$, $W = 12.566\ m\ s^{-1}$, *wave tilting angle* $\alpha = 45.3°$, *terrain slope* $\beta = 51.5°$ *(*$\alpha = \beta \Rightarrow \gamma = 2.69\ K\ km^{-1}$ *and* $\alpha = 0 \Rightarrow \gamma = -4.932\ K\ km^{-1}$*).*

The effect of this terrain is a monochromatic wave solution. A solution, which is the real part of equation (5), fulfilling the lower boundary conditions has the properties $k_x = K$ and $W = \overline{u}HK$, the dispersion relation becomes $k_z^2 = \ell^2 - K^2$ and $\ell = \frac{N}{\overline{u}}$, and the solution is

$$w'(x,z) = \overline{u}HK\cos\left(Kx + \sqrt{\ell^2 - K^2}z\right) \tag{14}$$

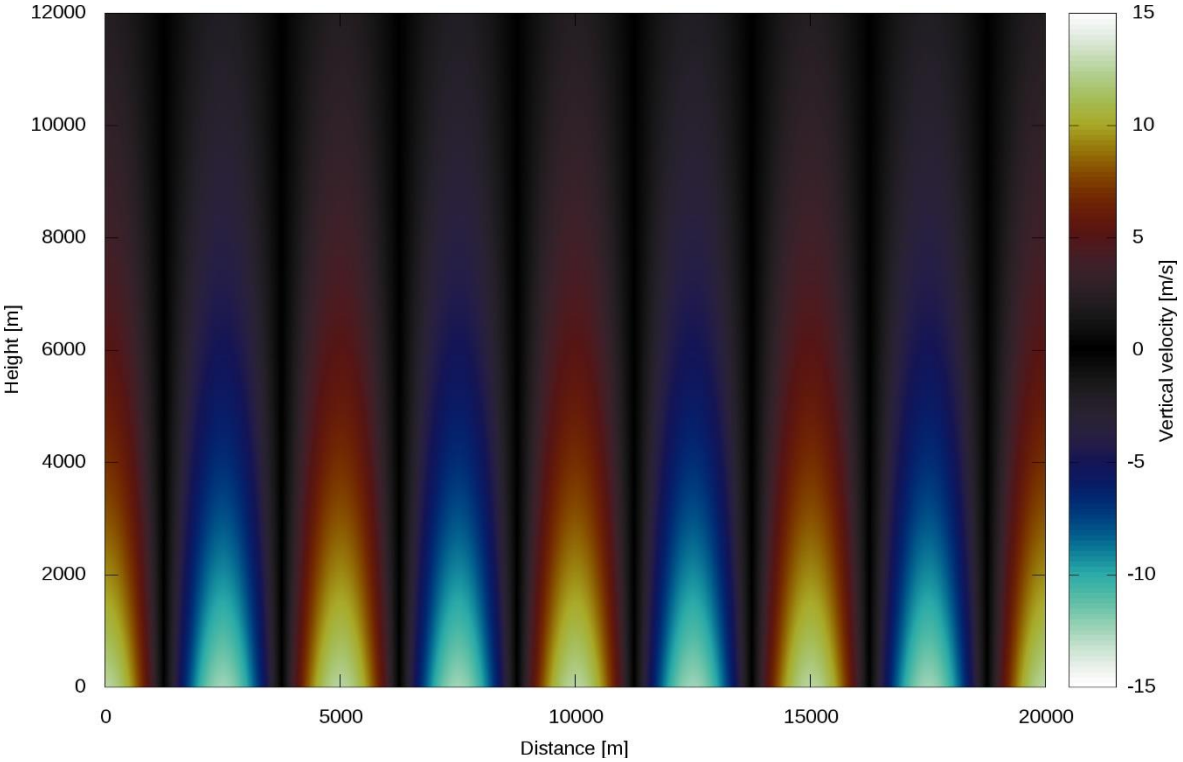

Fig. 9. Vertically evanescent monochromatic waves. $L = 5\ km$, $H = 1\ km$, $\overline{u} = 10\ m\ s^{-1}$, $T(z=0) = 300\ K$, $p(z=0) = 1000\ hPa$, *the temperature gradient is* $\gamma = -5\ K\ km^{-1}$, $K = 1.2567\ km^{-1}$, $N = 0.012478\ s^{-1}$, $\ell = 1.2478\ km^{-1}$, $W = 12.566\ m\ s^{-1}$

As K is given, the term under the square root (the vertical wavenumber) can be either positive or negative depending on the Scorer-parameter. The positive solution will be periodic in vertical (Fig. 8) while the negative will be evanescent (Fig. 9). If the waves are evanescent in vertical, the upper boundary condition will be automatically fulfilled. If the waves are periodic in vertical, the vertical component of the group velocity should be positive, this will result in waves tilted "backwards" against the average wind with height.

The angle to the vertical of the phase lines can be calculated from the wavelengths leading to the following:

$$\mathrm{tg}\alpha = \frac{L}{L_z} = \sqrt{\left(\frac{L\ell}{2\pi}\right)^2 - 1} \tag{15}$$

This tilting angle cannot exceed the maximal angle of the slope, otherwise the streamlines would intersect (Fig. 10). This leads to an upper limit for the stability for a given average wind:

$$\mathrm{tg}\alpha < \mathrm{tg}\beta \Rightarrow N^2 < \left(2\pi\frac{\overline{u}}{L}\right)^2\left(1+\left(2\pi\frac{H}{L}\right)^2\right) \tag{16}$$

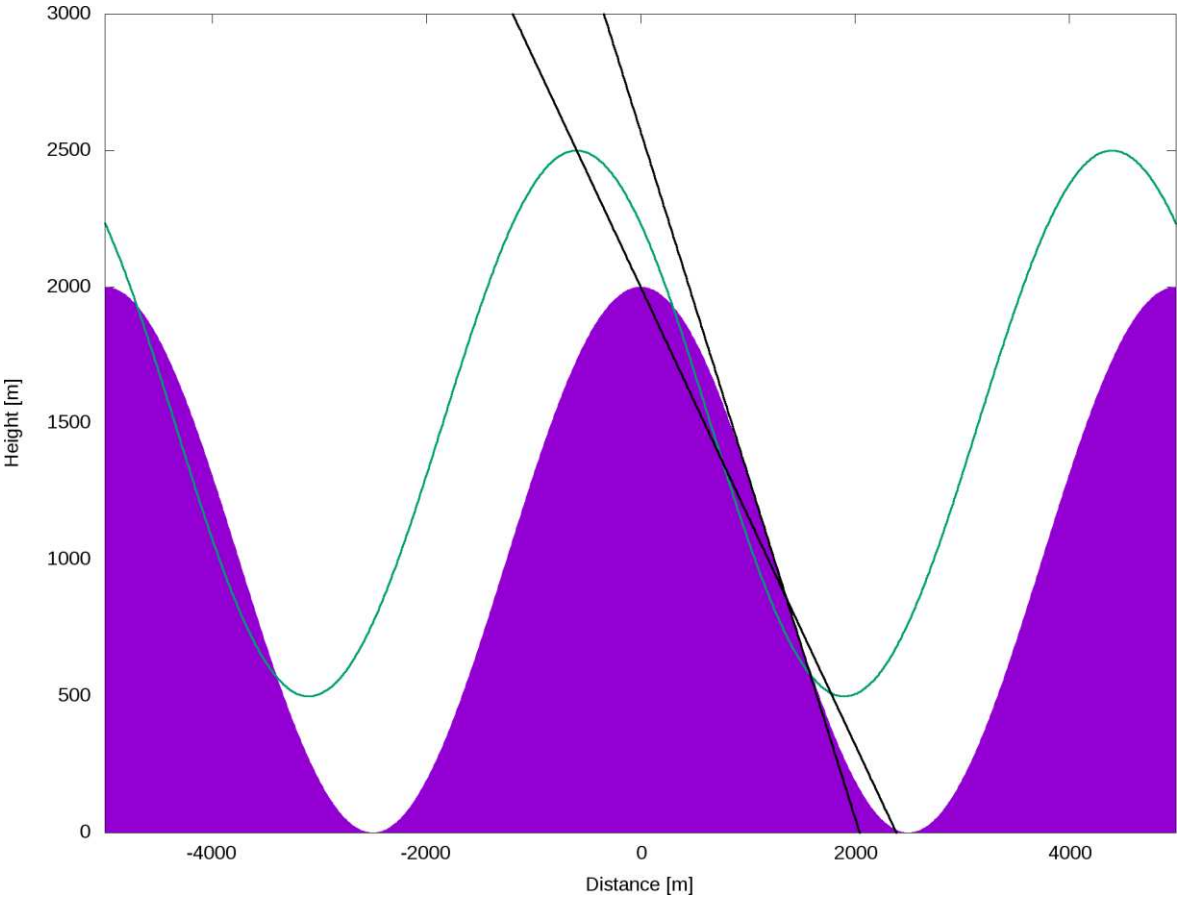

Fig. 10. Illustration of what happens if the wave tilting is too high. Streamlines (green) would intersect each other and even penetrate into the ground.

The condition which separates the periodic and evanescent waves is that the vertical wavenumber is exactly zero. This leads to $\ell = K$ and then $\frac{NL}{\overline{u}} = 2\pi$. The stability of the air, thus, has to be inside a range to have vertically periodic waves. Low stability will cause the waves to be evanescent in vertical, while high stability will cause them to tilt too much resulting in streamlines crossing each other.

2.5.2. One-layer atmosphere, isolated mountain

The terrain, in this case, can be described with any Fourier-transformable function. In this case, waves with practically all horizontal wavelengths are generated and the superposition principle holds. A range of these waves will be vertically periodic while others will be evanescent.

Applying Fourier-transformation to the problem by x will lead to the following solution (Fig. 11). Note that this is often referred to as the general solution in which vertical dependence is noted in $\overline{u}(z)$ and $\ell^2(z)$ but that is only approximately true if they change only slowly with height. Here, asterisk denotes convolution and $\mathcal{F}_{k_x}^{-1}$ is the inverse Fourier transformation with respect to the horizontal wavenumber.

$$w'(x,z) = \overline{u}\frac{dh}{dx} * \mathcal{F}_{k_x}^{-1}\left\{e^{i\sqrt{\ell^2-k_x^2}z}\right\} \tag{17}$$

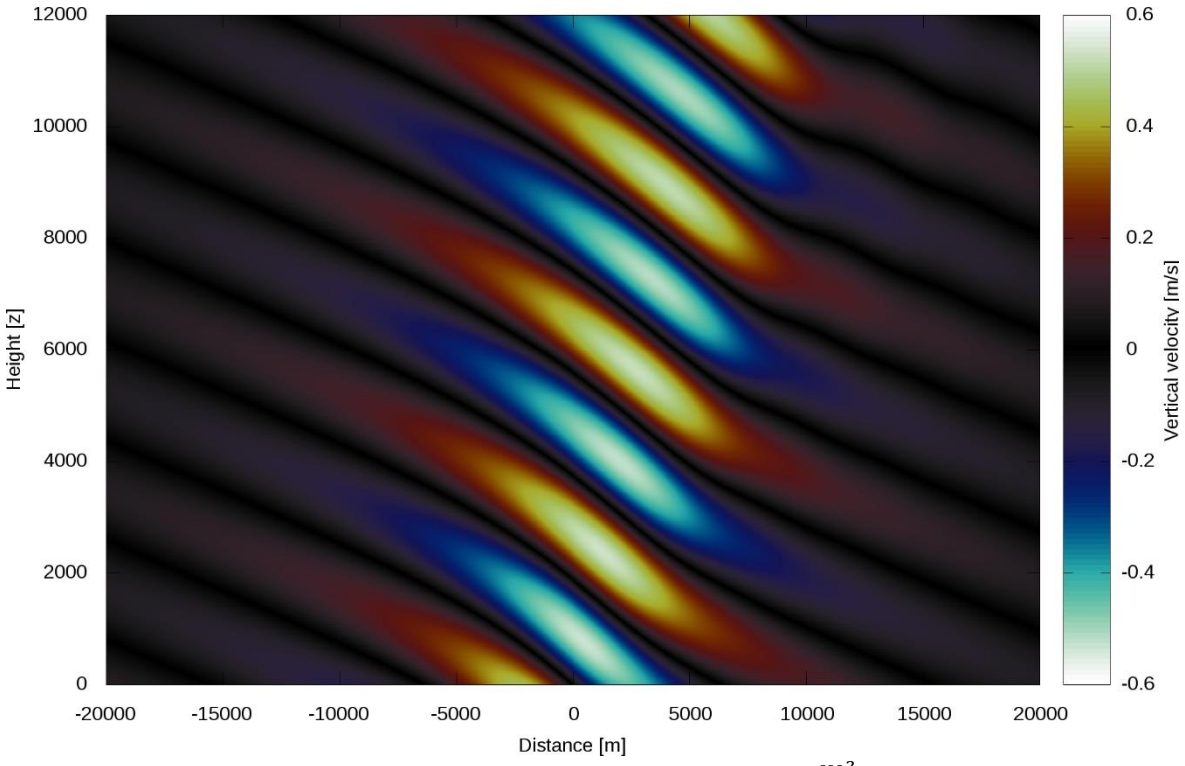

Fig. 11. Mountain waves over an isolated mountain. Here, $h(x) = \frac{HL^2}{x^2+L^2}$ is the shape of the mountain, where $H = 1\ km$ its height, $L = 2.5\ km$ is its half-height width, $\gamma = 0$ and $\overline{u} = 10\ m\ s^{-1}$.

2.5.3. Two-layer atmosphere, periodic terrain

In this case, we consider that the atmosphere has two layers of different Scorer-parameters being constant in each layer. The layer boundary is at height Z. Wave reflection and transmission occurs on this layer boundary. The existence of such a boundary is often responsible for wave trapping, the appearance of rotors, and can induce severe turbulence in lower layers (mainly CAT).

Lower layer variables will be denoted with index L, and upper layer variables with index U. We assume a free-slip boundary condition between the two layers which gives:

$$\frac{w_L'(x,Z)}{\overline{u}_L(Z)} = \frac{w_U'(x,Z)}{\overline{u}_U(Z)} \tag{18}$$

The monochromatic wave reflected from the layer boundary with a reflection coefficient r has negative vertical group velocity component. The ground surface is assumed to reflect waves without loss of amplitude. Thus, a wave will become the superposition of a downward and an upward propagating mode with amplitude $W_n = W_0 r^n$ after n reflections. The wave field of the lower layer is calculated as the superposition of all waves after infinite reflections, the amplitude will be modified with the reflection coefficient:

$$W = \overline{u} HK \left(\frac{2r}{1-r} + 1 \right) \tag{19}$$

Wave trapping (resonance) happens if the reflection coefficient for a wave mode is one. The favorable condition for trapping is when the wave is vertically periodic in the lower layer and evanescent in the upper layer. Utilizing the free-slip condition between the layers, this leads to a condition on the difference between the Scorer-parameters as follows:

$$\ell_L^2 - \ell_U^2 > \left(\frac{\pi}{2Z} \right)^2 \tag{20}$$

Note that resonance (i.e. $r = 1$) will lead to infinite amplitude. This will break many of the assumptions, most notably that perturbations are small. Neglected secondary phenomena (e.g. molecular viscosity, turbulent viscosity, in case of cloud formation the latent heat, etc.) will come to effect and carry away energy from the waves, so the wave amplitude won't be infinity in reality. These phenomena are highly nonlinear and thus cannot be quantified within this theory.

2.5.4. Two-layer atmosphere, isolated mountain

For an isolated mountain, the amplitudes in the Fourier-transformation of the mountain gives always the initial spectrum of the waves. The reflection coefficient is assumed to be dependent on the horizontal wavenumber. This leads to the following general solution in the lower layer:

$$w_L'(x,z) = \overline{u}_L \frac{dh}{dx} * \mathcal{F}_{k_x}^{-1} \left\{ \left(\frac{2r(k_x)}{1-r(k_x)} + 1 \right) \cos \sqrt{\ell_L^2 - k_x^2}\, z \right\} \tag{21}$$

Trapped waves, for which $r = 1$, have formally infinite amplitude. This means that any other wave modes can be neglected besides them. As the necessary condition for trapping is that the wave is vertically periodic in the lower layer and evanescent in the upper layer, and the horizontal wavenumber of that wave has to be between the Scorer-wavenumbers of the two layers, i.e. $\ell_U^2 < k_x < \ell_L^2$. Besides, $r = 1$ is assumed only for those waves for which the layer depth is a multiple of their half vertical wavelength, i.e. $Z = j \frac{L_Z}{2}$ where j is a positive integer.

Horizontal wavenumber of those waves which fulfill these conditions can be calculated, and applying the necessary condition for trapping will lead to a condition for j:

$$\frac{2Z}{\pi}\sqrt{\ell_L^2 - \ell_U^2} > j > 0 \tag{22}$$

From this, for a given layer depth and known Scorer-parameters, we can calculate the maximal j and if $j \geq 1$, there will be a resonant wave mode. More precisely, $\lfloor j \rfloor$ indicates the number of trapped wave modes. This can be applied to a numerical model output: choosing a grid point at a given time and obtaining the Scorer-parameter profile, we can approximate the profile with a two-layer model with different Z values and calculate j for every possible Z. Of course, this can be done for every grid point at any every to obtain a 3D time-dependent field of j values.

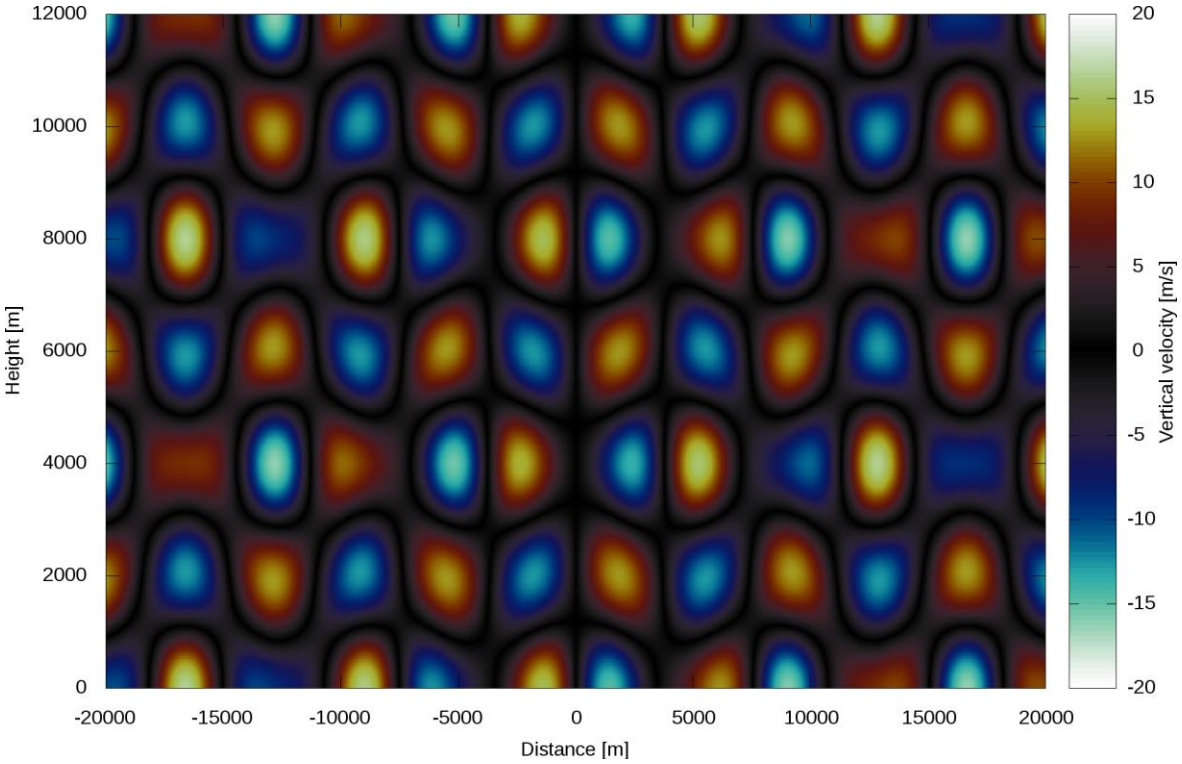

Fig. 12. Trapped mountain waves initiated by an isolated mountain. Here, $h(x) = \frac{HL^2}{x^2+L^2}$ is the shape of the mountain, where $H = 1\ km$ its height, $L = 2.5\ km$ is its half-height width, $\overline{u}_L = 10\ m\ s^{-1}$, $\overline{u}_U = 30\ m\ s^{-1}$, $T(z=0) = 300\ K$, $\gamma_L = 0$, $\gamma_U = -4.88\ K\ km^{-1}$, $Z = 4\ km$, $\ell_L^2 = 3.2\ km^{-2}$, $\ell_U^2 = 0.177\ km^{-2}$, $R = 1$ is chosen for all waves. The trapped waves have wavelengths $L_{x_1} = 3.92\ km$ and $L_{x_2} = 7.38\ km$. Note that the whole figure shows the lower layer solution in spite of the lower layer ends at height Z.

The inverse Fourier transformation in the solution will fall back to a finite series leading to a horizontally periodic result (Fig. 12). This can be interpreted as the explanation of why trapped lee waves can cover a wide area far downstream from the mountain.

$$w'_L(x,z) = \frac{\overline{u}_L}{\sqrt{2\pi}} \int_{-\infty}^{\infty} \frac{dh(x')}{dx'} \sum_{j=1}^{\frac{2Z}{\pi}\sqrt{\ell_L^2-\ell_U^2}} R_j \cos\frac{j\pi z}{Z} \cdot e^{i\sqrt{\ell_L^2-\left(\frac{j\pi}{Z}\right)^2}(x-x')}\, dx' \qquad (23)$$

As it was stated in subsection 2.5.3, secondary phenomena carry energy from the waves keeping their amplitude finite. The R_j coefficient stands now in place of the expression of the reflection coefficient which is unknown but can be considered finite. Equation (23) can be applied to any measured sounding and if vertical wind speeds of trapped mountain waves can be measured – for example with an array of SODARs or LIDARs –, it might be possible to give estimates for R_j.

2.5.5. Solution for upper layer

In the case of a two-layer atmosphere over an isolated mountain, it might be interesting to solve the upper layer problem. As the layer boundary at height Z is a free boundary, the stream in the lower layer will affect the shape of the layer boundary.

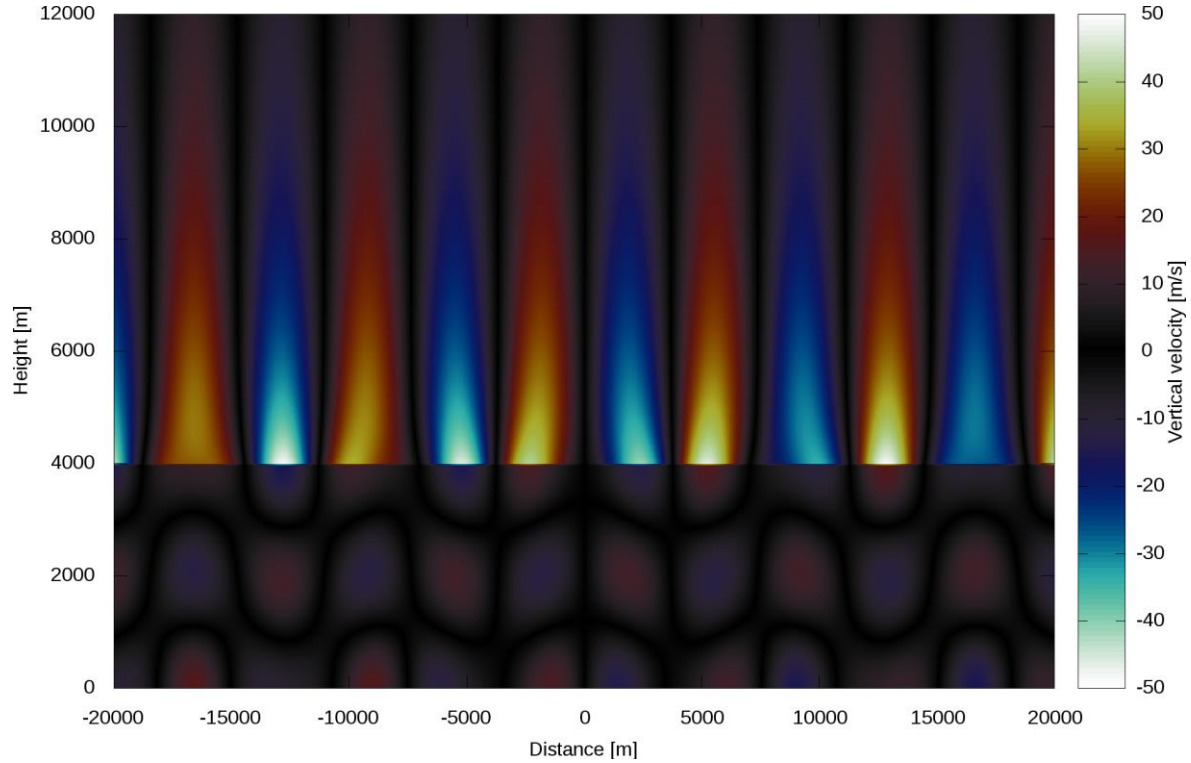

Fig. 13. Same as Fig. 12, but with the upper layer solution shown over $Z = 4\ km$. The sudden increase of w' visible at layer boundary is a consequence of the middle boundary condition and that the horizontal velocity is higher in the upper layer. The different damping factors of the waves are $\kappa_1 = 1.6937\ km^{-1}$ and $\kappa_2 = 1.2787\ km^{-1}$.

This layer boundary behaves as a "terrain" for the upper layer and the analytical solution can be derived in the upper layer assuming a one-layer atmosphere over the layer boundary. The boundary condition between the two layers can be applied to the lower layer solution at

Z to obtain a lower boundary condition for w'_U in the upper layer. Then, the upper layer solution will become the superposition of evanescent waves with the horizontal wavenumbers of the waves which are trapped in the lower layer. (The cosine in (22) becomes either 0 or ±1 which is included now in R_j).

$$w'_U(x,z) = \frac{\overline{u}_U}{\sqrt{2\pi}} \int_{-\infty}^{\infty} \frac{dh(x')}{dx'} \sum_{j=1}^{\frac{2Z}{\pi}\sqrt{\ell_L^2-\ell_U^2}} R_j e^{-\sqrt{\ell_L^2-\ell_U^2-\left(\frac{j\pi}{2Z}\right)^2}(z-Z)} e^{i\sqrt{\ell_L^2-\left(\frac{j\pi}{2Z}\right)^2}(x-x')} dx' \quad (24)$$

These evanescent waves have a vertical damping factor of $\kappa = \sqrt{\ell_L^2 - \ell_U^2 - \left(\frac{j\pi}{2Z}\right)^2}$ which determines how fast the vertical velocity amplitude decreases with height. If there are more trapped modes in the lower layer (i.e. $j \geq 2$), this damping factor is different for the individual waves. This causes that the horizontal placement of the overall maximal updrafts and downdrafts are not vertical (Fig. 13). The highest vertical velocity is near to the crest of the strongest wave in lower heights, while they shift to the slowest dampened wave with increasing height.

2.6. History of mountain wave and turbulence forecasting

Since the middle of the 1800s, meteorologists have been searching for solutions to determine the evolution of the atmospheric processes and establishing theories to describe the basic phenomena (*Scorer*, 1949; *Long*, 1953; *Doyle and Durran*, 2002; *Smith*, 2003). The challenge was whether atmospheric processes can be described in the form of mathematical equations and it is possible to generate weather forecasts by solving these equations. The physical-mathematical equations describing the atmospheric processes have been first synthesized by *Richardson* (1922). The solution of these equations, however, has been obtained only 28 years later with the appearance of the first computers. The first numerical forecasts in 1950 were made by The Electronic Numerical Integrator and Computer (ENIAC) (*Goldstine and Goldstine*, 1946; *Charney et al.*, 1950; *Charney*, 1951). Since then, more and more efficient computers have been used to solve more complicated versions of the governing equations (*Lynch*, 2006; *Lynch*, 2008). Internal gravity waves were first investigated by Lord Rayleigh and Lord Kelvin in 1883 and 1886.

The first observations of the occurrence of the standing wave at the orographic obstacles' lee-side came probably from observations of a balloon launched in 1928 to the lee of the Rossitten Dunes (today Rybachiy, Curonian Spit, Kaliningrad region, Russia). The observation campaign was organized by the German Glider Flight Institute after *Koschmieder* (1925) foresaw the existence of waves in the atmosphere after the results of Rayleigh and

Kelvin (*Bannon*, 1952; Alaka, 1960; *Maruhashi*, 2019). The first successful observations in 1933 brought also the discovery of rotors (*Hirth*, 1935). Their correct interpretation by *Küttner* (1938), led to the first comprehensive theoretical studies by *Lyra* (1943) and *Queney* (1946) at constant wind and stability, and *Scorer* (1949) and *Long* (1953) at variable wind and stability. Later, further observational data have been collected and supplemented by some important theoretical researches and experiments with numerical models (*Alaka*, 1958), whilst *Küttner and Jenkins* (1953) gave also a comprehensive explanation on the many aircraft accidents at the mountainous area which characterized those years.

In the following decades, numerical modeling became more popular in this field. While mountain waves have several accompanying phenomena, these are mainly caused by the nonlinear nature of the atmospheric processes and theoretical investigations cannot give satisfactory explanation of them.

Mountain wave studies received high attention in the past 30 years and numerous studies have been focusing on mountain waves and its parameterization as a consequence of a growing awareness of their omnipresence, their role in the atmospheric dynamics, and their applied technological advances (*Nappo*, 2012).

Mountain waves are often explored in connection with orographic precipitations (*Barstad et al.*, 2007) and, within the planetary boundary layer, in connection with variations of the terrain structure, flow separation, rotor formation and downslope windstorms (*Durran*, 1990; *Doyle and Durran*, 2002; *Sun et al.*, 2011; *Grubišic et al.*, 2015; *Strauss et al.*, 2015). The ability of MTW to generate aircraft turbulence in the mid- and upper troposphere was also studied (*Lilly*, 1968; *Staquet and Sommeria*, 2002; *Sharman et al.*, 2006). Orographic gravity waves penetrating the stratosphere has been also studied (*Shutts*, 1992; *Smith et al.*, 2008) and even on the general circulation as major wave breaking area are found to be effective sinks of momentum (*McFarlane*, 1987; *Bacmeister et al.*, 1994). Mountain wave activity occurs in the mesosphere and even lower thermosphere, where it causes horizontal wind variations and atmospheric dynamic changes and chemical composition (mixing and redistributing of chemicals such as ozone and oxygen) (*Garcia and Solomon*, 1985; *Miyoshi and Fujiwara*, 2008; *Smith and Skyllingstad*, 2009).

The World Area Forecast Centers (WAFC) has an algorithm to forecast MTW turbulence based on parameterizing wave stress when it exceeds a threshold (*Turner*, 1999). This is not correct, as it is the stress divergence rather than the stress itself associated with the wave dissipation. Comparing this with other methods involving mountain wave, wind shear, and

convective turbulence revealed that the methods on themselves are very limited and it is better to use some combinations of them (*Gill and Stirling*, 2013).

Most recent of these investigations was the Terrain-Induced Rotor Experiment (T-REX) (*Grubišic and Küttner*, 2006), organized in 2006 in the southern Sierra Nevada and Owens Valley, California. T-REX resulted in a better understanding of the interaction between MTW, the atmospheric boundary layer, and the rotors. These experiments were seeking for new observational insights into the small-scale turbulent structure of MTW and improvements in their high-resolution numerical modeling and forecasting. A detailed description of flow structures resulted from the ground-based measurements leading to further comprehensive studies of elevated turbulent zones in the lee of complex terrain, characterization of turbulence, and the tight coupling between the terrain-induced waves and boundary layer dynamics (*Grubišic et al.*, 2008). A vast set of meteorological instruments was deployed in the field, including ground-based scanning LIDARs, research aircraft equipped with modern instrumentation, and radars that can support mountain wave research. Significant progress has been achieved in the understanding of this field and conceptual models of the coupled mountain-wave and low-level turbulence flow in the lee of an isolated mountain range were established. However, they largely lack detailed information on the temporal evolution of waves and they do not account for the possible influence of the downstream atmospheric environment.

Mountain weather forecasting has improved significantly over the past decades. However, it remains challenging in operational forecasting due to the complexity of physical processes, the difficulties of analytically describing the associated phenomena with the MTW, and the spatial and temporal scales needed to be represented in operational NWP models (*Gill and Stirling*, 2013). Operationally used, general-purpose NWP models cannot be run at the ultrafine-scale space-time resolutions necessary to explicitly resolve both the full spectrum of gravity waves and the even smaller turbulent layers that form within breaking waves (*Kim et al.*, 2003).

2.7. The AROME model

In 1991, a European cooperation was created in the field of NWP, the so-called ALADIN (Aire Limitée Adaptation dynamic Développement InterNational) project. NWP models developed under this project were actively operational from 1996 in many European and African countries.

The AROME model has been operational since 2008 and gradually replaces ALADIN since 2012. Indeed, the physical parametrizations of the model are mainly inherited from the non-hydrostatic mesoscale atmospheric model (Meso-NH) research model (*Lafore et al.*, 1998) while the dynamic part is an adaptation for the fine-scale of the dynamic core of ALADIN.

The forecast methodology is primarily based on hydrodynamics (or atmospheric dynamics), thermodynamics, radiation theory, and cloud-physics (approximate numerical solution of the Navier-Stokes equation is computed considering thermodynamic processes and phase changes of water in the atmosphere).

NWP models are essentially the only available tools that provide mountain wave forecasting guidance. At the HMS, medium-range general weather forecasts are mainly based on AROME. ALADIN, GFS (NCEP, USA), and ICON (DWD) are also in operational use. Short-range forecasts with the finer spatial resolution are based on locally executed and developed regional models at HMS (ALADIN, AROME, and WRF) (*Horányi et al.*, 2006). The assimilation of high-resolution local observations (there are already different assimilation techniques) is essential to optimize the performance of turbulence parametrizations (*Montmerle et al.*, 2018).

AROME is a regional NWP models, that provides the expected values of meteorological parameters in the future on a 3D grid (*Arakawa*, 2004). The application enables us to emphasize the short-range prediction of mesoscale meteorological processes.

Some characteristics of the AROME model:

- AROME is a spectral model using a semi-implicit, semi-Lagrange time discretization scheme.
- The AROME model is run with non-hydrostatic dynamics. at its resolution (2.5 km), it can resolve long gravity waves with a wavelength greater than approximately 10 km.
- Physical parametrizations: processes with a characteristic size below the grid resolution or highly complexity processes are considered through parametrizations. The AROME physical parametrizations were adapted from a high-resolution mesoscale non-hydrostatic French research model (Meso-NH) which enables to resolve deep convection explicitly (still parametrizing shallow convection).
- Data assimilation and initialization (determining initial conditions): initial conditions for model forecasts are provided by a statistically optimal blend of meteor-

ological observations and earlier model forecasts (optimal interpolation, variational assimilation). The AROME model uses interpolated ALADIN initial conditions. A local data assimilation system for the AROME model is under development, which will consider observations in higher resolution, however, and compared to the ALADIN model. AROME may resolve gravity waves more precisely (Table 2).

Table 2. Main characteristics of the AROME model.

Main characteristics of the AROME model	
Geographical domain	Carpathian basin
Horizontal resolution	$0.025° \approx 2.5\ km$
Number of vertical layers	Operational model: 60 Case studies: 73
Dynamics and parameterizations	Non-hydrostatic model, deep convection explicitly resolved, shallow convection parameterized
Initial conditions	Local data assimilation: 3d-var and interpolation of surface fields from ALADIN
Lateral boundary condition	ECMWF model
Model time step	60 s
Coupling update	3 h
Number of grid points	401x185
Forecast range	48 h
Runs per day	8

3. Methods

3.1. Mountain wave forecasting

In the past, an MTW forecast product was daily issued by the Unit of Aviation Meteorology at the HMS. It was written by the forecaster in duty in early morning. It contained a 36-hour forecast, and a 5-days outlook (Fig. 14). Relevant data were presented in tabular form for 4 cities (Budapest, Pécs, Szombathely and Miskolc) for 09 UTC, 15 UTC, and next day 09 UTC. This product was published until 11th March 2010.

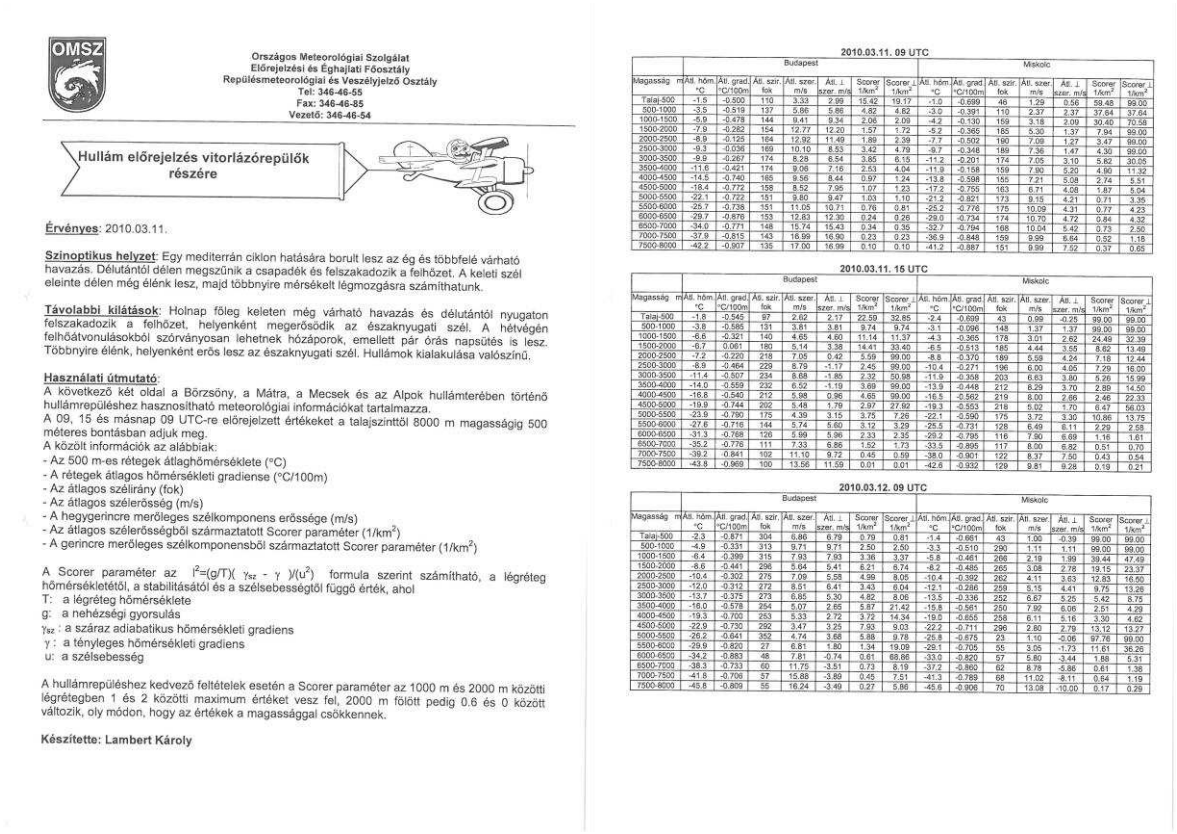

OMSZ

Országos Meteorológiai Szolgálat
Előrejelzési és Éghajlati Főosztály
Repülésmeteorológiai és Veszélyjelző Osztály
Tel: 346-46-55
Fax: 346-46-85
Vezető: 346-46-54

Hullám előrejelzés vitorlázórepülők részére

Érvényes: 2010.03.11.

Szinoptikus helyzet: Egy mediterrán ciklon hatására borult lesz az ég és többfelé várható havazás. Délutántól délen megszűnik a csapadék és felszakadozik a felhőzet. A keleti szél eleinte délen még élénk lesz, majd többnyire mérsékelt légmozgásra számíthatunk.

Távolabbi kilátások: Holnap főleg keleten még várható havazás és délutántól nyugaton felszakadozik a felhőzet, helyenként megerősödik az északnyugati szél. A hétvégén felhőátvonulásokból szórványosan lehetnek hózáporok, emellett pár órás napsütés is lesz. Többnyire élénk, helyenként erős lesz az északnyugati szél. Hullámok kialakulása valószínű.

Használati útmutató:
A következő két oldal a Börzsöny, a Mátra, a Mecsek és az Alpok hullámterében történő hullámrepüléshez hasznosítható meteorológiai információkat tartalmazza.
A 09, 15 és másnap 09 UTC-re előrejelzett értékeket a talajszinttől 8000 m magasságig 500 méteres bontásban adjuk meg.
A közölt információk az alábbiak:
- Az 500 m-es rétegek átlaghőmérséklete (°C)
- A rétegek átlagos hőmérsékleti gradiense (°C/100m)
- Az átlagos szélirány (fok)
- Az átlagos szélerősség (m/s)
- A hegygerincre merőleges szélkomponens erőssége (m/s)
- Az átlagos szélerősségből származtatott Scorer paraméter (1/km^2)
- A gerincre merőleges szélkomponensből származtatott Scorer paraméter (1/km^2)

A Scorer paraméter az $l^2=(g/T)(\gamma_{sz}-\gamma)/(u^2)$ formula szerint számítható, a légréteg hőmérsékletétől, a stabilitásától és a szélsebességtől függő érték, ahol
T: a légréteg hőmérséklete
g: a nehézségi gyorsulás
γ_{sz} : a száraz adiabatikus hőmérsékleti gradiens
γ : a tényleges hőmérsékleti gradiens
u: a szélsebesség

A hullámrepüléshez kedvező feltételek esetén a Scorer paraméter az 1000 m és 2000 m közötti légrétegben 1 és 2 közötti maximum értéket vesz fel, 2000 m fölött pedig 0.6 és 0 között változik, oly módon, hogy az értékek a magassággal csökkennek.

Készítette: Lambert Károly

2010.03.11. 09 UTC

Magasság m	Budapest Átl. hőm. °C	Átl. grad. °C/100m	Átl. szír. fok	Átl. szer. m/s	Átl. ⊥ szer. m/s	Scorer 1/km^2	Scorer ⊥ 1/km^2	Miskolc Átl. hőm. °C	Átl. grad. °C/100m	Átl. szír. fok	Átl. szer. m/s	Átl. ⊥ szer. m/s	Scorer 1/km^2	Scorer ⊥ 1/km^2
Talaj-500	-1.5	-0.500	110	3.33	2.99	15.42	19.17	-1.0	-0.699	46	1.29	0.56	59.48	99.00
500-1000	-3.5	-0.519	137	5.86	5.86	4.82	4.82	-3.0	-0.391	110	2.37	2.37	37.64	37.64
1000-1500	-5.6	-0.478	144	9.41	9.34	2.06	2.09	-4.2	-0.130	159	3.16	2.09	30.40	70.58
1500-2000	-7.9	-0.282	154	12.77	12.20	1.57	1.72	-5.2	-0.385	185	5.30	1.37	7.94	99.00
2000-2500	-8.9	-0.125	164	12.92	11.49	1.89	2.39	-7.7	-0.502	190	7.09	1.27	3.47	99.00
2500-3000	-9.3	-0.036	169	10.10	8.53	3.42	4.79	-9.7	-0.348	189	7.36	1.47	4.30	99.00
3000-3500	-9.9	-0.267	174	8.28	6.54	3.85	6.15	-11.2	-0.201	174	7.05	3.10	5.82	30.05
3500-4000	-11.6	-0.421	174	9.06	7.16	2.53	4.04	-11.9	-0.158	159	7.80	5.20	4.90	11.32
4000-4500	-14.5	-0.740	165	9.56	8.44	0.97	1.24	-13.8	-0.598	155	7.21	5.08	2.74	5.51
4500-5000	-18.4	-0.772	158	8.52	7.95	1.07	1.23	-17.2	-0.755	163	6.71	4.08	1.87	5.04
5000-5500	-22.1	-0.722	151	9.80	9.47	1.03	1.10	-21.2	-0.821	173	9.15	4.21	0.71	3.35
5500-6000	-25.7	-0.738	151	11.05	10.71	0.76	0.81	-25.2	-0.776	175	10.09	4.31	0.77	4.23
6000-6500	-29.7	-0.876	153	12.83	12.30	0.24	0.26	-29.0	-0.734	174	10.70	4.72	0.84	4.32
6500-7000	-34.0	-0.771	148	15.74	15.43	0.34	0.35	-32.7	-0.794	168	10.04	5.42	0.73	2.56
7000-7500	-37.9	-0.815	143	16.99	16.90	0.23	0.23	-36.9	-0.848	159	9.99	6.64	0.52	1.18
7500-8000	-42.2	-0.907	135	17.00	16.99	0.10	0.10	-41.2	-0.887	151	9.99	7.52	0.37	0.65

2010.03.11. 15 UTC

Magasság m	Budapest Átl. hőm. °C	Átl. grad. °C/100m	Átl. szír. fok	Átl. szer. m/s	Átl. ⊥ szer. m/s	Scorer 1/km^2	Scorer ⊥ 1/km^2	Miskolc Átl. hőm. °C	Átl. grad. °C/100m	Átl. szír. fok	Átl. szer. m/s	Átl. ⊥ szer. m/s	Scorer 1/km^2	Scorer ⊥ 1/km^2
Talaj-500	-1.8	-0.545	97	2.62	2.17	22.59	32.85	-2.4	-0.699	43	0.99	-0.25	99.00	99.00
500-1000	-3.8	-0.585	131	3.81	3.81	9.74	9.74	-3.1	-0.096	148	1.37	1.37	99.00	99.00
1000-1500	-6.6	-0.321	140	4.65	4.60	11.14	11.37	-4.3	-0.365	178	3.01	2.62	24.49	32.39
1500-2000	-6.7	0.061	180	5.14	3.38	14.41	33.40	-6.5	-0.513	185	4.44	3.55	8.62	13.49
2000-2500	-7.2	-0.220	219	7.05	0.42	5.59	99.00	-8.8	-0.370	189	5.58	4.24	7.18	12.44
2500-3000	-8.9	-0.464	229	8.79	-1.17	2.45	99.00	-10.4	-0.271	196	6.00	4.05	7.29	16.00
3000-3500	-11.4	-0.507	234	8.68	-1.85	2.32	50.98	-11.9	-0.358	203	6.63	3.80	5.26	15.99
3500-4000	-14.0	-0.559	232	8.52	-1.19	3.69	99.00	-13.9	-0.448	212	8.29	3.70	2.89	14.50
4000-4500	-16.8	-0.540	212	5.98	0.96	4.65	99.00	-16.5	-0.562	219	8.00	2.66	2.46	22.33
4500-5000	-19.9	-0.744	202	5.48	1.79	2.97	27.92	-19.3	-0.553	218	5.02	1.70	6.47	56.03
5000-5500	-23.9	-0.790	175	4.39	3.15	3.75	7.26	-22.1	-0.590	175	3.72	3.30	10.86	13.75
5500-6000	-27.6	-0.716	144	5.74	5.60	3.12	3.29	-25.5	-0.731	128	6.49	6.11	2.29	2.58
6000-6500	-31.3	-0.768	126	5.99	5.96	2.33	2.35	-29.2	-0.795	116	7.90	6.69	1.16	1.61
6500-7000	-35.2	-0.776	111	7.33	6.86	1.52	1.73	-33.5	-0.895	117	8.00	6.82	0.51	0.70
7000-7500	-39.2	-0.841	102	11.10	9.72	0.45	0.59	-38.0	-0.901	122	8.37	7.50	0.43	0.54
7500-8000	-43.8	-0.969	100	13.56	11.59	0.01	0.01	-42.6	-0.932	129	9.81	9.28	0.19	0.21

2010.03.12. 09 UTC

Magasság m	Budapest Átl. hőm. °C	Átl. grad. °C/100m	Átl. szír. fok	Átl. szer. m/s	Átl. ⊥ szer. m/s	Scorer 1/km^2	Scorer ⊥ 1/km^2	Miskolc Átl. hőm. °C	Átl. grad. °C/100m	Átl. szír. fok	Átl. szer. m/s	Átl. ⊥ szer. m/s	Scorer 1/km^2	Scorer ⊥ 1/km^2
Talaj-500	-2.3	-0.871	304	6.86	6.79	0.79	0.81	-1.4	-0.661	43	1.00	-0.39	99.00	99.00
500-1000	-4.9	-0.331	313	9.71	9.71	2.50	2.50	-3.3	-0.510	290	1.11	1.11	99.00	99.00
1000-1500	-6.4	-0.399	315	7.93	7.93	3.36	3.37	-5.8	-0.461	266	2.19	1.99	39.44	47.49
1500-2000	-8.6	-0.441	296	5.64	5.41	8.21	8.74	-8.2	-0.485	260	3.08	2.76	19.15	23.37
2000-2500	-10.4	-0.302	275	7.09	5.58	4.99	8.05	-10.4	-0.392	262	4.11	3.63	12.83	16.56
2500-3000	-12.0	-0.312	272	8.51	6.41	3.43	6.04	-12.1	-0.286	259	5.15	4.41	9.75	13.26
3000-3500	-13.7	-0.375	273	6.85	5.30	4.82	8.06	-13.5	-0.336	252	6.67	5.25	5.42	8.75
3500-4000	-16.0	-0.578	254	5.07	2.65	5.87	21.42	-15.8	-0.561	250	7.90	6.06	2.51	4.29
4000-4500	-19.3	-0.700	253	5.33	2.72	3.72	14.34	-19.0	-0.655	258	6.11	5.16	3.30	4.62
4500-5000	-22.9	-0.730	292	3.47	3.25	7.93	9.03	-22.2	-0.711	296	2.80	2.79	13.12	13.27
5000-5500	-26.2	-0.641	352	4.74	3.68	5.88	9.78	-25.8	-0.675	23	1.10	-0.06	97.76	99.00
5500-6000	-29.9	-0.820	27	6.81	1.80	1.34	19.09	-29.1	-0.705	55	3.05	-1.73	11.61	36.26
6000-6500	-34.2	-0.883	48	7.81	-0.74	0.61	68.86	-33.0	-0.820	57	5.80	-3.44	1.88	5.31
6500-7000	-38.3	-0.733	60	11.75	-3.51	0.73	8.19	-37.2	-0.860	62	8.78	-5.86	0.61	1.36
7000-7500	-41.8	-0.706	57	15.88	-3.89	0.45	7.51	-41.3	-0.789	68	11.92	-8.11	0.64	1.19
7500-8000	-45.8	-0.809	55	16.24	-3.49	0.27	5.86	-45.6	-0.906	70	13.08	-10.00	0.17	0.29

Fig. 14. Past mountain wave forecast product, published until 11th March 2010.

After 6.5 years of hiatus, http://aviation.met.hu, the new website of the Unit started on 7th November 2016. Among others, model forecast outputs are published for several branches of sport aviation on this site. For mountain wave gliding, a wind time-height section is published for 4 airfields (Dunakeszi – Fig. 15, Kőszeg, Pécs-Pogány and Gyöngyös-Pipshegy).

According to experiences of glider pilots, as a rule of thumb, conditions considered favorable for wave generation are steady wind conditions with minimal directional shear and increasing speed with height.

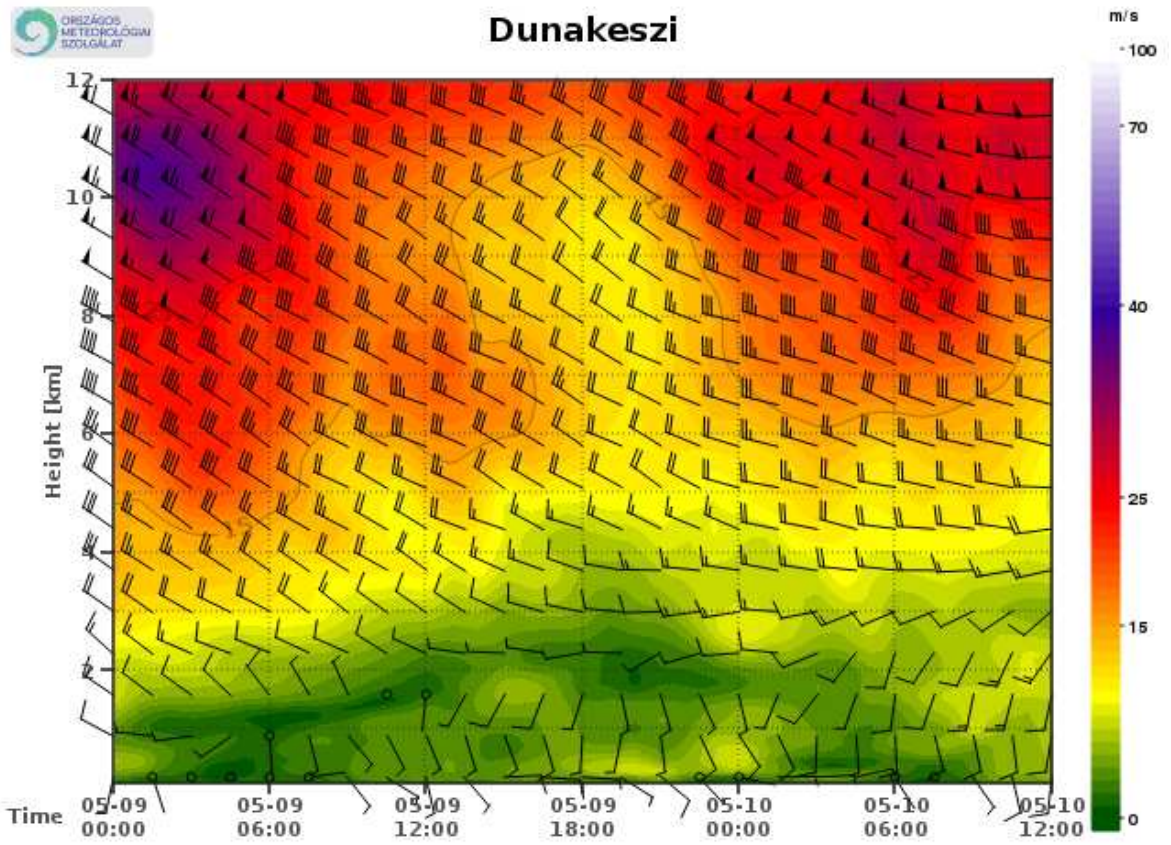

Fig. 15. Wind time-height section published on the aviation.met.hu website.

3.2. Numerical simulations, case study

The AROME model was used to generate model forecast data for the case studies. The vertical resolution of the operational model is 50 hPa over 500 hPa. For the case studies, the vertical resolution was set to 10 hPa between 500 hPa and 300 hPa. Dávid Lancz formulated, and László Kullmann implemented, a discrete version of equation (4b) in the AROME post-processing module, using a central finite difference scheme to calculate derivatives of the model variables.

With these settings, a 36-hour model forecast was initialized with data at 00 UTC 22nd February, 2019. Model forecast products were generated using the HAWK-3 visualization system. These products are the same as presented in *Salavec* (2018) and qualitative analysis of the situation will be provided, focusing on MTW formation.

3.3. Sensitivity analysis

Several other case studies are planned. In the autumn of 2018, a model cycle update was made on AROME. Cases older than the model update cannot be simulated with the current

surface datasets (the current model cannot read the older surface file formats), but newer cases can be simulated with both surface data (the currently operational one and the older one interpolated to the current grid). As the operational model is planned to use for regular production of the products, this raises the question whether or not the cases before and after the model cycle update are comparable. For this to analyze, two model runs were performed with the two surface datasets for a given case.

Effect of surface variable differences on the atmospheric variables are analyzed. Gridpoint-wise comparison of the datasets is carried out by linear regression and relative difference statistics. Statistical analysis was carried out separately for every time step and every vertical model level for Brunt-Väisälä frequency, wind shear curvature $\frac{\partial^2 u}{\partial z^2}$, vertical gradient of virtual temperature, geopotential, model vertical velocity w, relative humidity, Scorer-parameter ℓ^2, temperature, potential temperature, equipotential temperature, turbulence kinetic energy and magnitude of horizontal wind $\sqrt{u^2 + v^2}$ where u and v are the model horizontal wind components.

A linear function $y = mx + b$ was fit against the data points where x contains values from the model run using the current terrain dataset and y contains those using the interpolated older terrain dataset. Here, m is the slope and b is the intercept of the line estimated by fitting using Marquardt-Levenberg nonlinear least squares algorithm (*Levenberg*, 1944; *Marquardt*, 1963). In an ideal case, $m = 1$ and $b = 0$ is expected (with zero asymptotic errors) which would mean there are no difference between the two model datasets, i.e. they are identical. Values of $m \approx 1$ and $b \approx 0$ with non-zero errors, which are so large that $m = 1$ and $b = 0$ fall within the error ranges, mean the differences between the two model datasets are random. In this case, the magnitude (or significance) of this random error can be estimated from pointwise difference statistics of the model data.

If $m \approx 1$ and $b \approx 0$ but $m = 1$ and $b = 0$ fall outside the error ranges, that means the difference is statistically significant, no matter how little it is by absolute magnitude. In this case, we might formulate absolute difference thresholds as acceptable differences and treat the two model datasets similar if the pointwise differences are less than these thresholds, and then derive similar conclusions while studying the appearance of atmospheric phenomena in the model. In this case, the structure of the $m(t, z)$ and $b(t, z)$ data can be examined and correct interpretation of their features might help understanding how the model's operational features (e.g. model spin-up, surface-atmosphere interactions, chaotic error propagation etc.) interact with the differences in the two terrain datasets.

3.4. Automatic wave trapping identification

Provided that Scorer-parameter vertical profiles can be extracted at any time and grid point, it is possible to implement a wave trapping identification algorithm. The general method is to choose a custom height, approximate the Scorer-profile with an appropriate two-layer idealized profile and calculate the number j of possible trapped wave modes using equation (22). Gnuplot v5.2 was used for generating vertical profile plots of model Scorer-parameter, the approximating Scorer-parameter values and the j number.

For this, we interpolate the model Scorer-parameter data to a 10 m vertical resolution from the surface or the lowest model level to the tropopause (which is considered being at the height where temperature has a minimum). Choosing every height as the layer boundary Z, in order to split the atmosphere into two layers, we can choose appropriate constant Scorer-parameter values to approximate the lower and the higher layer values.

This approximation can be done in several ways. Averaging Scorer-parameter values in both layers can give unrealistic results because of high distortion caused by the high near-surface Scorer-parameter values, especially in the night. Thus, we decided to choose the lower quartile of the Scorer-parameter values in the lower layer, and the upper quartile in the upper layer. They converge close to each other in the higher troposphere if the layer of high Scorer-values is thin enough, avoiding unrealistically high j values caused by the higher difference between the two Scorer-parameter values.

A linear interpolation is carried out in the script by the following function:

```
interp(x0,y0,x1,y1,x)=y0+(y1-y0)/(x1-x0)*(x-x0)
```

Here, (`x0,y0`) and (`x1,y1`) are two known points and the function returns with y at x. When interpolating Scorer-parameter, `x0` and `x1` will get the height, and `y0` and `y1` the Scorer-parameter from the two model levels surrounding the level at height x to be interpolated.

Heights are measured in meters above ground level. Surface geopotential (a constant field) is provided in the model data and geopotential values are calculated for the pressure levels so we calculated model level heights as their difference divided by gravity.

Temperature has a minimum at a certain height which is considered the tropopause (in a few cases, this minimum is at the topmost model level, i.e. at 100 hPa). We set that height as our maximum height `maxH`, while `minH` will be either zero or the height of the lowest model level (which is at 1000 hPa) if it is over the ground. Height range is then restricted to `[minH:maxH]` and the model levels outside this range will be omitted from calculations.

The input data for the linear interpolation is obtained abusing the syntax of the `plot` command whose `using` specifier contains the necessary variable assignments (and the plot output itself, which contain plots of 0 against 0, is redirected to the Unix null device `/dev/null` which gobbles all output). The `every` clause of the command selects the two levels (the $(j-1)^{th}$ and the j^{th}) surrounding the actual `z` height which loops in the range `[minH:maxH]` by steps of 10 m. Interpolated values, then, are written to the datablock `$linear`.

```
set print $linear
set table '/dev/null'
do for [z=minH:maxH:10] {
  if(z>c){j++}
  plot fs using (a=($10-$11)/g,0):(b=$1,0) every ::j-1::j-1 with table
  plot fs using (c=($10-$11)/g,0):(d=$1,0) every ::j::j with table
  print z,interp(a,b,c,d,z) }
unset table
```

This method is rather slow, interpolation using external tools (even within the gnuplot script using the `system()` call) is advisable instead.

Now we can approximate a 2-layer atmosphere. `Z` goes in the range `[minH:maxH]` through the previously set `z` values (i.e. with 10 m steps now, however, this might be further rarified if runtime issues arise) and serves as the height of the layer boundary. Extreme heights are omitted, however, to ensure a layer has at least three values. Data necessary for plotting will be stored in the datablock `$trap`. The approximating Scorer-parameter values are read from the output of two `stats` commands which calculates (among others) the quartile values. Gnuplot orders the Scorer-parameter values in both layers which is a very slow operation. Plotting one profile needs ca. 2.5 seconds on a 1.7 MHz 4-threaded processor PC, so applying this to the whole model data (401x185x37 profiles) would take approximately 80 days. Thus, the method for obtaining upper- and lower-layer Scorer-parameters is under consideration: a value not requiring data ordering would be advisable, and assuming a skew-normal distribution for the Scorer-parameters seems reasonable (*Grushka*, 1972; *Azzalini and Capitanio*, 2013).

```
set print $trap
do for [Z=ceil(minH)+20:floor(maxH)-20:10] {
  stats [][ceil(minH):Z] $linear using 2:1 nooutput
  lL=STATS_lo_quartile_x
  stats [][Z:floor(maxH)] $linear using 2:1 nooutput
  lU=STATS_hi_quartile_x
}
```

4. Results

4.1. Original plans and earlier progress

On 13th October, 2017, the weather in the Carpathian Basin, especially in the northern and eastern parts, was favorable for MTW formations. Fig. 16 shows cloud pattern indicating mountain wave formation over North-East Hungary. We can identify vertically propagating waves over the little Carpathians as only one row of wave cloud is visible there (Fig. 17) and trapped waves over North-East Hungary as multiple wave crests are visible there.

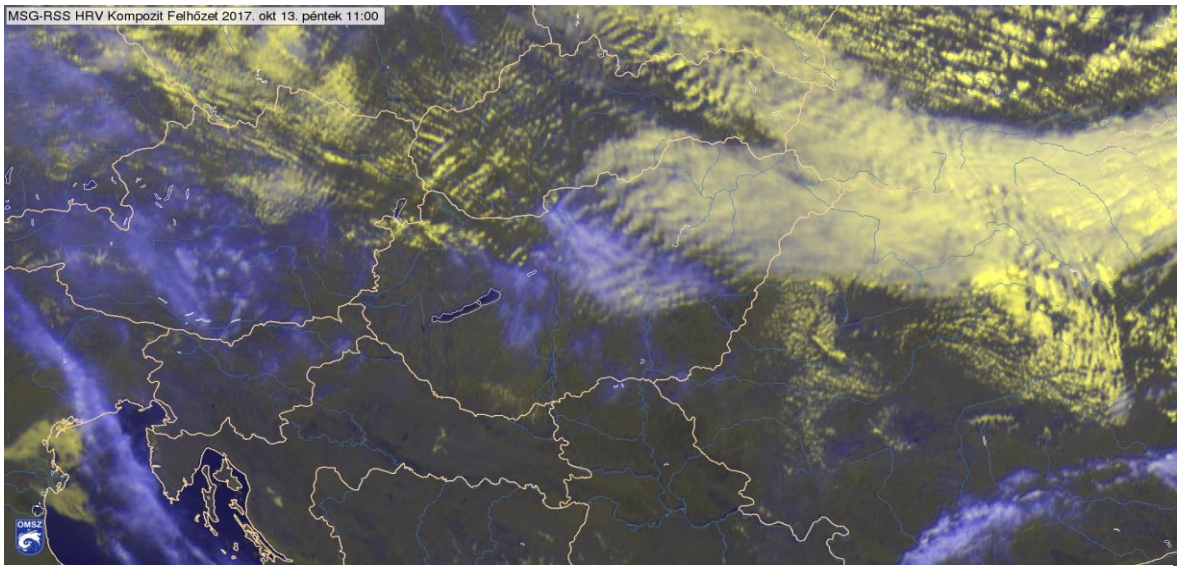

Fig. 16. MSG-RSS HRV composite image at 11:00 UTC on 13th October, 2017

Cool air mass flowed from the northwest with strong northwestern currents. There was also an inversion around 850 hPa, which helped the formation of the waves. In the northeast, more moisture arrived in the middle air layers in the morning. At approximately 4 to 4.5 km height, it was enough to form stationary wave clouds, which was seen in the satellite image, and they were detectable for several hours.

Detailed analysis of this situation was carried out by *Salavec* (2018) using AROME model outputs visualized by the HAWK-3 system. This case and the article served as a basis for further planning in that period.

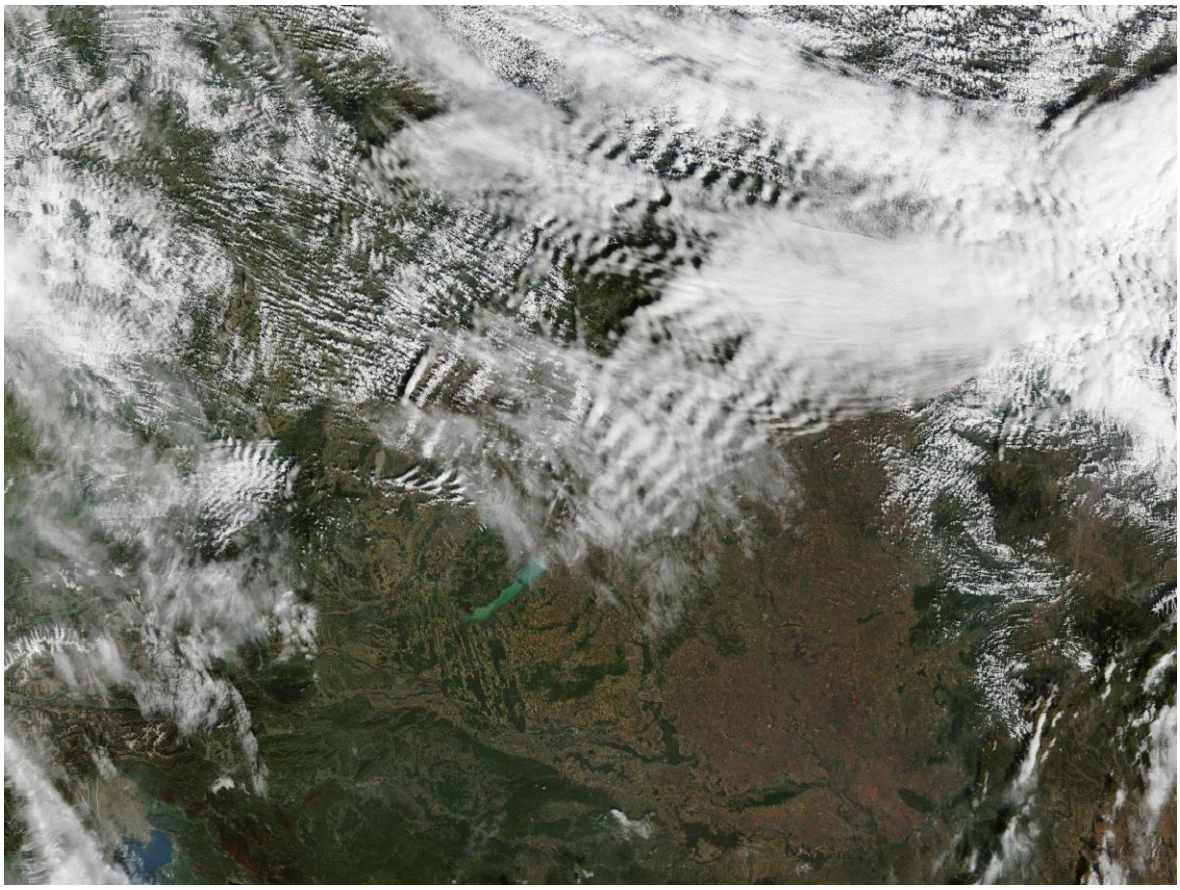

Fig. 17. Terra/MODIS visible image at 9:50 UTC on 13th October 2017.

4.2. Case study: 22-23 February 2019

In this subsection, we reproduce the qualitative analysis for the 22nd to 23rd February, 2019 situation based on *Salavec* (2018). Vertical profiles of equipotential and potential temperature, horizontal and vertical wind, relative humidity, turbulence kinetic energy (TKE), and Scorer wavenumber are produced using the HAWK-3 visualization system.

On 22nd February, 2019, a cold front was passing over Hungary and mountain wave formation was observed on satellite imagery (Fig. 18) on the backside edge of the frontal cloud field. In early morning of 23rd, operative AROME forecast runs were checked whether they predicted the evolution of the mountain waves. This case study reproduces the products found in *Salavec* (2018) at the northern part of the C-D section in Fig. 35. Because of the limited extent of the thesis, we have chosen to show only the spatial cross-sections at 14 UTC

on 22nd at which time the model outputs have some recognizable features about mountain wave formation.

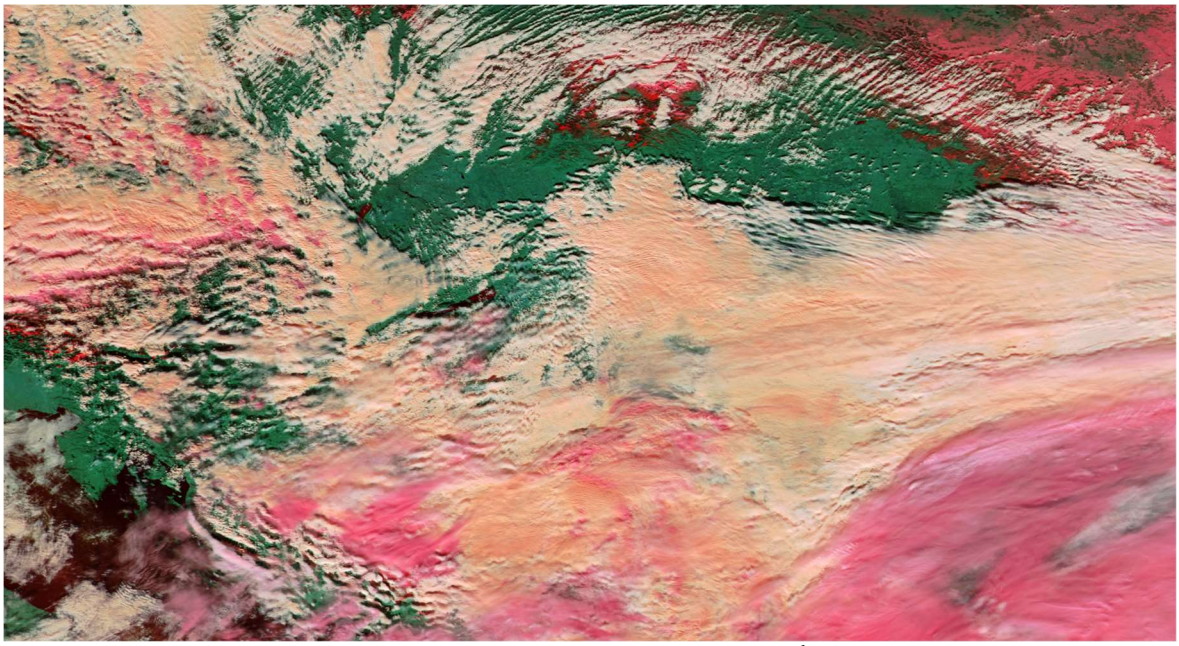

Fig. 18. Suomi NPP/VIIRS false-color image on 22nd February 2019.

4.2.1. Vertical velocity

Fig. 19 shows the vertical velocity with colors, where red colors indicate updrafts and blue colors indicate downdrafts, and the relative humidity with grey lines over 70%. Wave-like motion is indicated by the model output which can be seen over both the Tatra ranges and the Mátra range. The former waves seem to have not perfectly vertical phase lines above 7 km height. This might be the effect of high wind shear near the Polar front jet stream.

Values of the relative humidity higher than about 95% may indicate possible cloud formation but the threshold can be lower when vertical motions are strong enough. And according to these values, we can have an expected view on the thickness of the clouds.

It can be seen by the black patches that the vertical velocities in the model output are much higher at some places than where the scale ends, i.e. values higher than 2 m s^{-1} are present. This is a problem of the design of the product, adjustment (stretching) the color scale needs to be considered. This may cause, however, that weaker MTW formation will become more difficult to identify.

A time-height section of this product might be rather useless as the wave motions cannot be visible on that. However, when mountain wave formation is identifiable on the cross-section, the updraft or downdraft might be present on the time-height section and its disappearance might indicate the dissipation of mountain waves.

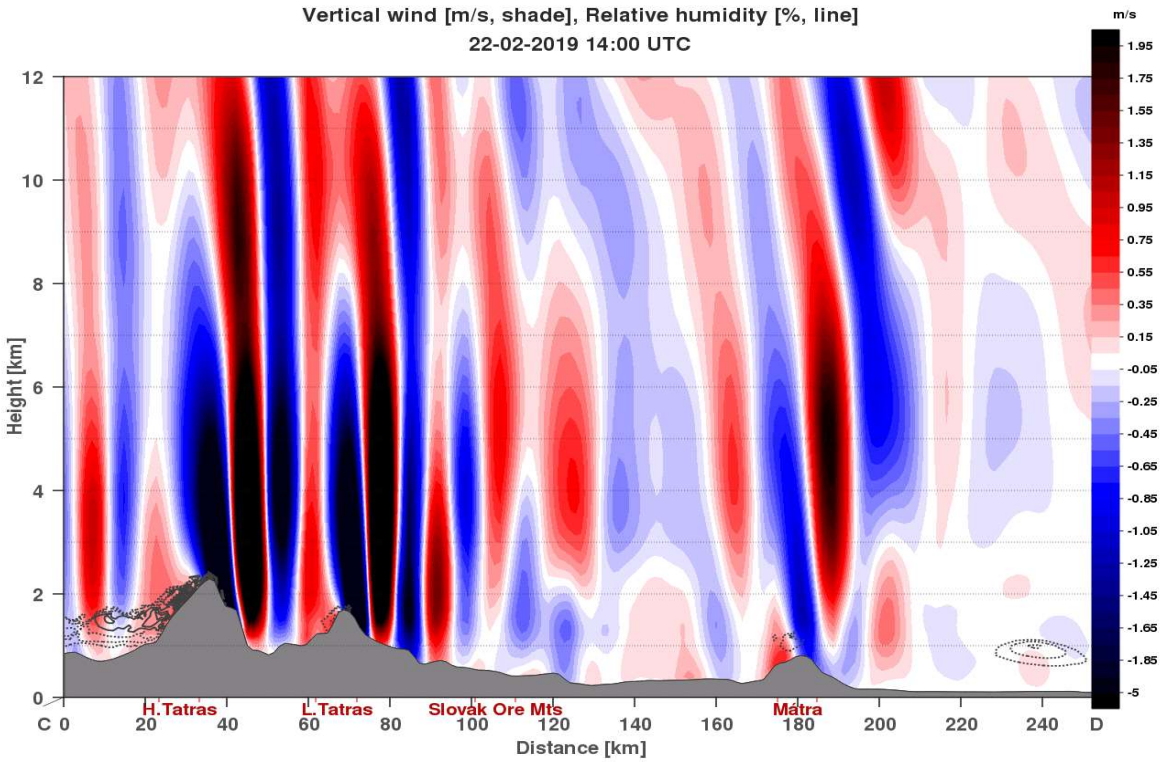

Fig. 19. Vertical velocity (red: updraft, blue: downdraft, m s^{-1}) and relative humidity (above 70%, grey lines) at 14 UTC on 22nd February, 2019, from the AROME model initialized at 00 UTC on 22nd February, 2019.

4.2.2. Relative humidity

While the previous product already contains relative humidity, its purpose is mainly to identify whether or not repeating patterns, whenever visible at high humidity values, are connected to the updrafts (and whether or not lenticular cloud formation is expected). In turn, Fig. 20 shows only the relative humidity in which the general state of the atmospheric moisture can be examined. This can be useful for detecting possible cloud formation in general.

Earlier, a cloud fraction (a 3D field expressed in octas, based on the hydrometeors) was also shown on this product with grey semi-transparent patches. The model doesn't calculate this field by default and it was only an experimental parameter in the earlier case study. This parameter is planned to be implemented, however, the coarse vertical resolution of 50 hPa in the higher troposphere gives a high uncertainty to its correct interpretation.

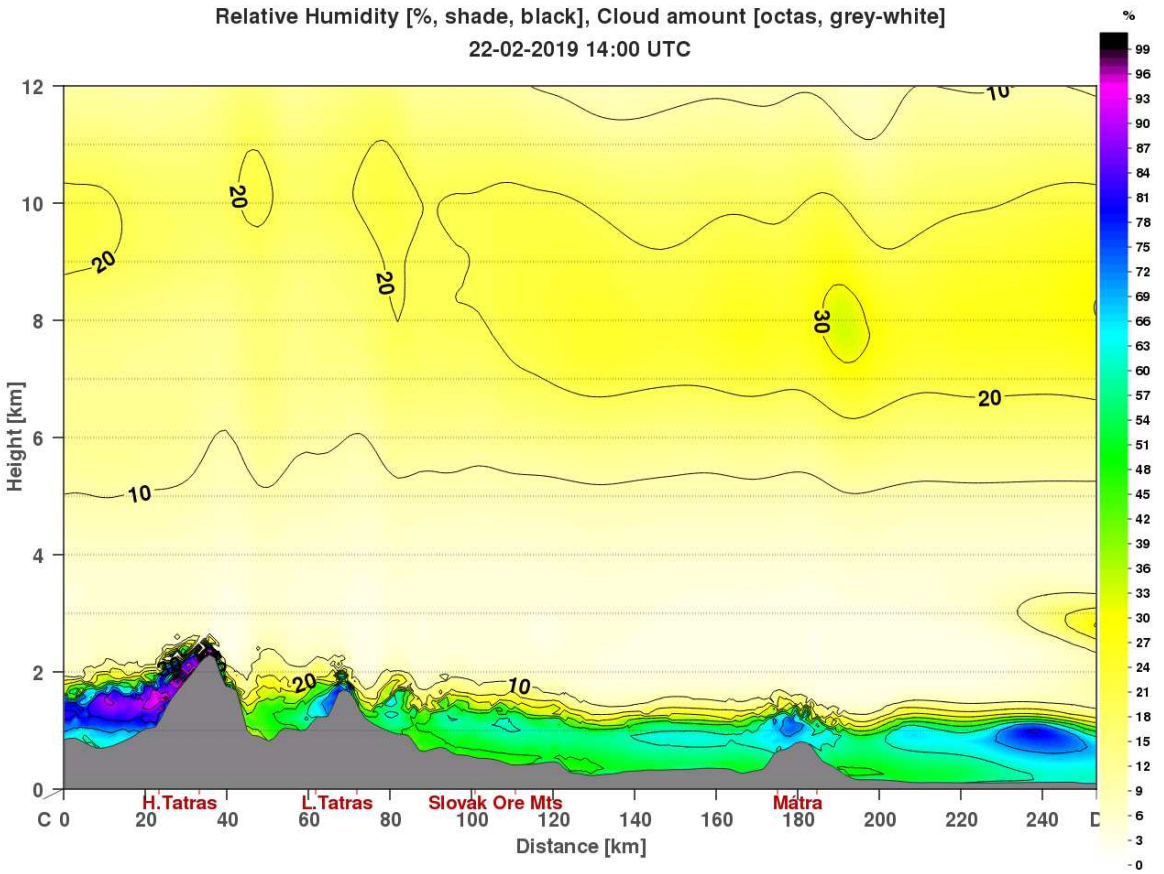

Fig. 20. Relative humidity at 14 UTC on 22nd February, 2019, from the AROME model initialized at 00 UTC on 22nd February, 2019. Colors and black contours indicate relative humidity. Cloud amount (from a 3D variable 'cloud_fraction' based on hydrometeors) was calculated earlier as an experimental variable, and shown with semi-transparent grey shading. This data is currently missing from the current model output but is planned to calculate later.

4.2.3. Horizontal wind profile

Fig. 21 shows the horizontal wind with barbs. Colors represent the magnitude of its component parallel to the cross-section. This means that, for example, a downward pointing wind barb must be interpreted as horizontal wind from North, and not vertical downdraft. Positive values of the parallel wind component appear in warm, reddish colors and they always mean wind from left to right on the section, which is from north to south in this case. We can observe that the wind direction is not changing significantly, and the speed is increasing, with height over Tatras, and this supports MTW formation according to pilots' experience.

Although the wave equation is written for the vertical wind perturbation, there is also a perturbation in the horizontal wind. This is not surprising, according to equation system (7a-d). Another explanation is that the height-dependent average horizontal wind refers to the layer at a given height, but that layer is displaced by the vertical wind. This can also be seen mostly over the Lower Tatras.

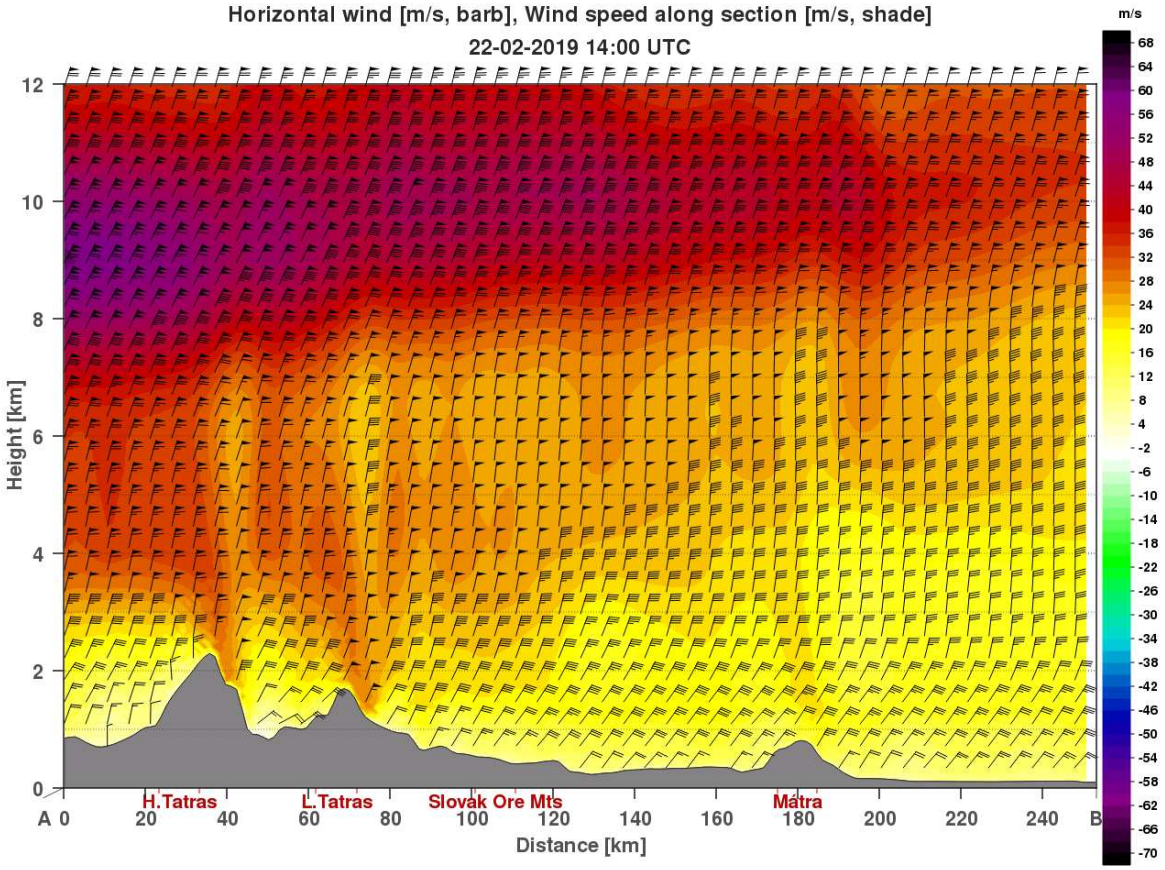

Fig. 21. Horizontal wind (barb) and wind component parallel to the cross-section (color, positive values mean wind from right to left, m s^{-1}) at 14 UTC on 22nd February, 2019, from the AROME model initialized at 00 UTC on 22nd February, 2019.

4.2.4. Potential and equipotential temperature

Both parameters provide information on atmospheric stability: higher density of the isolines means greater stability, and thus a higher Brunt-Väisälä frequency. Where isolines are rare, the atmosphere is less stable. Neutral atmosphere has zero vertical gradient of potential temperature. This is the case usually in the boundary layer in summer daytime where shallow convection is present (Fig. 22).

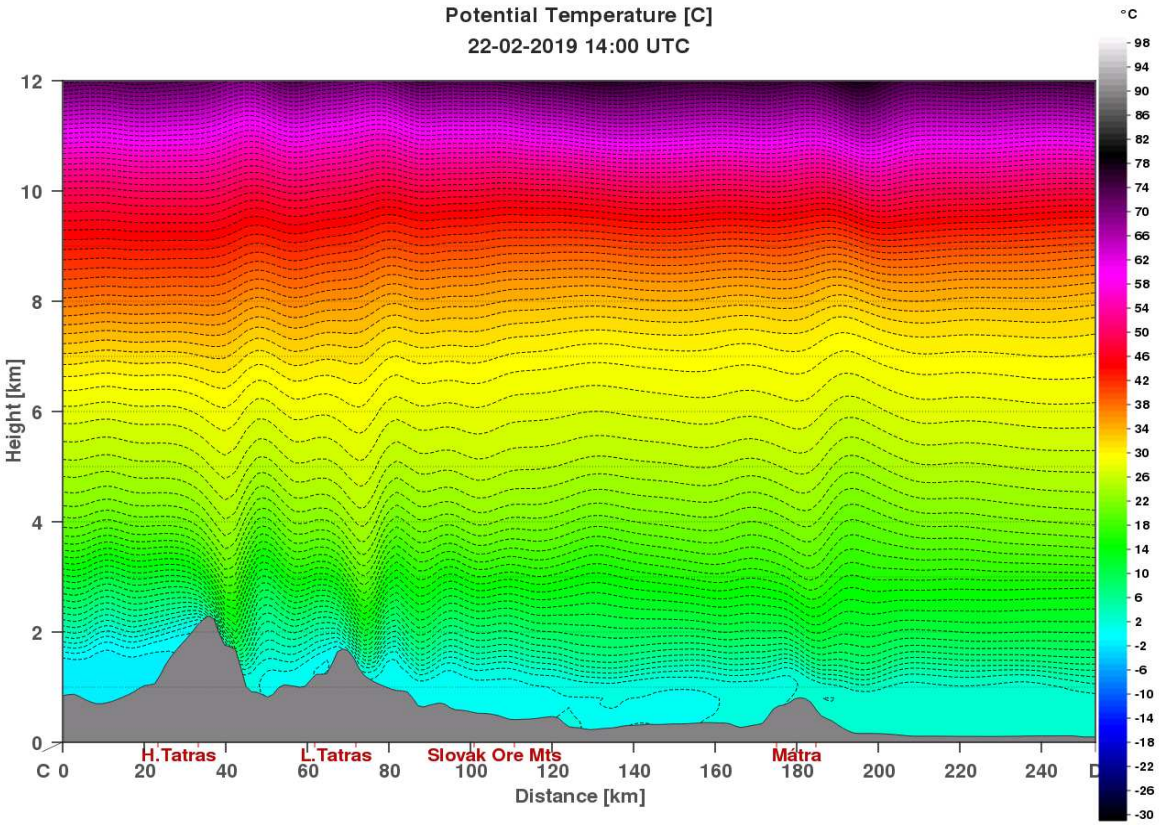

Fig. 22. Potential temperature [°C] at 14 UTC on 22nd February, 2019, from the AROME model initialized at 00 UTC on 22nd February, 2019.

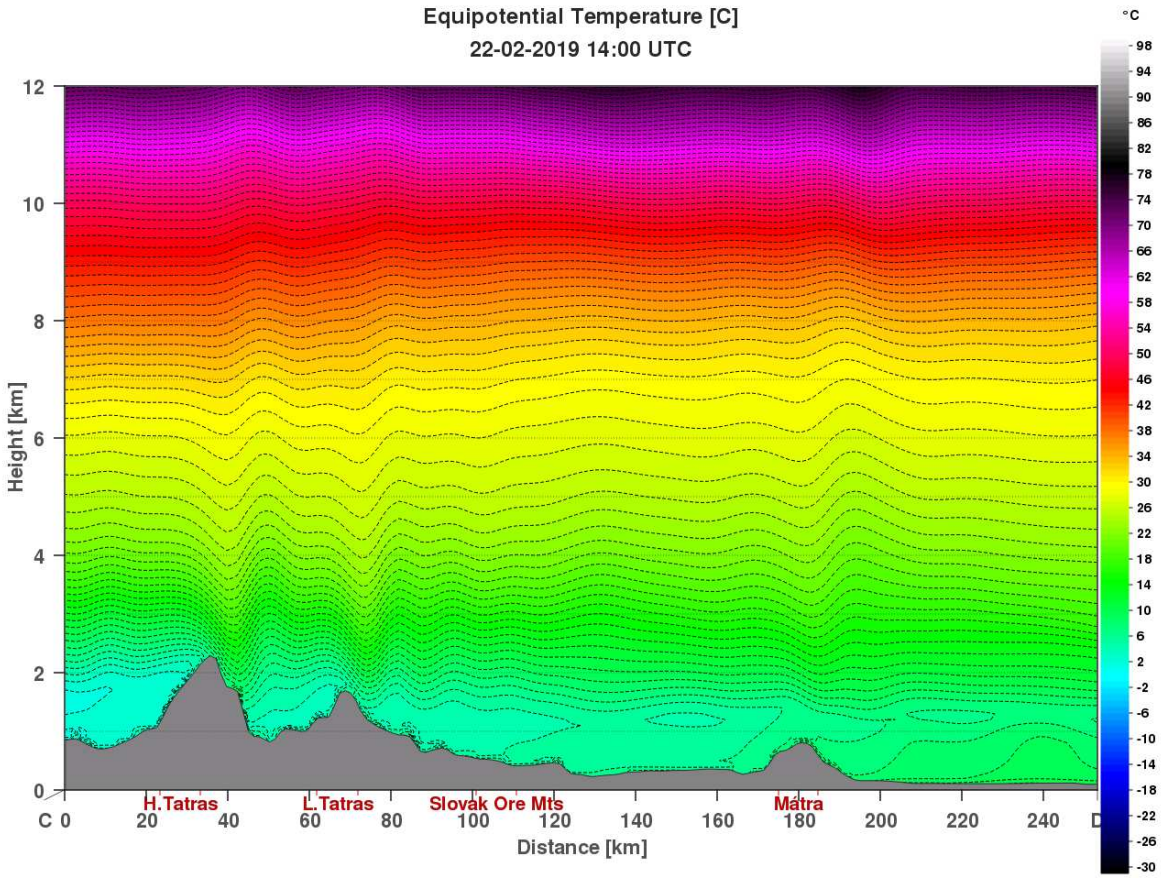

Fig. 23. Equipotential temperature [°C] at 14 UTC on 22nd February, 2019, from the AROME model initialized at 00 UTC on 22nd February, 2019.

The equipotential temperature (Fig. 23) product, in addition, can show what layers may be moist-unstable. As the equivalent temperature involves moisture (mixing ratio), a moist layer can have less gradient in the equipotential temperature compared to that of the potential temperature. If more moisture arrives in a layer, the equipotential temperature of that layer will increase, making its gradient to decrease above. In the case of moist instability, equipotential temperature gradient can be even negative. If some process forces condensation of water vapor in this layer, the cloud formation will be convective, thus, cumulus clouds will form. To form lenticular clouds, absolute stability is needed.

During wave formation, the air parcels move adiabatically, so the air transport causes the isolines to be deformed into a wave-like shape, which is visible in this case on these products.

4.2.5. Scorer-wavenumber

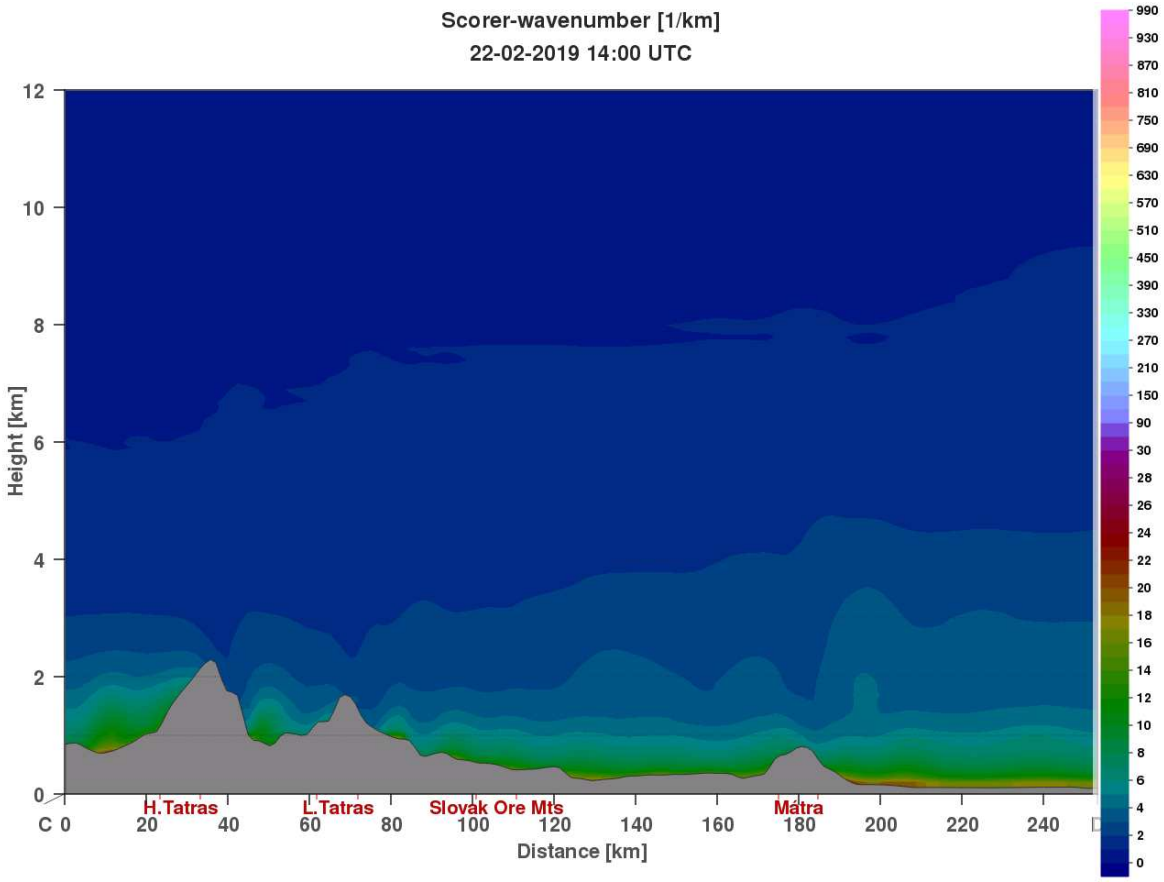

Fig. 24. Scorer-wavenumber [km^{-1}] at 14 UTC on 22nd February, 2019, from the AROME model initialized at 00 UTC on 22nd February, 2019.

Fig. 24 shows the Scorer-wavenumber ℓ (the square-root of the Scorer-parameter). Its scale is more readable than that of the Scorer-parameter itself because smaller differences are more pronounced. However, the parameter itself could can be plotted.

It has a unit of km^{-1}, so if the value is e.g. 4 km^{-1}, that means that mountain waves have 0.25 km overall wavelength.

Any features discussed in the theory of mountain wave formation can be identified. If the Scorer-wavenumber has a sudden decrease in the middle troposphere, wave trapping can occur. On both a cross-section and a time-height, the spatial and temporal extension of the trapped wave modes can be estimated until where and when the difference of the Scorer-wavenumbers remains high.

It can be seen that the Scorer-wavenumber values in the free troposphere are smaller than those in the lower troposphere, which is often ideal for trapping of lee waves. In our case, high values of the Scorer-parameter are present only in the boundary layer, possibly because of the strong decrease of the wind shear which is usual in the boundary layer.

Comparing this with the potential temperature product, it seems like that the Scorer-wavenumbers are high under the cold front. The front's surface is already emerged over the peaks of Mátra mountains, but not over the Higher Tatras. However, the low-level wind was strong enough to flow over the Tatras, elevating locally the front surface over the mountain. A possible downslope windstorm can be identified over both Higher and Lower Tatras. The hydraulic jump-like phenomena then penetrated possibly the stable layer of the front causing wave formation which remained trapped in that layer, as it is slightly visible over the Slovak Ore Mountains. However, over Mátra, the mountain wave seems to be a vertically propagating wave as the air under the front became less stable again and waves in this case are able to "leak" through that layer, as most of the wave modes in themselves are vertically periodic in each layer.

4.2.6. Turbulence kinetic energy

This product is a side-product of the work of André Simon, former colleague at the HMS. He implemented TKE based on a 1,5-order closure model, applying its prognostic equation. It is known that the local increase of wind shear can generate mechanical turbulence which might appear in this product (Fig. 25). Usually, high values are present in the boundary layer as can be seen in this case. In the free troposphere, there is usually no turbulence at all. A few cases, for example deep convection appearing in the model or hydraulic jump-like streaming can cause high wind shears and low Richardson-numbers, and in this case, some turbulence kinetic energy may appear in the model. This product might be useful in identifying secondary turbulent phenomena accompanying mountain waves, however, current evidence suggests that this would need higher model resolution.

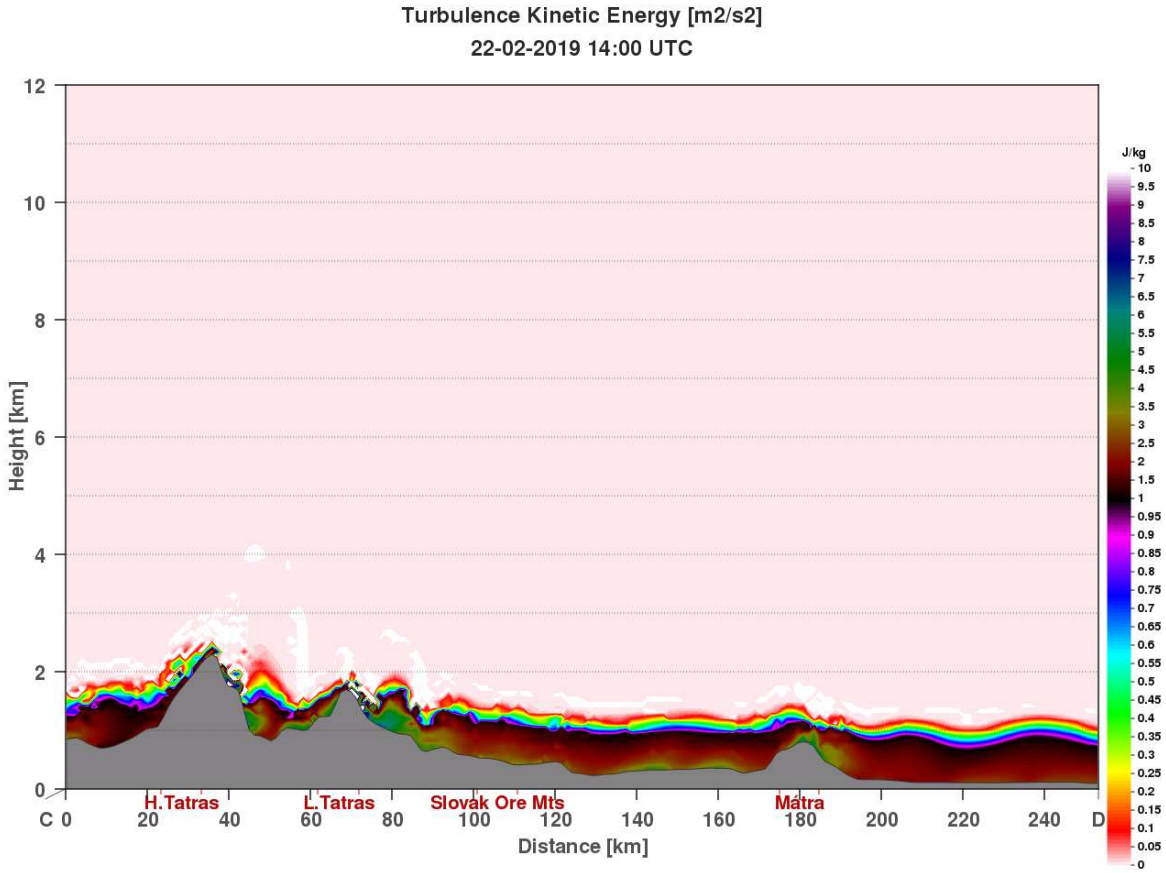

Fig. 25. Turbulence kinetic energy [J kg^{-1}] at 14 UTC on 22nd February, 2019, from the AROME model initialized at 00 UTC on 22nd February, 2019.

4.3. Sensitivity analysis

Fitting linear function against the gridpoint-wise pairs of data was carried out for several variables, as mentioned in subsection 3.3, and for every height and every time step separately, giving estimations of $m(t,z)$ and $b(t,z)$ and their asymptotic standard errors.

During the analysis, some data became corrupted, so analysis of BV-frequency and shear curvature term is left out. In an ideal case, $m = 1$ and $b = 0$ is expected within error range. However, the effect of the different initial surface values might have significant.

Qualitative analysis suggests that the resultant products have a few common features but there are also unique structures recognizable in some cases, and some errors emerged as well obscuring the details in some cases. Plotting of the fitted data was carried out in a way that high deviations from the expected values are visible but fine structure around the expected values is currently less meaningful.

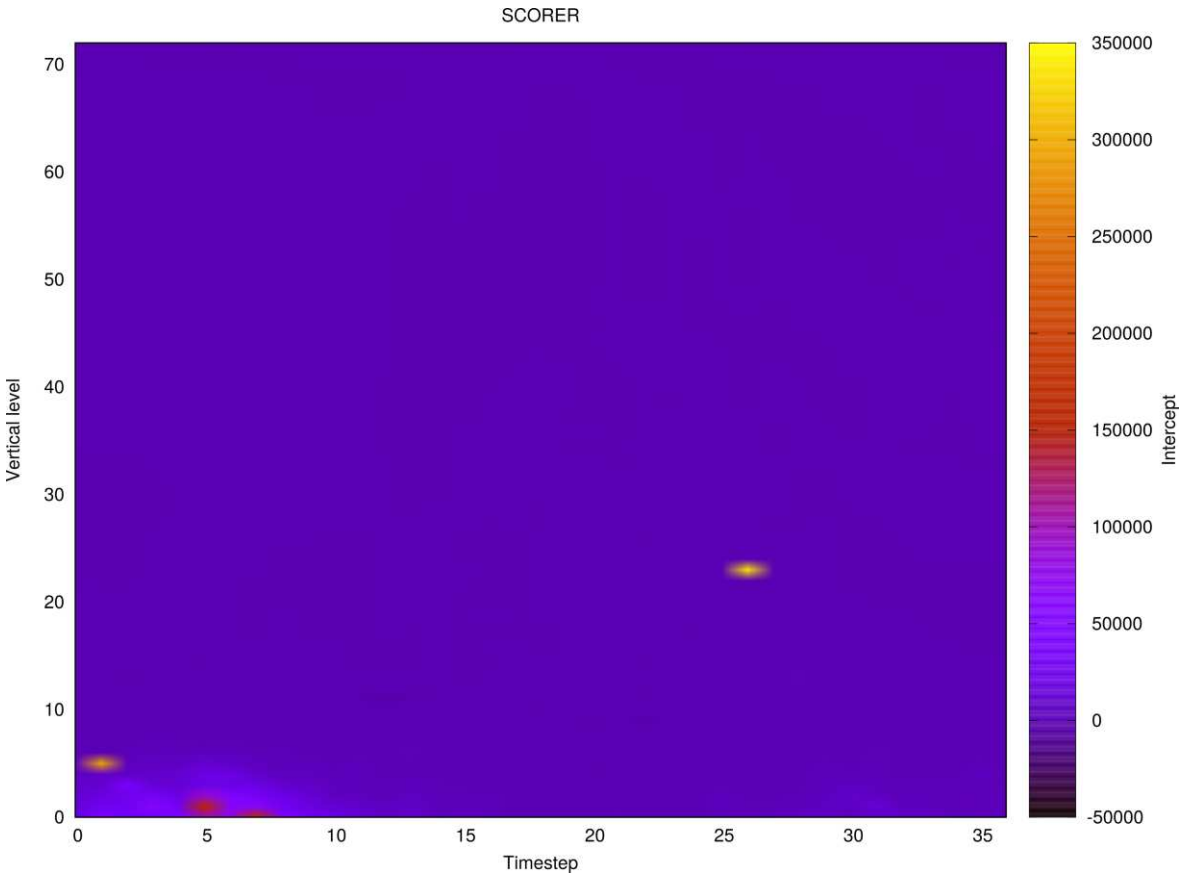

Fig. 26. Intercept of Scorer-parameter $\ell^2[km^{-2}]$. Small patches of very high intercepts made fine structure obscured.

Computational or numeric overflow errors may arise during calculations, but in some cases, this might be caused by the sign of a real phenomenon (Fig. 26). In this case, the real

structure can become completely obscured. The whole analysis, thus, needs a comprehensive review concerning the sources of these errors, and then repeated.

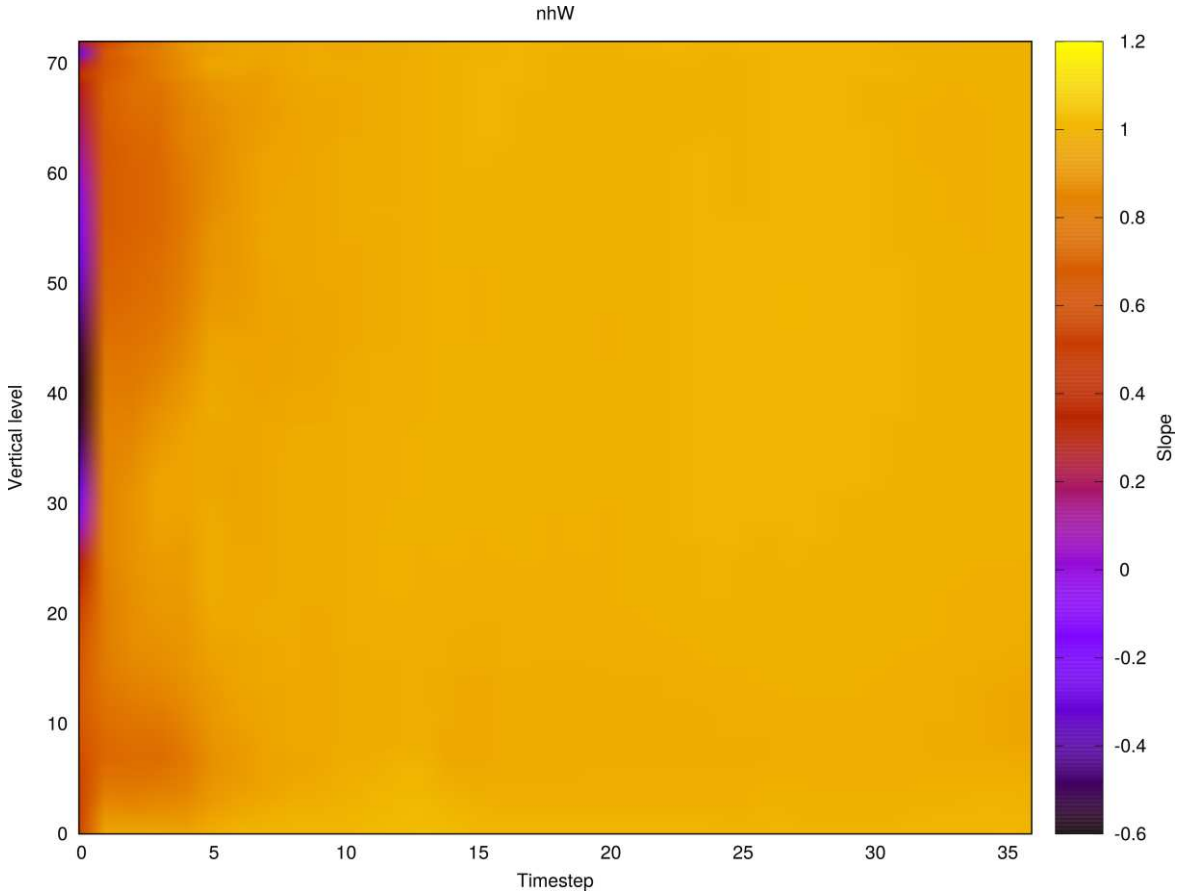

Fig. 27. Vertical velocity, slope parameter. High deviations are visible on the first two time-steps which then fade out quickly.

Most variables share the feature of higher deviations from the expected values in the first few time steps (Fig. 27). This is probably caused by the model spin-up. During when the model is out of statistical equilibrium, a random progress of the differences can cause the initial increase of the differences, which will later consolidate. These errors seem to be height-independent, or the differences in some cases are higher in the higher troposphere, which might be surprising as the surface datasets has their initial differences.

One exception seems to be relative humidity, for which a significant deviation is visible even after time step 15 in the middle and upper troposphere. This might be caused by the dry air behind the cold front as very low humidity values tend to produce higher differences in the slope (Fig. 28).

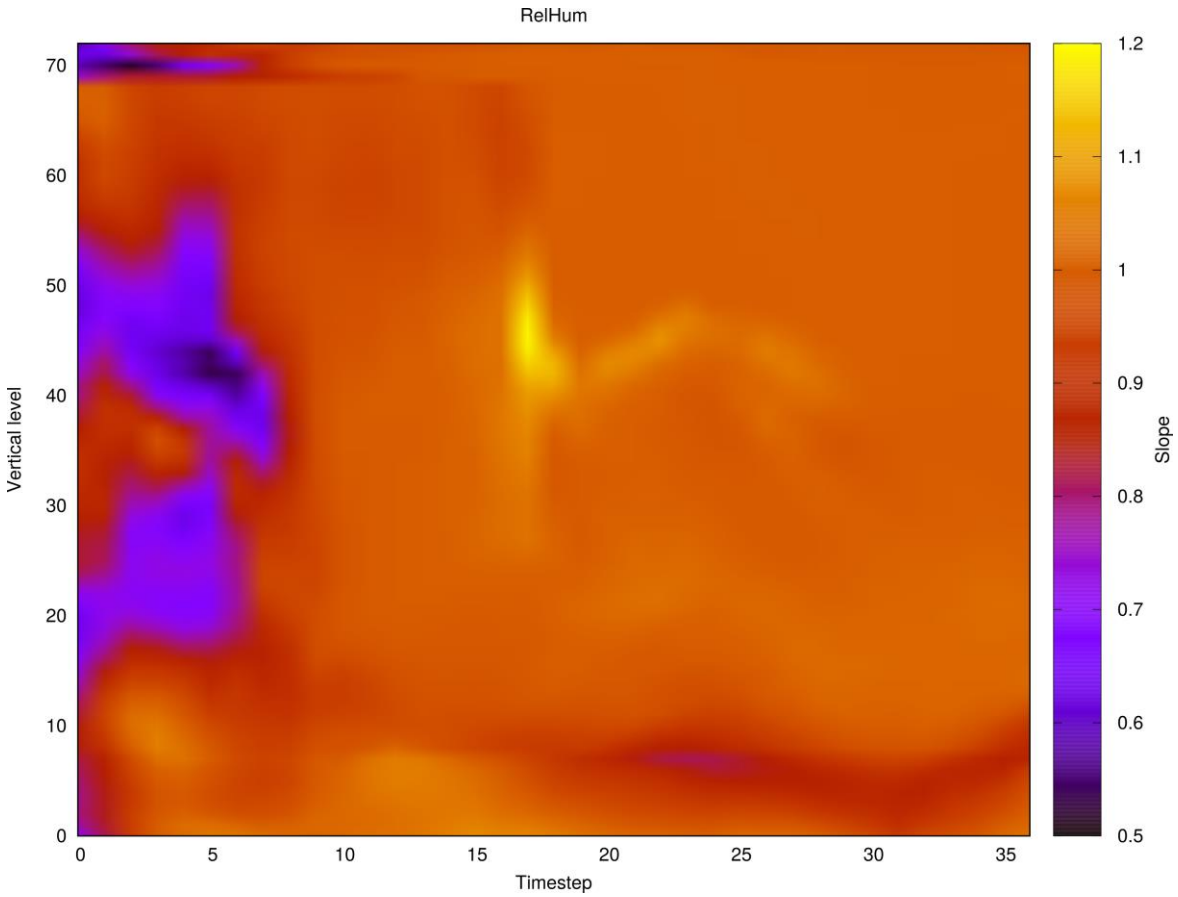

Fig. 28. Relative humidity slope analysis. Values differ from 1 mainly in the model spin-up period, but significant differences are recognizable mainly between time steps 15 to 25 and height level of 35 to 55. The exact reason is unclear but may be weather related.

In general, fitted parameter errors are approximately two orders of magnitude less than the difference of the fitted parameters from their ideal values. This means that, even if the fitted parameters are reasonably close to the ideal values (the two model runs having relative differences of at most a few percent), the deviation from the expected values are still statistically significant. Thus, the difference between the two models might potentially lead to inconsistencies. So, to ensure consistency, reasonable thresholds of differences of gridpoint-wise values should be formulated and model output consistency must be defined based on them, then, model runs must be compared focusing on these consistency definitions. Scorer-parameter and vertical velocity may be important in this concern, as estimated j values are sensitive to Scorer-parameter profile, and vertical velocity can have abrupt changes as j exceeds an integer value. Further detailed analysis of these are needed with highlighting the fine structure of the fitted parameters around their expected values.

4.4. Automatic wave trapping identification

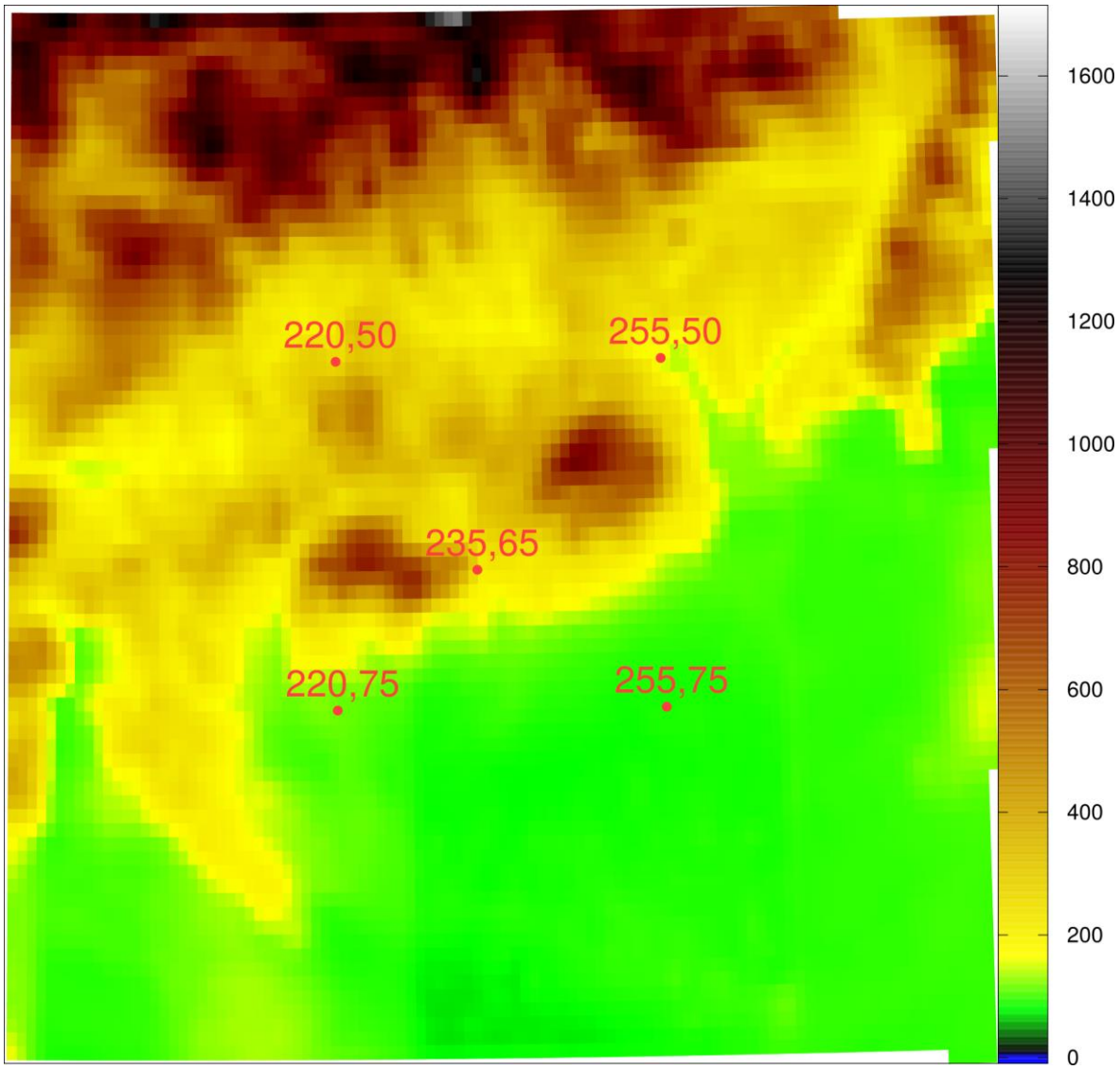

Fig. 29. Topography around the Mátra and Bükk ranges. The 5 points for which the profiles of Scorer-parameters and j values are indicated. Points are near Somoskő (220,50), Kazincbarcika (255,50), Sirok (235,65), Ecséd (220,75) and Mezőkeresztes (255,75)

Vertical profiles of the model Scorer-parameter were extracted at five points near the Mátra and Bükk mountain ranges (Fig. 29). The Scorer-parameter values were interpolated to 10 m vertical resolution and number j of possibly trapped wave modes were calculated using equation (22) for every possible height as the layer boundary height Z, and lower and upper Scorer-parameters as the lower and upper quartile of the values in the layers.

In general, the Scorer-parameter has high values in the boundary layer because a) the wind shear curvature of both the logarithmic and the Ekman wind profile has a high positive value, and b) the low horizontal wind by itself may overcompensate the low BV-frequency in the stability term. This results in very high Scorer-parameter values in the lowest ca. 1 km.

Choosing an inappropriate lower Scorer-parameter will lead to very high distortions and thus unrealistic values of j. This distortion might be still present in our case choosing the quartiles for the estimating Scorer-parameters, as the two Scorer-parameters seems not to converge to zero. Thus, highest j values are usual in the middle or the higher troposphere (Fig. 30).

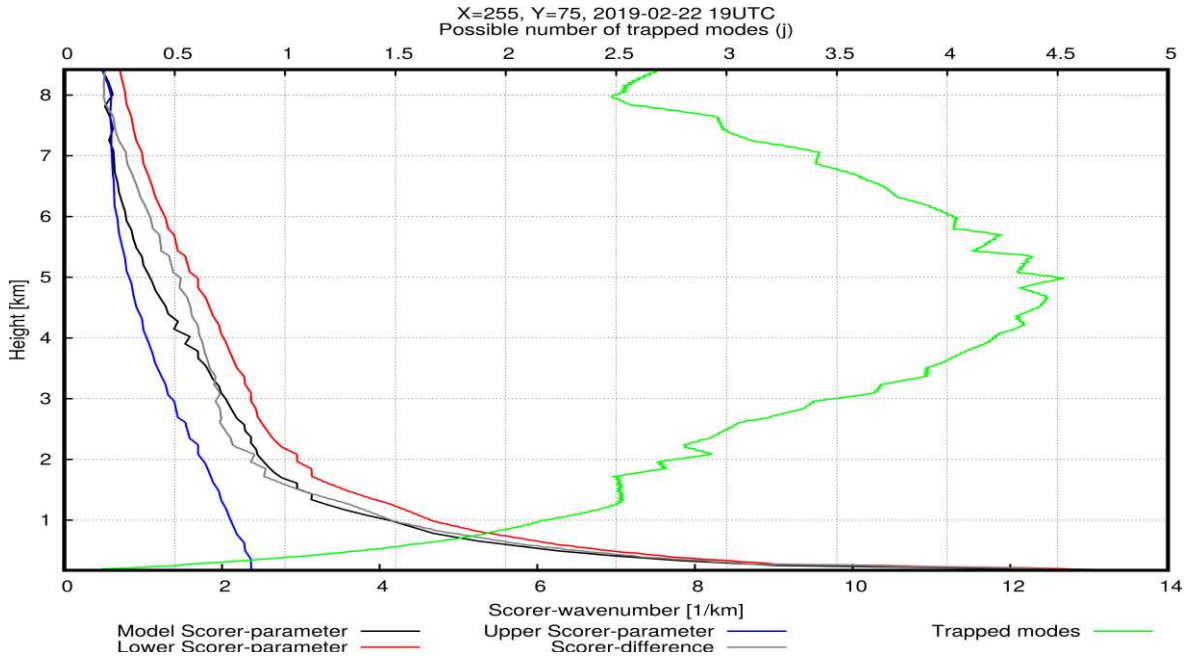

Fig. 30. Profiles of model and approximating Scorer-wavenumbers, and estimated number j of trapped modes (green) at Mezőkeresztes, 19 UTC 22nd February, 2019.

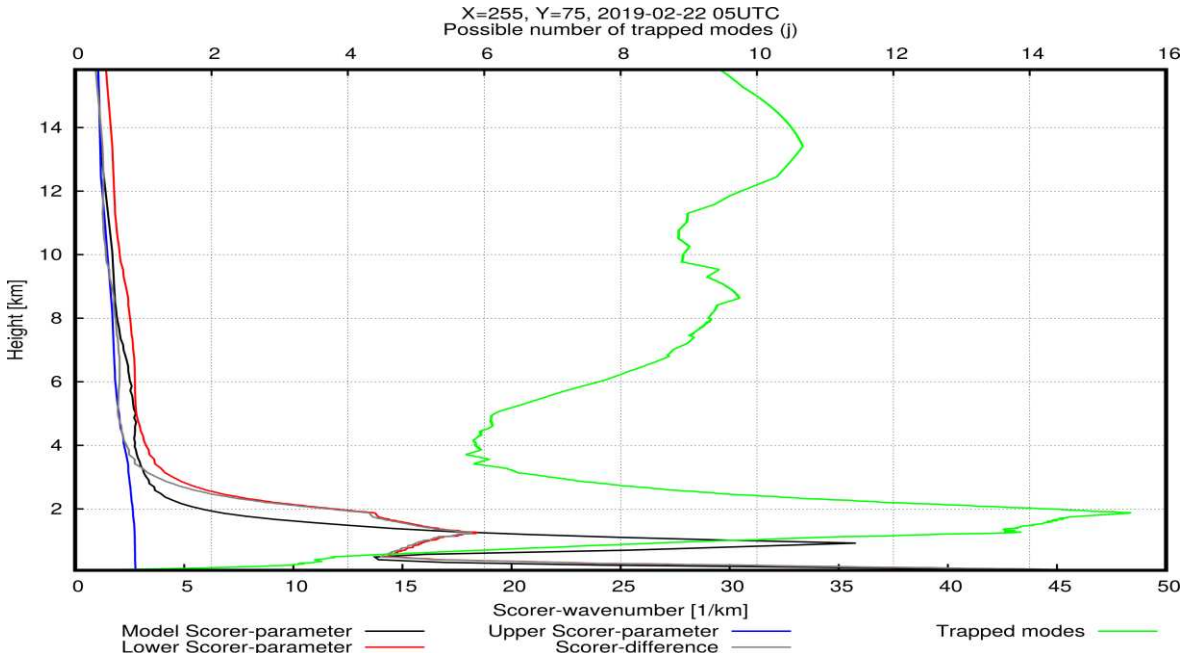

Fig. 31. Profiles of model and approximating Scorer-wavenumbers, and estimated number j of trapped modes (green) at Mezőkeresztes, 5 UTC 22nd February, 2019.

The five grid points share the main features, i.e. there are no significant differences in the results at the different sides of the mountain ranges, which in turn means that the synoptic scale effects (the passage of the front and the inflow of the cold air from North-East behind it) determine the situation and no local effects are recognizable.

One feature visible on Fig.31 is the cold front at 5 UTC, as its inversion causes high Scorer-parameters to appear at around 1 km height. This results in very high *j* values above this layer, at around 2 km. Later, as the surface of the cold front raises, the Scorer-parameter decreases in its inversion. These two effects compensate each other as increasing *Z* would cause *j* to increase, but decreasing Scorer-parameter would cause *j* to decrease. This results in nearly the same maximal *j* values but at a slightly higher altitude (Fig. 32).

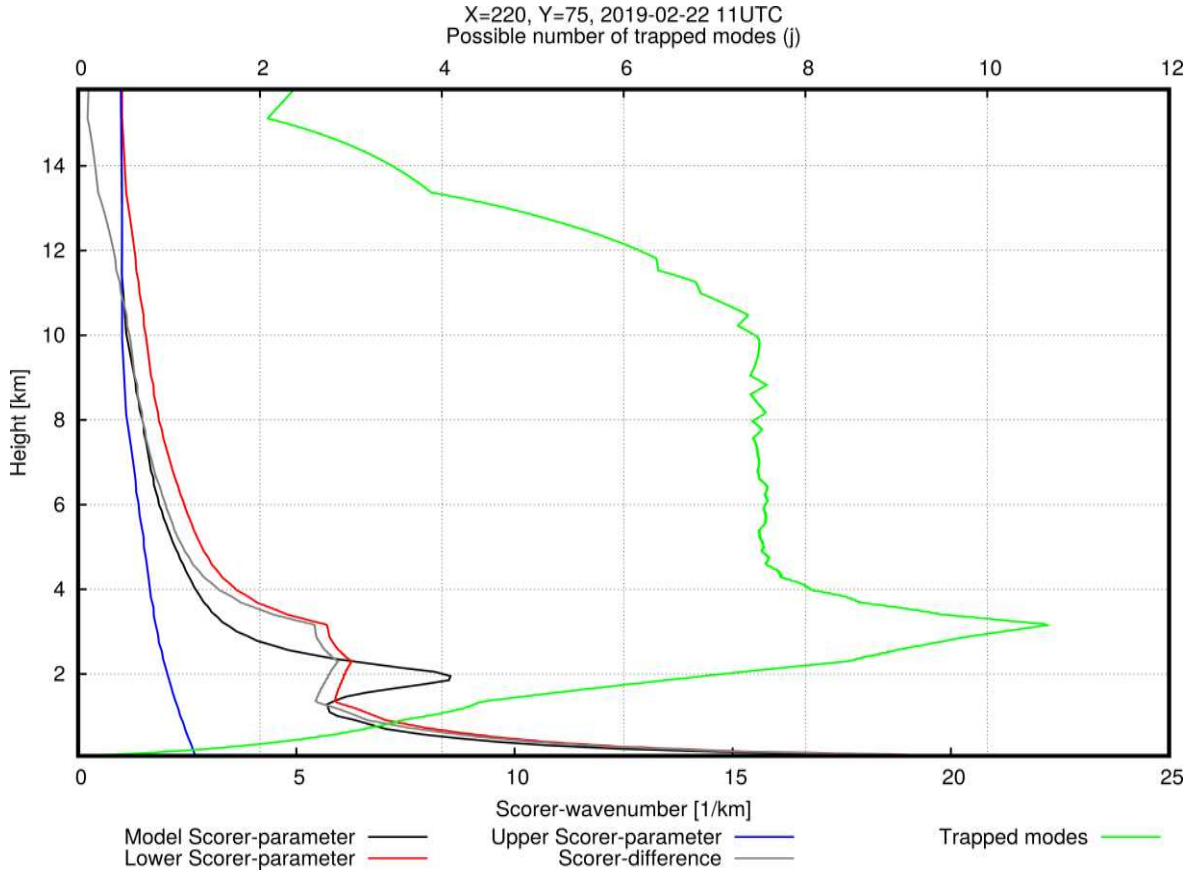

Fig. 32. Profiles of model and approximating Scorer-wavenumbers, and estimated number j of trapped modes (green) at Ecséd, 11 UTC 22nd February, 2019.

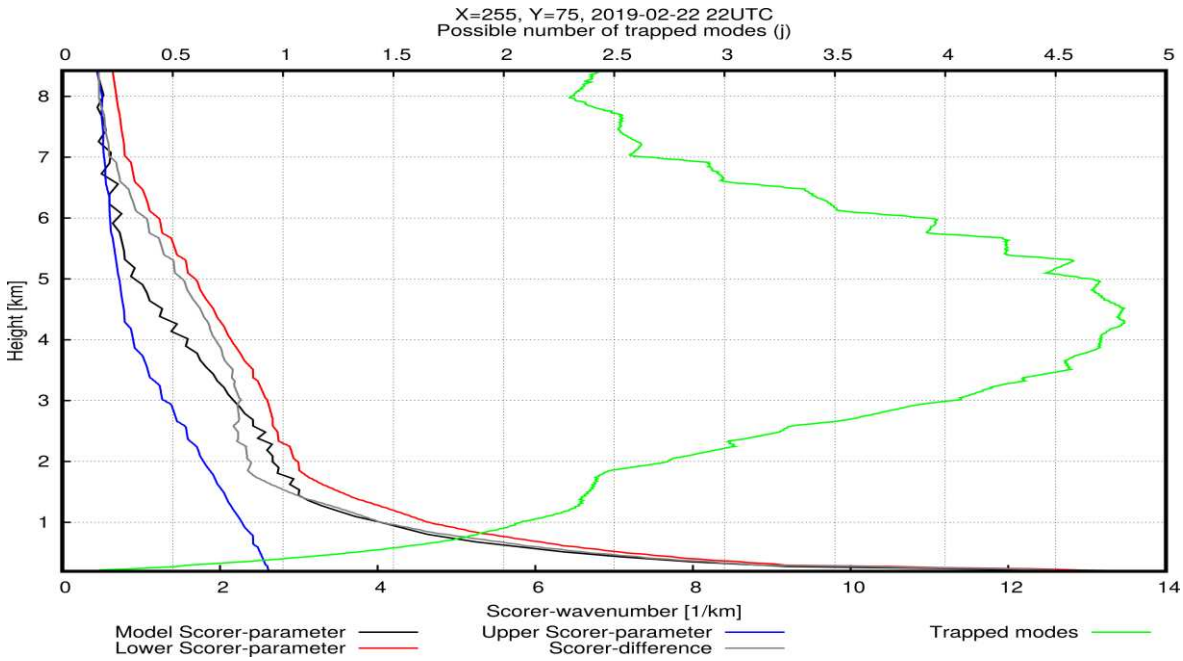

Fig. 33. Profiles of model and approximating Scorer-wavenumbers, and estimated number j of trapped modes (green) at Mezőkeresztes, 22 UTC 22nd February, 2019.

As the cold front moved further away, the profiles became close to a normal moist-adiabatic state and the resulting maximal *j* values decreased to around 5 (Fig. 33). However, later during the night, a gradual decrease of the Scorer-parameter in the middle troposphere developed and caused the slight increase of *j* at that levels (Fig. 34).

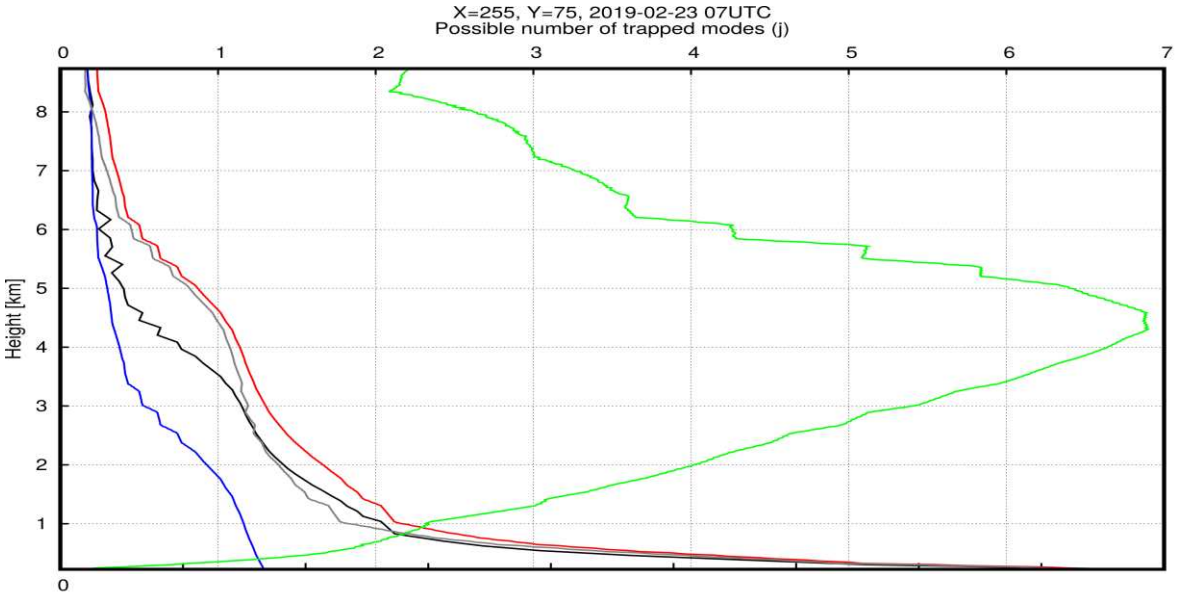

Fig. 34. Profiles of model and approximating Scorer-wavenumbers, and estimated number j of trapped modes (green) at Mezőkeresztes, 07 UTC 23rd February, 2019.

An important note is that equation (22) is written in the way that it includes both free and fixed boundaries for both the upper and lower boundary of the lower layer. In reality, however, both layers are usually only of one type (in spite that this must not be the case as different wave modes can be trapped in different layers), i.e. there are usually only one of 4 possible trapped wave modes present in reality. Dividing the resulted j values with 4 gives more realistic results of around 1 in general, and around 3 to 5 in a highly favorable situation for mountain wave trapping which seems to be quite realistic.

Comparing the results from the different model runs leads to the same conclusion as the sensitivity analysis. It seems that the effect of the differences during the spin-up time is significant on the j values. Differences of 3 to 6, depending also on the height, can occur, however, the general shape is similar, i.e. highest values are in the middle or upper troposphere. After around 6 to 8 time-steps, the differences decrease to nearly zero.

A more comprehensive study will be needed to understand the behavior of this product in different situations. This is a recent idea and a new direction of the research and it is highly experimental and at a rudimentary state.

5. Summary and Future plans

This thesis provided a comprehensive summary of the linear theory of mountain wave formation. Concepts introduced in this theory were examined through a case study which aims to serve as a basis for the documentation of the mountain wave forecast products planned to be published on the website of the Unit of Aviation Meteorology of the HMS. This work was interrupted by the epidemic situation and associated regulations on personal contact, so several other cases remained a further plan to work with. The main conclusion of this case study is that the qualitative analysis is reproducible in other cases, proving that rules for users to the interpretation of these products can be formulated.

However, model cycle updates can have an effect on the products which is needed to be examined. A short examination presented here resulted in the conclusion that model spin-up has the most significant effect on the atmospheric parameters, including the Scorer-parameter, in the first 4 to 8 hours and the different terrain datasets have little effect compared to this. However, as the model reaches statistical equilibrium, the differences between the two datasets vanish but remains statistically significant. Statistical significance, thus, doesn't necessarily means inconsistencies in the model outputs and consistency must be defined separately.

The support of mountain wave gliding branch of General Aviation in Hungary has been provided with limited information, which is being currently expanded by the research effort of the Hungarian experts. Our future plans can be divided based on the time horizon of implementation.

5.1. Short-term plans

The primary plan is to expand the products presented at the mountain wave gliding forecast products at the aviation.met.hu website, with temporal and spatial profile cross-sections for several places in Hungary. Fig. 35 shows planned lines of cross-sections intersecting some mountain ranges, and points of time-height sections at many sport airfields. This is currently under consideration.

Since trapped waves can occupy larger areas in appropriate weather conditions, it may be useful to also create products for some cities even in the Great Plain, for example for Nyíregyháza or Kalocsa.

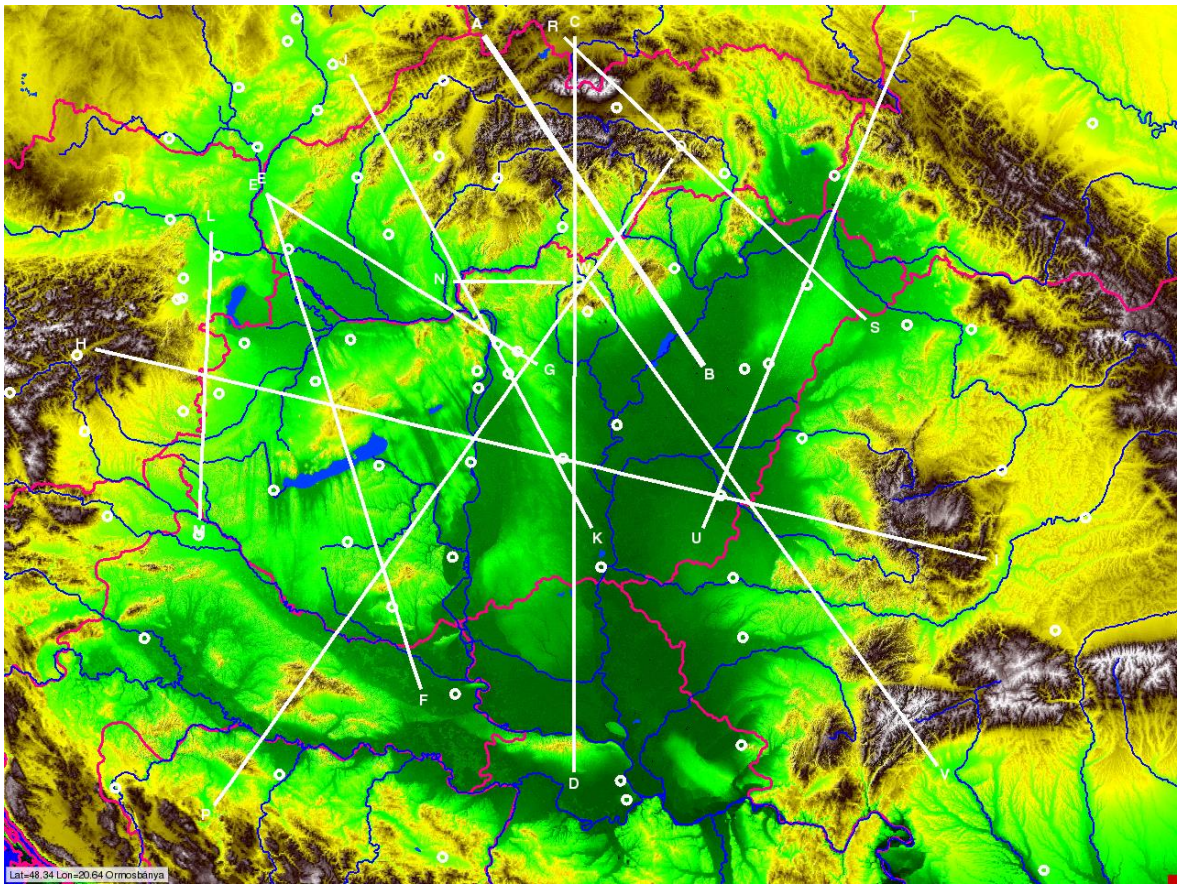

Fig. 35. Preliminary plan of placement of cross-sections (lines) and time-height sections (circles) for the products to be published on aviation.met.hu.

The original aim of this Thesis was to serve as a basis for the documentation of the products. For this, analysis of several other case studies is planned. These will include also situations where MTW formation was not observed, to unambiguously identify features on the products indicating mountain wave formation.

We plan to display cloud fraction on the relative humidity product later. It was available for the 2017-10-13 case but it is not calculated by default and needs some setup adjustments. In the AROME model, only the mixing ratio of hydrometeors is currently available, but this is a less useful information for users. Low, medium and high cloud coverage are 2D variables from which a vertical section cannot be produced. The plan is to calculate a 3D cloud fraction based on the number of hydrometeors.

5.2. Middle-term plans

Development of the wave trapping identification algorithm is needed. The most performance improvement can be achieved by reconsidering the choice of the approximating lower and upper Scorer-parameter values. Values not needing the ordering of the Scorer-parameter would reduce the processor cycle count order from $2N^2 \log N$ to N, where N is the count of

the interpolated layers and is on order of 10^4. However, the choice has a significant effect on the results for j, thus, extreme care must be taken and a comprehensive study will be needed.

5.3. Long-term plans

Currently, there are operative turbulence parameterizations that approximate the turbulence of the free troposphere based on wind speed and shear. SIGMETs, for example, are published, if necessary, based on these indicators. Currently, it is planned to continue the work of André Simon on how AROME can model free-tropospheric turbulence and investigating the relationship between MTW formation and mid-tropospheric turbulence.

Theory of atmospheric turbulence has complicated mathematics. Closure theories are difficult to verify in the higher troposphere. It is difficult to conduct micrometeorological measurement campaigns there with an accuracy similar to what can be achieved in the boundary layer, to understand the nature of mountain wave turbulence. An operational NWP model used in general weather forecasting, like AROME, cannot be accurate enough to describe realistic wave turbulence even in case when turbulence parameterizations has the same accuracy in the free troposphere as in the boundary layer. A 1,5-order closure model (with prognostic equation for the TKE) uses theoretically this kind of parameterizations, however, as these parameterizations are calibrated with measurements mostly in the boundary layer, there is no guarantee for the same accuracy in the free troposphere where boundary layer processes has no effect and the turbulence measurements has less accuracy.

Acknowledgments

This is a special thanks to Mr. Salavec Péter for his daily supervision and deeply detailed corrections and explanations all over the thesis work. I want to thank Dr. Barcza Zoltán for his encouragement and guidance throughout the preparation period and his useful corrections and advice. I'm so grateful also to Dr. Breuer Hajnalka, who helped me pick up an interesting subject of my thesis. Special thanks also to the members of the Hungarian Meteorological Service, especially to Ms. Szépszó Gabriella, Mr. Lancz Dávid, Mr. Kullmann László, Mr. Szintai Balázs, Mr. Szűcs Mihály and and Mr. Rajnai Márk, for their help with technical informations about the AROME model and data, and the HAWK-3 visualization system.

References

Abegg, B., 1996: *Klimaänderung und Tourismus: Klimafolgenforschung am Beispiel des Wintertourismus in den Schweizer Alpen*. vdf Hochschulverlag AG, 252 p.

Ahmed, O.K., 2014: Assessment of Wind Speed for Electricity Generation in Makhool Mountain in Iraq *2*, 6.

Alaka, M.A., 1958: *Aviation Aspect of Mountain Waves*, WMO Technical Notes. Secretariat of the World Meteorological Organization, 66 p.

Alaka, M.A., 1960: *The airflow over mountains*, WMO Technical Notes. Secretariat of the World Meteorological Organization, 149 p.

Arakawa, A., 2004: The Cumulus Parameterization Problem: Past, Present, and Future. *Journal of Climate*, *17*, 2493–2525. doi:10.1175/1520-0442(2004)017<2493:RATCPP>2.0.CO;2

Azzalini, A., Capitanio, A., 2013: *The Skew-Normal and Related Families*, Cambridge University Press, doi:10.1017/CBO9781139248891

Bacmeister, J.T., 1993: Mountain-Wave Drag in the Stratosphere and Mesosphere Inferred from Observed Winds and a Simple Mountain-Wave Parameterization Scheme. *Journal of the Atmospheric Sciences*, *50*, 377–399. doi:10.1175/1520-0469(1993)050<0377:MWDITS>2.0.CO;2

Bacmeister, J.T., Newman, P.A., Gary, B.L., and Chan, K.R., 1994: An Algorithm for Forecasting Mountain Wave–Related Turbulence in the Stratosphere. *Weather and Forecasting*, *9*, 241–253. doi:10.1175/1520-0434(1994)009<0241:AAFFMW>2.0.CO;2

Balachandran, N.K., 1980: Gravity Waves from Thunderstorms. *Monthly Weather Review*, *108*, 804–816. doi:10.1175/1520-0493(1980)108<0804:GWFT>2.0.CO;2

Bannon, J.K., 1952: Weather systems associated with some occasions of severe turbulence at high altitude. *Meteorological Magazine*, *81*, 97–101.

Barcilon, A., and Fitzjarrald, D., 1985: A Nonlinear Steady Model for Moist Hydrostatic Mountain Waves. *Journal of the Atmospheric Sciences*, *42*, 58–67. doi:10.1175/1520-0469(1985)042<0058:ANSMFM>2.0.CO;2

Barstad, I., Grabowski, W.W., and Smolarkiewicz, P.K., 2007: Characteristics of large-scale orographic precipitation: Evaluation of linear model in idealized problems. *Journal of Hydrology*, *340*, 78–90. doi:10.1016/j.jhydrol.2007.04.005

Beall, C.M., 2007: Detecting natural selection in high-altitude human populations. *Respiratory Physiology & Neurobiology*, *Oxygen Transport at High Altitude: An Integrated Perspective 158*, 161–171. doi:10.1016/j.resp.2007.05.013

Belušić, D., Žagar, M., and Grisogono, B., 2007: Numerical simulation of pulsations in the bora wind. *Quarterly Journal of the Royal Meteorological Society*, *133*, 1371–1388. doi:10.1002/qj.129

Booker, J.R., and Bretherton, F.P., 1967: The critical layer for internal gravity waves in a shear flow. *Journal of Fluid Mechanics*, *27*, 513–539. doi:10.1017/S0022112067000515

Bramberger, M., Dörnbrack, A., Wilms, H., Ewald, F., and Sharman, R., 2020: Mountain-Wave Turbulence Encounter of the Research Aircraft HALO above Iceland. *Journal of Applied Meteorology and Climatology*, *59*, 567–588. doi:10.1175/JAMC-D-19-0079.1

Broad, A.S., 1995: Linear theory of momentum fluxes in 3-D flows with turning of the mean wind with height. *Quarterly Journal of the Royal Meteorological Society*, *121*, 1891–1902. doi:10.1002/qj.49712152806

Browning, K.A., Harrold, T.W., and Starr, J.R., 1970: Richardson number limited shear zones in the free atmosphere. *Quarterly Journal of the Royal Meteorological Society*, *96*, 40–49. doi:10.1002/qj.49709640706

Carney, T.Q., 1995: *Hazardous Mountain Winds: And Their Visual Indicators*. U.S. Department of Commerce, National Oceanic and Atmospheric Administration, 90 p.

Charney, J.G., Fjørtoft, R., and Neumann, J., 1950: Numerical Integration of the Barotropic Vorticity Equation. *Tellus*, *2*, 237–254. doi:10.3402/tellusa.v2i4.8607

Charney, J.G., 1951: Dynamic Forecasting by Numerical Process, In: Compendium of Meteorology: Prepared under the Direction of the Committee on the Compendium of Meteorology (eds. Byers, H.R., Landsberg, H.E., Wexler, H., Haurwitz, B., Spilhaus, A.F., Willett, H.C., Houghton, H.G., and Malone, T.F.). American Meteorological Society, Boston, MA, 470–482. doi:10.1007/978-1-940033-70-9_40

Chunchuzov, I.P., 1994: On a Possible Generation Mechanism for Nonstationary Mountain Waves in the Atmosphere. *Journal of the Atmospheric Sciences*, *51*, 2196–2206. doi:10.1175/1520-0469(1994)051<2196:OAPGMF>2.0.CO;2

Curry, J.A., Ebert, E.E., and Herman, G.F., 1988: Mean and turbulence structure of the summertime Arctic cloudy boundary layer. *Quarterly Journal of the Royal Meteorological Society*, *114*, 715–746. doi:10.1002/qj.49711448109

Cushman-Roisin, B., and Beckers, J.-M., 2011: *Introduction to Geophysical Fluid Dynamics: Physical and Numerical Aspects*. Academic Press, 850 p.

Deardorff, J.W., 1980: Stratocumulus-capped mixed layers derived from a three-dimensional model. *Boundary-Layer Meteorology*, *18*, 495–527. doi:10.1007/BF00119502

Dempsey, K. 2019: The crash of BOAC flight 911: Analysis. URL: https://medium.com/@admiralcloudberg/the-crash-of-boac-flight-911-analysis-dbd2dc4b0f18

Dierking, C.F., 1998: Effects of a Mountain Wave Windstorm at the Surface. *Weather and Forecasting*, *13*, 606–616. doi:10.1175/1520-0434(1998)013<0606:EOAMWW>2.0.CO;2

Downing, L.L., 2013: *Meteorology of Clouds*. AuthorHouse, 156 p.

Doyle, J.D., and Durran, D.R., 2002: The Dynamics of Mountain-Wave-Induced Rotors. *Journal of the Atmospheric Sciences*, *59*, 186–201. doi:10.1175/1520-0469(2002)059<0186:TDOMWI>2.0.CO;2

Durran, D.R., and Klemp, J.B., 1983: A Compressible Model for the Simulation of Moist Mountain Waves. *Monthly Weather Review*, *111*, 2341–2361. doi:10.1175/1520-0493(1983)111<2341:ACMFTS>2.0.CO;2

Durran, D.R., 1986: Mountain Waves, In: Mesoscale Meteorology and Forecasting (ed. Ray, P.S.). American Meteorological Society, Boston, MA, 472–492. doi:10.1007/978-1-935704-20-1_20

Durran, D.R., 1990: Mountain Waves and Downslope Winds, In: Atmospheric Processes over Complex Terrain, Meteorological Monographs (ed. Blumen, W.). American Meteorological Society, Boston, MA, 59–81. doi:10.1007/978-1-935704-25-6_4

Durran, D.R., 2003: Lee Waves and Mountain Waves, In: Encyclopedia of Atmospheric Sciences. Elsevier, 1161–1169. doi:10.1016/B0-12-227090-8/00202-5

Eckermann, S.D., McCormack, J.P., Coy, L., Allen, D., Hogan, T., and Kim, Y.-J., 2004: NOGAPS-ALPHA: A Prototype High-Altitude Global NWP Model. NAVAL RESEARCH LAB WASHINGTON DC.

Elder, J.W., 1967: Thermal Turbulence in Forced Convection. *The Physics of Fluids*, *10*, S237–S239. doi:10.1063/1.1762458

Eliassen, A., and Palm, E., 1960: On the Transfer of Energy in Stationary Mountain Waves. *Geophysiske Publikasjoner*, *22*, 1–23.

Ellrod, G.P., and Knapp, D.I., 1992: An Objective Clear-Air Turbulence Forecasting Technique: Verification and Operational Use. *Weather and Forecasting*, *7*, 150–165. doi:10.1175/1520-0434(1992)007<0150:AOCATF>2.0.CO;2

Epifanio, C.C., and Qian, T., 2008: Wave–Turbulence Interactions in a Breaking Mountain Wave. *Journal of the Atmospheric Sciences*, *65*, 3139–3158. doi:10.1175/2008JAS2517.1

Francis, S.H., 1975: Global propagation of atmospheric gravity waves: A review. *Journal of Atmospheric and Terrestrial Physics*, *37*, 1011–1054. doi:10.1016/0021-9169(75)90012-4

Fritts, D.C., and Nastrom, G.D., 1992: Sources of Mesoscale Variability of Gravity Waves. Part II: Frontal, Convective, and Jet Stream Excitation. *Journal of the Atmospheric Sciences*, *49*, 111–127. doi:10.1175/1520-0469(1992)049<0111:SOMVOG>2.0.CO;2

Fritts, D.C., and Alexander, M.J., 2003: Gravity wave dynamics and effects in the middle atmosphere. *Reviews of Geophysics*, *41*. doi:10.1029/2001RG000106

Fritts, D.C., Vosper, S.B., Williams, B.P., Bossert, K., Plane, J.M.C., Taylor, M.J., Pautet, P.-D., Eckermann, S.D., Kruse, C.G., Smith, R.B., Dörnbrack, A., Rapp, M., Mixa, T., Reid, I.M., and Murphy, D.J., 2018: Large-Amplitude Mountain Waves in the Mesosphere Accompanying Weak Cross-Mountain Flow During DEEPWAVE Research Flight RF22. *Journal of Geophysical Research: Atmospheres*, *123*, 9992–10,022. doi:10.1029/2017JD028250

Garcia, R.R., and Solomon, S., 1985: The effect of breaking gravity waves on the dynamics and chemical composition of the mesosphere and lower thermosphere. *Journal of Geophysical Research: Atmospheres*, *90*, 3850–3868. doi:10.1029/JD090iD02p03850

Gast, P. and Moshtaghian, A. 2015: 'Turbulence causes injuries on Air Canada flight', *URL:* https://edition.cnn.com/2015/12/30/world/air-canada-flight-turbulence/index.html

Gill, P.G., and Stirling, A.J., 2013: Including convection in global turbulence forecasts. *Meteorological Applications*, *20*, 107–114. doi:10.1002/met.1315

Goldstine, H.H., and Goldstine, A., 1946: The Electronic Numerical Integrator and Computer (ENIAC). *Mathematical Tables and Other Aids to Computation*, *2*, 97–110. doi:10.2307/2002620

Griljava, M. and Foster, J. 2015: Cap Clouds on Fuego, Acatenango and Agua Volcanoes. *Earth Science Picture of the Day, 10th December, 2015*, URL: https://epod.usra.edu/blog/2015/12/cap-clouds-on-fuego-acatenango-and-agua-volcanoes.html

Grisogono, B., and Belušić, D., 2009: A review of recent advances in understanding the mesoand microscale properties of the severe Bora wind. *Tellus A: Dynamic Meteorology and Oceanography*, *61*, 1–16. doi:10.1111/j.1600-0870.2007.00369.x

Grubišić, V., and Küttner, J.P., 2005: Final Plans for the Terrain-Induced Rotor Experiment. *Hrvatski meteorološki časopis*, *40*, 450–453.

Grubišić, V., and Orlić, M., 2007: Early observations of rotor clouds by Andrija Mohorovičić. *Bulletin of the American Meteorological Society*, *88*, 693–700. doi:10.1175/BAMS-88-5-693

Grubišić, V., Doyle, J.D., Kuettner, J., Mobbs, S., Smith, R.B., Whiteman, C.D., Dirks, R., Czyzyk, S., Cohn, S.A., Vosper, S., Weissmann, M., Haimov, S., De Wekker, S.F.J., Pan, L.L., and Chow, F.K., 2008: The terrain-induced rotor experiment. *Bulletin of the American Meteorological Society*, *89*, 1513–1534. doi:10.1175/2008BAMS2487.1

Grubišić, V., Serafin, S., Strauss, L., Haimov, S.J., French, J.R., and Oolman, L.D., 2015: Wave-Induced Boundary Layer Separation in the Lee of the Medicine Bow Mountains. Part II: Numerical Modeling. *Journal of the Atmospheric Sciences*, *72*, 4865–4884. doi:10.1175/JAS-D-14-0381.1

Grushka, E., 1972: Characterization of Exponentially Modified Gaussian Peaks in Chromatography. *Analutical Chemistry, 44,* 1733–1738. doi:10.1021/ac60319a011

Guarino, M.V., 2017: Mountain wave breaking in atmospheric flows with directional wind shear. Phd Thesis, University of Reading.

Hanson, H.P., 1987: Radiative/Turbulent Transfer Interactions in Layer Clouds. *Journal of the Atmospheric Sciences*, *44*, 1287–1295. doi:10.1175/1520-0469(1987)044<1287:RTIILC>2.0.CO;2

Herak, D. and Herak, M. 2007: Andrija Mohorovičić (1857-1936) — On the occasion of the 150th anniversary of his birth. *Seismological Research Letters 78*, 671-674. doi:10.1785/gssrl.78.6.671

Hertenstein, R.F., and Küttner, J.P., 2016: Simulations of Rotors Using Steep Lee Topography.

Hills, M.O.G., and Durran, D.R., 2012: Nonstationary Trapped Lee Waves Generated by the Passage of an Isolated Jet. *Journal of the Atmospheric Sciences*, *69*, 3040–3059. doi:10.1175/JAS-D-12-047.1

Hirth, W., 1935: *Die hohe Schule des Segelfluges: Eine Anleitg zum therm., Wolken- u. Gewitter-Segelflug ; Mit Beitr. von ...* Klasing, 194 p.

Holmboe, J., and Klieforth, H., 1957: Investigation of Mountain Lee Waves and the Air Flow Over the Sierra Nevada. Defense Technical Information Center, Fort Belvoir, VA. doi:10.21236/AD0133606

Holton, J.R., and Hakim, G.J., 2013: *An Introduction to Dynamic Meteorology*, Fifth ed. Academic Press, Amsterdam, 553 p.

Horányi, A., Kertész, S., Kullmann, L., and Radnóti, G., 2006: The ARPEGE/ALADIN mesoscale numerical modeling system and its application at the Hungarian Meteorological Service. *Időjárás, Quarterly Journal of the Hungarian Meteorological Service*, *110*, 203–227.

Houze Jr., R.A., 2014: *Cloud Dynamics*. Academic Press, 457 p.

Janovics, F. and Farkas, A. 2006: 134/2006 számú légiközlekedési baleset. *URL:* http://www.kbsz.hu/j25/hu/legi-kozlekedes/kbsz-altal-vizsgalt-esemenyek-2014/25-legi-kozlekedes/latest-sp-842/1158-20060514zj

Jiang, Q., and Doyle, J.D., 2008: Diurnal Variation of Downslope Winds in Owens Valley during the Sierra Rotor Experiment. *Monthly Weather Review*, *136*, 3760–3780. doi:10.1175/2008MWR2469.1

Job, M. 1995: *Air Disaster*. Vol. 1. Aerospace Publications, Indiana Universtity.

Kaimal, J.C., and Finnigan, J.J., 1994: *Atmospheric Boundary Layer Flows: Their Structure and Measurement*. Oxford University Press, 304 p.

Kaltenborn, B.P., Nellemann, C., Vistnes, I.I., and GRID--Arendal, 2010: *High mountain glaciers and climate change: challenges to human livelihoods and adaptation*. GRID-Arendal : UNEP, Arendal, Norway.

Kim, J., and Mahrt, L., 1992: Simple formulation of turbulent mixing in the stable free atmosphere and nocturnal boundary layer. *Tellus A*, *44*, 381–394. doi:10.1034/j.1600-0870.1992.t01-4-00003.x

Kim, Y.-J., Eckermann, S.D., and Chun, H.-Y., 2003: An overview of the past, present and future of gravity-wave drag parametrization for numerical climate and weather prediction models. *Atmosphere-Ocean*, *41*, 65–98. doi:10.3137/ao.410105

Klemp, J.B., and Lilly, D.R., 1975: The Dynamics of Wave-Induced Downslope Winds. *Journal of the Atmospheric Sciences*, *32*, 320–339. doi:10.1175/1520-0469(1975)032<0320:TDOWID>2.0.CO;2

Koschmieder, H., 1925: Zur Kenntnis des Stromfeldes in Lee. *Zeitschrift für Flugtechnik und Motorluftschiffahrt*, *16*, 240–244.

Kozhevnikov, V.N., Berzegova, R.B., and Bedanokov, M.K., 2020: Modeling of the Novorossiysk bora. Part 1. Atmospheric disturbances over the mountains of Novorossiysk. *Russian Journal of Earth Sciences*, *20*, 1–12. doi:10.2205/2019ES000684

Küttner, J.P., 1938: Moazagotl und Föhnwelle. *Beiträge zur Physik der freien Atmosphäre*, *25*, 79–114.

Küttner, J.P., and Jenkins, C.F., 1953: *Flight Aspects of the Mountain Wave*. Geophysics Research Directorate, Air Force Cambridge Research Center, 24 p.

Küttner, J.P., 1959: *The Rotor Flow in the Lee of Mountains*. Meteorological Development Laboratory, Geophysics Research Directorate, Air Force Cambridge Research Center, 40 p.

Lafore, J.P., Stein, J., Asencio, N., Bougeault, P., Ducrocq, V., Duron, J., Fischer, C., Héreil, P., Mascart, P., Masson, V., Pinty, J.P., Redelsperger, J.L., Richard, E., and de Arellano, J.V.-G., 1997: The Meso-NH Atmospheric Simulation System. Part I: adiabatic formulation and control simulations. *Annales Geophysicae*, *16*, 90–109. doi:10.1007/s00585-997-0090-6

Lane, T.P., Reeder, M.J., and Clark, T.L., 2001: Numerical Modeling of Gravity Wave Generation by Deep Tropical Convection. *Journal of the Atmospheric Sciences*, *58*, 1249–1274. doi:10.1175/1520-0469(2001)058<1249:NMOGWG>2.0.CO;2

Levenberg, K. 1944: A Method for the Solution of Certain Non-linear Problems in Least Squares. *Quarterly of Applied Mathematics 2*, 164-168.

Lilly, D.K., 1968: Models of cloud-topped mixed layers under a strong inversion. *Quarterly Journal of the Royal Meteorological Society*, *94*, 292–309. doi:10.1002/qj.49709440106

Lilly, D.K., and Kennedy, P.J., 1973: Observations of a Stationary Mountain Wave and its Associated Momentum Flux and Energy Dissipation. *Journal of the Atmospheric Sciences*, *30*, 1135–1152. doi:10.1175/1520-0469(1973)030<1135:OOASMW>2.0.CO;2

Lilly, D.K., 1978: A Severe Downslope Windstorm and Aircraft Turbulence Event Induced by a Mountain Wave. *Journal of the Atmospheric Sciences*, *35*, 59–77. doi:10.1175/1520-0469(1978)035<0059:ASDWAA>2.0.CO;2

Lin, Y., and Zhang, F., 2008: Tracking Gravity Waves in Baroclinic Jet-Front Systems. *Journal of the Atmospheric Sciences*, *65*, 2402–2415. doi:10.1175/2007JAS2482.1

Long, R.R., 1953: Some Aspects of the Flow of Stratified Fluids: I. A Theoretical Investigation. *Tellus*, *5*, 42–58. doi:10.3402/tellusa.v5i1.8563

Lynch, P., 2006: *The Emergence of Numerical Weather Prediction: Richardson's Dream*. Cambridge University Press, 251 p.

Lynch, P., 2008: The ENIAC Forecasts: A Re-creation. *Bulletin of the American Meteorological Society*, *89*, 45–56. doi:10.1175/BAMS-89-1-45

Lyra, G., 1943: Theorie der stationären Leewellenströmung in freier Atmosphäre. *ZAMM - Journal of Applied Mathematics and Mechanics / Zeitschrift für Angewandte Mathematik und Mechanik*, *23*, 1–28. doi:10.1002/zamm.19430230102

Malkus, W.V.R., and Chandrasekhar, S., 1954: The heat transport and spectrum of thermal turbulence. *Proceedings of the Royal Society of London. Series A. Mathematical and Physical Sciences*, *225*, 196–212. doi:10.1098/rspa.1954.0197

Marquardt, D.W. 1963: An Algorithm for Least-Squares Estimation of Nonlinear Parameters. *Journal of the Society for Industrial and Applied Mathematics 11*, 431-441.

Maruhashi, J., 2019: Mountain Waves in Aviation: Prediction and Effects. MSc Thesis. Técnico Lisboa, Lisboa, 95 p.

McDowell, G., Ford, J.D., Lehner, B., Berrang-Ford, L., and Sherpa, A., 2013: Climate-related hydrological change and human vulnerability in remote mountain regions: a case study from Khumbu, Nepal. *Regional Environmental Change*, *13*, 299–310. doi:10.1007/s10113-012-0333-2

McFarlane, N.A., 1987: The Effect of Orographically Excited Gravity Wave Drag on the General Circulation of the Lower Stratosphere and Troposphere. *Journal of the Atmospheric Sciences*, *44*, 1775–1800. doi:10.1175/1520-0469(1987)044<1775:TEOOEG>2.0.CO;2

McHugh, J., and Sharman, R., 2013: Generation of mountain wave-induced mean flows and turbulence near the tropopause. *Quarterly Journal of the Royal Meteorological Society*, *139*, 1632–1642. doi:10.1002/qj.2035

McLandress, C., 1998: On the importance of gravity waves in the middle atmosphere and their parameterization in general circulation models. *Journal of Atmospheric and Solar-Terrestrial Physics*, *60*, 1357–1383. doi:10.1016/S1364-6826(98)00061-3

Minár, J., Falťan, V., Bánovský, M., and Damankošová, Z., 2008: Impact of a catastrophic wind on various types of site in the Tatra National Park. *Folia Geographica*, *Series Geographica-Physica 39*, 95–106.

Miyoshi, Y., and Fujiwara, H., 2008: Gravity Waves in the Thermosphere Simulated by a General Circulation Model. *Journal of Geophysical Research: Atmospheres*, *113*. doi:10.1029/2007JD008874

Moeng, C.-H., 1986: Large-Eddy Simulation of a Stratus-Topped Boundary Layer. Part I: Structure and Budgets. *Journal of the Atmospheric Sciences*, *43*, 2886–2900. doi:10.1175/1520-0469(1986)043<2886:LESOAS>2.0.CO;2

Montmerle, T., Michel, Y., Arbogast, E., Ménétrier, B., and Brousseau, P., 2018: A 3D ensemble variational data assimilation scheme for the limited-area AROME model:

Formulation and preliminary results. *Quarterly Journal of the Royal Meteorological Society*, *144*, 2196–2215. doi:10.1002/qj.3334

Murrow, H.M., McCain, W.E., and Rhyne, R.H., 1982: Power spectral measurements of clear-air turbulence to long wavelengths for altitudes up to 14,000 meters. *NASA Technical Paper 1979,* 165.

Nance, L.B., and Durran, D.R., 1997: A Modeling Study of Nonstationary Trapped Mountain Lee Waves. Part I: Mean-Flow Variability. *Journal of the Atmospheric Sciences*, *54*, 2275–2291. doi:10.1175/1520-0469(1997)054<2275:AMSONT>2.0.CO;2

Nappo, C.J., 2012: *An Introduction to Atmospheric Gravity Waves*, 2nd ed, International Gephysics. Academic Press, 400 p.

Oke, T.R., 2002: *Boundary Layer Climates*, 2nd ed. Routledge, London; New York, 460 p.

Orlanski, I., and Ross, B.B., 1973: Numerical simulation of the generation and breaking of internal gravity waves. *Journal of Geophysical Research (1896-1977)*, *78*, 8808–8826. doi:10.1029/JC078i036p08808

Orlanski, I. 1975: A Rational Subdivision of Scales for Atmospheric Processes. *Bulleti of the American Meteorological Society 56*, 527-530.

Pao, Y.-H., 1969: Origin and Structure of Turbulence in Stably Stratified Media, In: Clear Air Turbulence and Its Detection (eds. Pao, Y.-H., and Goldburg, A.). Springer US, Boston, MA, 73–99. doi:10.1007/978-1-4899-5615-6_6

Peltier, W.R., and Clark, T.L., 1979: The Evolution and Stability of Finite-Amplitude Mountain Waves. Part II: Surface Wave Drag and Severe Downslope Windstorms. *Journal of the Atmospheric Sciences*, *36*, 1498–1529. doi:10.1175/1520-0469(1979)036<1498:TEASOF>2.0.CO;2

Queney, P., 1946: Theory of perturbations in stratified currents with applications to air flow over mountain barriers. Article; Article/Report. Chicago: University of Chicago.

Queney, P., 1955: Rotor Phenomena in the Lee of Mountains. *Tellus*, *7*, 367–371. doi:10.1111/j.2153-3490.1955.tb01173.x

Ralph, F.M., Neiman, P.J., Keller, T.L., Levinson, D., and Fedor, L., 1997a: Observations, Simulations, and Analysis of Nonstationary Trapped Lee Waves. *Journal of the Atmospheric Sciences*, *54*, 1308–1333. doi:10.1175/1520-0469(1997)054<1308:OSAAON>2.0.CO;2

Ralph, F.M., Neiman, P.J., and Levinson, D., 1997b: Lidar observations of a breaking mountain wave associated with extreme turbulence. *Geophysical Research Letters*, *24*, 663–666. doi:10.1029/97GL00349

Ralph, F.M., Neiman, P.J., and Keller, T.L., 1999: Deep-Tropospheric Gravity Waves Created by Leeside Cold Fronts. *Journal of the Atmospheric Sciences*, *56*, 2986–3009. doi:10.1175/1520-0469(1999)056<2986:DTGWCB>2.0.CO;2

Reiter, E.R., and Rasmussen, J.L., 1967: *Proceedings of the Symposium on Mountain Meteorology*, Technical Papers on Atmospheric Science. Colorado State University, Fort Collins, Colorado, USA, 230 p.

Richardson, L.F., 1922: *Weather Prediction by Numerical Process*. Cambridge University Press, 262 p.

Salavec P., 2018: Fejlesztések a Hullám-előrejelzés Terén az Országos Meteorológiai Szolgálatnál. *Repüléstudományi Közlemények*, *30*, 77–98.

Sato, J., 2004: ASB Flying Club Sukhoi SU-26, RA2821K, A Crash to the Ground, Aerial Circuit in Motegi Town, Haga County, Tochigi Prefecture, Japan, October 31, 2003. Aicraft Accident Investigation ReportNo. AA2004-2. Aircraft and Railway Accidents Investigation Commission, Japan.

Schöberl, M.R., 1985: The Penetration of Mountain Waves into the Middle Atmosphere. *Journal of the Atmospheric Sciences*, *42*, 2856–2864. doi:10.1175/1520-0469(1985)042<2856:TPOMWI>2.0.CO;2

Scorer, R.S., 1949: Theory of waves in the lee of mountains. *Quarterly Journal of the Royal Meteorological Society*, *75*, 41–56. doi:10.1002/qj.49707532308

Scorer, R.S., 1951: Forecasting the Occurrence of Lee Waves. *Weather*, *6*, 99–103. doi:10.1002/j.1477-8696.1951.tb01322.x

Scorer, R.S., 1955: Theory of airflow over mountains: IV-separation of flow from the surface. *Quarterly Journal of the Royal Meteorological Society*, *81*, 340–350. doi:10.1002/qj.49708134905

Scorer, R.S., and Klieforth, H., 1959: Theory of mountain waves of large amplitude. *Quarterly Journal of the Royal Meteorological Society*, *85*, 131–143. doi:10.1002/qj.49708536406

Seity, Y., Brousseau, P., Malardel, S., Hello, G., Bénard, P., Bouttier, F., Lac, C., and Masson, V., 2010: The AROME-France Convective-Scale Operational Model. *Monthly Weather Review*, *139*, 976–991. doi:10.1175/2010MWR3425.1

Sharman, R., Wiener, G., and Brown, B., 2000: Description and verification of the NCAR Integrated Turbulence Forecasting Algorithm (ITFA). Amer. Inst. Aeronautics and Astronautics, Boulder, CO, USA, 9. doi:10.2514/6.2000-493

Sharman, R., Tebaldi, C., Wiener, G., and Wolff, J., 2006: An Integrated Approach to Mid- and Upper-Level Turbulence Forecasting. *Weather and Forecasting*, *21*, 268–287. doi:10.1175/WAF924.1

Sharman, R., and Lane, T., 2016: *Aviation Turbulence: Processes, Detection, Prediction*. Springer, 529 p.

Sharman, R.D., Trier, S.B., Lane, T.P., and Doyle, J.D., 2017: Sources and dynamics of turbulence in the upper troposphere and lower stratosphere: A review. *Geophysical Research Letters*, *39*, LI2803. doi:10.1029/2012GL051996

Shutts, G., 1992: Observations and Numerical Model Simulation of a Partialy Trapped Lee Wave over the Welsh Mountains. *Monthly Weather Review*, *120*, 2056–2066. doi:10.1175/1520-0493(1992)120<2056:OANMSO>2.0.CO;2

Smith, C.M., and Skyllingstad, E.D., 2009: Investigation of Upstream Boundary Layer Influence on Mountain Wave Breaking and Lee Wave Rotors Using a Large-Eddy Simulation. *Journal of the Atmospheric Sciences*, *66*, 3147–3164. doi:10.1175/2009JAS2949.1

Smith, C.M., and Skyllingstad, E.D., 2011: Effects of Inversion Height and Surface Heat Flux on Downslope Windstorms. *Monthly Weather Review*, *139*, 3750–3764. doi:10.1175/2011MWR3619.1

Smith, R.B., 1979: The Influence of Mountains on the Atmosphere, In: Advances in Geophysics (ed. Saltzman, B.). Elsevier, 87–230. doi:10.1016/S0065-2687(08)60262-9

Smith, R.B., 2003: Stratified Flow Over Topography, In: Environmental Stratified Flows, Topics in Environmental Fluid Mechanics (ed. Grimshaw, R.). Springer US, 119–159. doi:10.1007/0-306-48024-7_5

Smith, R.B., Woods, B.K., Jensen, J., Cooper, W.A., Doyle, J.D., Jiang, Q., and Grubišić, V., 2008: Mountain Waves Entering the Stratosphere. *Journal of the Atmospheric Sciences*, *65*, 2543–2562. doi:10.1175/2007JAS2598.1

Staquet, C., and Sommeria, J., 2002: Internal Gravity Waves: From Instabilities to Turbulence. *Annual Review of Fluid Mechanics*, *34*, 559–593. doi:10.1146/annurev.fluid.34.090601.130953

Stone, R.I., 1968: 124 die in 2nd Japan air disaster. *Long Beach, California: Press-Telegram*. A-1, A-3 URL: https://aviation-safety.net/database/record.php?id=19660305-1.

Strauss, L., Serafin, S., and Grubišić, V., 2015: Atmospheric Rotors and Severe Turbulence in a Long Deep Valley. *Journal of the Atmospheric Sciences*, *73*, 1481–1506. doi:10.1175/JAS-D-15-0192.1

Sun, C., Zhou, Q., and Xia, K.-Q., 2006: Cascades of Velocity and Temperature Fluctuations in Buoyancy-Driven Thermal Turbulence. *Physical Review Letters*, *97*, 144504. doi:10.1103/PhysRevLett.97.144504

Sun, J., Mahrt, L., Banta, R.M., and Pichugina, Y.L., 2011: Turbulence Regimes and Turbulence Intermittency in the Stable Boundary Layer during CASES-99. *Journal of the Atmospheric Sciences*, *69*, 338–351. doi:10.1175/JAS-D-11-082.1

Szintai, B., Szűcs, M., Randriamampianina, R., and Kullmann, L., 2015: Application of the AROME non-hydrostatic model at the Hungarian Meteorological Service: physical parameterizations and ensemble forecasting. *Időjárás, Quarterly Journal of the Hungarian Meteorological Service*, *119*, 241–265.

Tan, K.-A., and Eckermann, S.D., 2000: Numerical Simulations of Mountain Waves in the Middle Atmosphere over the Southern Andes. Hulburt Center for Space Research, Naval Research Laboratory, Washington D.C.

Teets Jr., E.H., and Carter, E.J., 2002: *Atmospheric Conditions of Stratospheric Mountain Waves: Soaring the Perlan Aircraft to 30 km*.

Teixeira, M.A.C., 2014: The physics of orographic gravity wave drag. *Frontiers in Physics*, *2*, 24. doi:10.3389/fphy.2014.00043

Tokgozlu, A., Rasulov, M., and Aslan, Z., 2005: Modeling and Classification of Mountain Waves. *Technical Soaring*, *29*, 22–30.

Turner, J.S., 1999: Development of a Mountain Wave Turbulence Prediction Scheme for Civil Aviation. Met Office Forecasting Research Technical ReportNo. 265.

Tutiš, V., 1992: Trapped lee waves: A special analytical solution. *Meteorology and Atmospheric Physics*, *50*, 189–195. doi:10.1007/BF01026016

Udina, M., Bech, J., Gonzalez, S., Soler, M.R., Paci, A., Miró, J.R., Trapero, L., Donier, J.M., Douffet, T., Codina, B., and Pineda, N., 2020: Multi-sensor observations of an elevated rotor during a mountain wave event in the Eastern Pyrenees. *Atmospheric Research*, *234*, 104698. doi:10.1016/j.atmosres.2019.104698

Uhlenbrock, N.L., Bedka, K.M., Feltz, W.F., and Ackerman, S.A., 2007: Mountain Wave Signatures in MODIS 6.7-μm Imagery and Their Relation to Pilot Reports of Turbulence. *Weather and Forecasting*, *22*, 662–670. doi:10.1175/WAF1007.1

van der Mescht, D., and Geldenhuys, M., 2019: Observations of mountain waves with interference generated by coastal mountains in South Africa. *Meteorological Applications*, *26*, 409–415. doi:10.1002/met.1771

VanZandt, T.E., and Fritts, D.C., 1989: A Theory of Enhanced Saturation of the Gravity Wave Spectrum Due to Increases in Atmospheric Stability, In: Middle Atmosphere, Pageoph Topical Volumes (eds. Plumb, R.A., and Vincent, R.A.). Birkhäuser, Basel, 399–420. doi:10.1007/978-3-0348-5825-0_16

Vinnichenko, N.K., and Dutton, J.A., 1969: Empirical studies of atmospheric structure and spectra in the free atmosphere. *Radio Science*, *4*, 1115–1126. doi:10.1029/RS004i012p01115

Vosper, S.B., Sheridan, P.F., and Brown, A. r., 2006: Flow separation and rotor formation beneath two-dimensional trapped lee waves. *Quarterly Journal of the Royal Meteorological Society*, *132*, 2415–2438. doi:10.1256/qj.05.174

Watkins, S., Thompson, M., Loxton, B., and Abdulrahim, M., 2010: On Low Altitude Flight through the Atmospheric Boundary Layer. *International Journal of Micro Air Vehicles*, *2*, 55–68. doi:10.1260/1756-8293.2.2.55

Wurtele, M.G., Sharman, R.D., and Datta, A., 1996: Atmospheric Lee Waves. *Annual Review of Fluid Mechanics*, *28*, 429–476. doi:10.1146/annurev.fl.28.010196.002241

Wyngaard, J.C., Coté, O.R., and Izumi, Y., 1971: Local Free Convection, Similarity, and the Budgets of Shear Stress and Heat Flux. *Journal of the Atmospheric Sciences*, *28*, 1171–1182. doi:10.1175/1520-0469(1971)028<1171:LFCSAT>2.0.CO;2

1. sz. Melléklet

Konzultációs adatlap diplomamunkához

Hallgató adatai

név: Ghanmi Imen **Neptun-kód: A65E5j**

Dátum	Tevékenység	Aláírás
2018.07.04.	First meeting	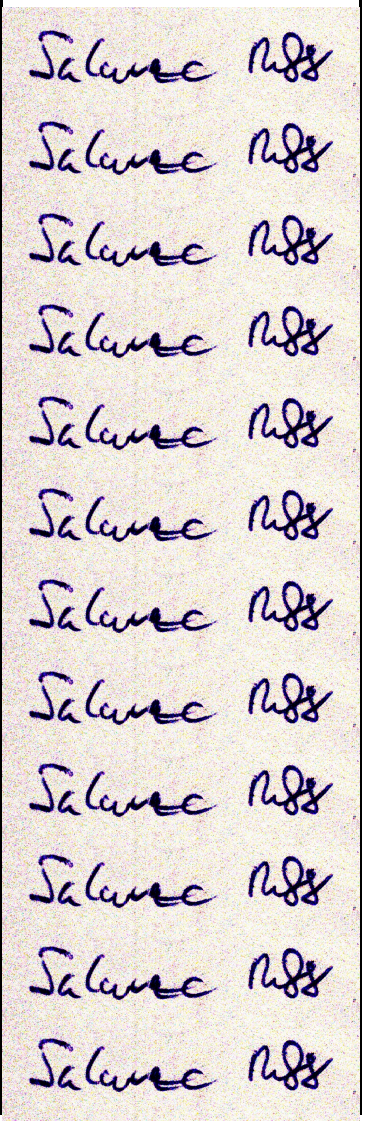
2018.08.30.	Summer practice: discussion about mountain waves and the AROME model	
2018.10.15.	Discussion about linear theory and planned case studies	
2019.04.03.	Discussion about the linear theory	
2019.05.08.	Discussion about the literature and the linear theory of mountain waves	
2019.11.12.	Visiting model developers to collect information about AROME	
2019.12.03.	Finalizing parts of literature review	
2020.01.29.	Preparing case study, fixing methodology	
2020.02.15.	Discussion about the results of case 22nd February 2019	
2020.04.08.	New tasks due to vis major: Sensitivity analysis and automatic trapping detection	
2020.04.30.	Preparing results of the new tasks	
2020.05.08.	Formatting and preparing Thesis for final approval and submission	

A dolgozat jelenlegi formájában [beadható / nem adható be]: beadható

2020.05.15. **Salavec Péter**

dátum **Belső konzulens/Témavezető neve**

STATEMENT

Name: Ghanmi Imen

Neptun code: A65E5j

ELTE Faculty of Science, Field of studies: meteorology

Title of thesis: Application of Scorer-parameter in Mountain Wave Forecasting at the Hungarian Meteorological Service.

As the author of this master thesis, I declare that it is my own work and that I have acknowledged and referenced the work and ideas of others.

04/05/2020, Budapest

signature